

# The SLUGGS Survey: Kinematics for over 2500 Globular Clusters in Twelve Early-type Galaxies

Vincenzo Pota<sup>1</sup>, Duncan A. Forbes<sup>1</sup>, Aaron J. Romanowsky<sup>2</sup>, Jean P. Brodie<sup>3</sup>,  
Lee R. Spitler<sup>1</sup>, Jay Strader<sup>4</sup>, Caroline Foster<sup>5</sup>, Jacob A. Arnold<sup>3</sup>, Andrew Benson<sup>6</sup>,  
Christina Blom<sup>1</sup>, Jonathan R. Hargis<sup>7</sup>, Katherine L. Rhode<sup>7</sup>, Christopher Usher<sup>1</sup>

<sup>1</sup> Centre for Astrophysics & Supercomputing, Swinburne University, Hawthorn VIC 3122, Australia

<sup>2</sup> Department of Physics and Astronomy, San José State University, San Jose, CA 95192, USA

<sup>3</sup> University of California Observatories, 1156 High Street, Santa Cruz, CA 95064, USA

<sup>4</sup> Department of Physics and Astronomy, Michigan State University, East Lansing, Michigan 48824, USA

<sup>5</sup> European Southern Observatory, Alonso de Cordova 3107, Vitacura, Santiago, Chile

<sup>6</sup> The Observatories of the Carnegie Institution for Science, 813 Santa Barbara Street, Pasadena, CA 91101, USA

<sup>7</sup> Indiana University, 727 East 3rd Street, Swain West 319, Blomington, IN 47405, USA

Email: vpota@astro.swin.edu.au, dforbes@astro.swin.edu.au

Released 2012 Xxxxx XX

## ABSTRACT

We present a spectro-photometric survey of 2522 extragalactic globular clusters (GCs) around twelve early-type galaxies, nine of which have not been published previously. Combining space-based and multi-colour wide field ground-based imaging, with spectra from the Keck DEIMOS instrument, we obtain an average of 160 GC radial velocities per galaxy, with a high velocity precision of  $\sim 15 \text{ km s}^{-1}$  per GC. After studying the photometric properties of the GC systems, such as their spatial and colour distributions, we focus on the kinematics of metal-poor (blue) and metal-rich (red) GC subpopulations to an average distance of  $\sim 8$  effective radii from the galaxy centre.

Our results show that for some systems the bimodality in GC colour is also present in GC kinematics. The kinematics of the red GC subpopulations are strongly coupled with the host galaxy stellar kinematics. The blue GC subpopulations are more dominated by random motions, especially in the outer regions, and decoupled from the red GCs. Peculiar GC kinematic profiles are seen in some galaxies: the blue GCs in NGC 821 rotate along the galaxy minor axis, whereas the GC system of the lenticular galaxy NGC 7457 appears to be strongly rotation supported in the outer region.

We supplement our galaxy sample with data from the literature and carry out a number of tests to study the kinematic differences between the two GC subpopulations. We confirm that the GC kinematics are coupled with the host galaxy properties and find that the velocity kurtosis and the slope of their velocity dispersion profiles is different between the two GC subpopulations in more massive galaxies.

**Key words:** galaxies:star clusters – galaxies:evolution – galaxies: kinematics and dynamics – GCs

## 1 INTRODUCTION

The reconstruction of the evolutionary history of galaxies in the local universe requires a comprehensive knowledge of their chemo-dynamic properties at all scales. Along these lines, the ATLAS<sup>3D</sup> project (Cappellari et al. 2011) has carried out a rich survey of galaxies employing an integral field unit (IFU) technique to map out the chemo-dynamics of galaxies within 1 effective radius ( $R_{\text{eff}}$ ). However, such a radius encloses  $< 10\%$  of the total galaxy mass (baryonic + dark) and hence it may not be representative of

the overall galaxy (e.g., Proctor et al. 2009). In contrast, beyond this radius ( $R_{\text{eff}} > 1$ ), the halo of the galaxy contains precious dynamical signatures of early merging or early collapse events that might have eventually built up the galaxy (Hopkins et al. 2009, 2010; Oser et al. 2010; Hoffman et al. 2010). Some recent examples of the dynamical studies of the outskirts of galaxies beyond the Local Group has mainly involved a few deep long-slit observations (e.g., Coccato et al. 2010), the pioneering technique of Proctor et al. (2009) and Norris et al. (2008) that probed the two-

dimensional stellar kinematics to  $3R_{\text{eff}}$ , and extragalactic planetary nebulae (PNe, Coccato et al. 2009) that can probe the galaxy potential up to  $\sim 10R_{\text{eff}}$ .

Often labeled the “fossil record” of galaxy formation, GCs have been used to study galaxy haloes. GC systems have been found in galaxies of all morphological type and they extend beyond the detectable galaxy diffuse light, probing galactocentric distances  $\geq 10R_{\text{eff}}$  where there are only a few other gravitational constraints (Rhode & Zepf 2001, 2004; Dirsch et al. 2003; Tamura et al. 2006; Forbes et al. 2011). Moreover, their old ages ( $> 10$  Gyr, Kissler-Patig et al. 1998; Cohen et al. 1998; Beasley et al. 2000; Forbes et al. 2001; Schroder et al. 2002; Brodie & Larsen 2002; Beasley et al. 2004; Strader et al. 2005) suggest they have survived violent merging events, preserving the chemo-dynamical record of their parent galaxies.

Moreover, the well-studied dichotomy observed in the colour distribution of most GC systems (Zepf & Ashman 1993; Ostrov et al. 1993; Whitmore et al. 1995; Gebhardt & Kissler-Patig 1999; Larsen et al. 2001; Kundu & Whitmore 2001; Peng et al. 2006; Sinnott et al. 2010) is thought to stem from different formation mechanisms that shaped the underlying host galaxy (Ashman & Zepf 1992; Forbes et al. 1997; Côté et al. 1998). Although the reality of the GC metallicity bimodality has been recently called into question as the result of a strongly non-linear color-metallicity relation (Yoon et al. 2006, 2011; Blakeslee et al. 2010), observations have shown that physical dissimilarities exist among these two subpopulations (Côté 1999; Brodie & Strader 2006; Peng et al. 2006; Chies-Santos et al. 2011; Forbes et al. 2011). For instance, the two GC subpopulations are found to have different physical sizes (Kundu & Whitmore 2001; Jordán et al. 2005; Masters et al. 2010) and diverse spatial distributions around the host galaxy, with the metal-rich (red) GCs more centrally concentrated than the metal-poor (blue) GCs (Geisler et al. 1996; Ashman & Zepf 1998; Brodie & Strader 2006; Bassino et al. 2006; Faifer et al. 2011; Strader et al. 2011; Forbes et al. 2012).

Current spectroscopic studies of GC systems have shown that the kinematics (e.g. rotation directions and rotation amplitudes) of the two GC subpopulations are somewhat diverse. The kinematics of the red GCs is usually akin to that of the host galaxy stars (Schuberth et al. 2010; Strader et al. 2011), perhaps due to a similar formation history (Shapiro et al. 2010). Whereas, the velocity dispersion of the blue GCs is typically larger than that of the red GCs (e.g., Lee et al. 2008). Also intriguing is the fact that rotation has been detected for both the blue and the red GCs, regardless the mass or morphology of the host galaxy (Foster et al. 2011; Arnold et al. 2011).

Interpreting this variety of GC kinematics in the context of galaxy and GC formation has been limited due to the low number of galaxies with large GC radial velocity datasets. To date, this set includes only a dozen GC systems, most of which are nearby very massive ellipticals (see Lee et al. 2010, for a summary). On the other side, numerical simulations on this front have mainly focused on the origin of GC metallicity and colour bimodality (e.g., Weil & Pudritz 2001; Kravtsov & Gnedin 2005; Yoon et al. 2006, 2011), rather than on GC kinematic properties (e.g., Bekki et al. 2005, 2008; Prieto & Gnedin 2008).

This scenario has left open several questions regarding the kinematics of GC systems: does the colour bimodality also imply kinematic bimodality? If so, do the kinematical differences between the blue and red GC subpopulations found in the most massive ellipticals also hold for  $\sim L^*$  galaxies over the whole early-type sequence of the Hubble diagram? Furthermore, do the blue

and red GC subpopulations rotate faster in the outer regions, as predicted in a formation in a disk-disk merging scenario (Bekki et al. 2005)? Can GC kinematics contribute to our understanding of the formation of lenticular galaxies (e.g., Barr et al. 2007)?

We have been carrying out a project named SLUGGS<sup>1</sup> to investigate the GC systems in external galaxies (Brodie et al. 2012, in preparation). SLUGGS is the SAGES Legacy Unifying Globulars and Galaxies Survey, where SAGES is the Study of the Astrophysics of Globular Clusters in Extragalactic Systems. This survey exploits the combination of Subaru/Suprime-Cam wide-field imaging with spectra from the Keck/DEIMOS multi-object spectrograph. The results released so far have shown that the wide-field imaging can give clues about assembly history of the host galaxy (Blom et al. 2011; Forbes et al. 2011). If combined with the high velocity resolution of DEIMOS, this dataset can unravel, at the same time, the dynamics and the metallicity of the field stars (Foster et al. 2009; Proctor et al. 2009) and of the GCs (Foster et al. 2011; Arnold et al. 2011) deep into the galaxy halo, as well as a giving compelling view of galaxy dynamics (Strader et al. 2011; Romanowsky et al. 2009, 2011).

In this work, we aim to study the GC kinematics for an unprecedented large sample of early-type galaxies (ETGs) with high-quality data. We investigate the global kinematics of blue and red subpopulations to study how they, and the underlying galaxy itself, formed. We also supplement our galaxy sample with literature data, and we compare the properties of this large sample with the existing numerical predictions.

The plan of this paper is as follows. From Section 1 to Section 5 we describe the reduction and the analysis of both the photometric and the spectroscopic data. In Section 5, we briefly discuss the significant findings for each galaxy. In Section 6, we give an overview on the current state of the GC formation models in order to compare their predictions to our generic results discussed in Section 7. In Section 8 we supplement our galaxy sample with data from the literature. In Section 9 we analyse the enlarged GC system dataset (our data plus literature) and discuss the results in Section 10. The summary of the paper is given in Section 11.

## 2 THE SAMPLE

In this paper we discuss a subset sample from our survey. This includes nine new galaxies, in addition to other three galaxies already published: NGC 4494 (Foster et al. 2011), NGC 3115 (Arnold et al. 2011) and NGC 4486 (Strader et al. 2011). The analysis and the specific results for these three galaxies have been extensively discussed in the respective papers. Therefore, their overall results will be discussed together with the other nine starting from Section 7.

The physical characteristics of the twelve galaxies are listed in Table 1, with their optical images shown in Figure 1. This galaxy sample extends the study of extragalactic GC systems into a new regime, because it is representative of a wide range of luminosity, morphological type (from lenticulars to giant ellipticals) and environment (from field to clusters), with a velocity resolution three times better than typical previous studies. This improvement is shown in Figure 2 in which we compare the intrinsic properties of our dataset with previous GC studies (that have employed various

<sup>1</sup> <http://sluggs.swin.edu.au/>

Galaxy ID (1)	Hubble Type (2)	$V_{\text{sys}}$ [km s $^{-1}$ ] (3)	$R_{\text{eff}}$ [arcsec] (4)	$(m - M)$ [mag] (5)	$D$ [Mpc] (6)	$M_K$ [mag] (7)	$A_K$ [mag] (8)	$PA_K$ [degree] (9)	$(b/a)_K$ (10)
NGC 0821	E6	1718	51	31.85	23.4	-24.0	0.040	31	0.62
NGC 1400	SA0	558	31	31.05	26.8	-23.8	0.024	29	0.90
NGC 1407	E0	1779	72	32.30	26.8	-25.4	0.025	70	0.95
NGC 2768	E6	1353	93	31.69	21.8	-24.7	0.016	91	0.46
NGC 3377	E6	690	46	30.19	10.9	-22.7	0.013	46	0.58
NGC 4278	E2	620	34	30.97	15.6	-23.8	0.010	219	0.91
NGC 4365	E3	1243	60	31.84	23.3	-25.2	0.008	41	0.74
NGC 5846	E0	1712	61	31.92	24.2	-25.0	0.020	233	0.92
NGC 7457	S0	844	52	30.55	12.9	-22.4	0.019	125	0.54
NGC 3115	S0	663	85	29.87	9.4	-24.0	0.017	43	0.45
NGC 4486	E0	1284	81	31.18	17.2	-25.3	0.008	151	0.86
NGC 4494	E1	1344	53	31.10	16.6	-24.2	0.008	173	0.87

**Table 1.** General properties of our galaxy sample. The galaxy name (1) and Hubble Type (2) are from the NED database. The galaxy systemic velocity (3) and ellipticity corrected effective radius (4) are from Cappellari et al. (2011), otherwise from NED and the RC3 catalogue (de Vaucouleurs 1991) if not in Cappellari et al. (2011). The distance modulus (5) and the respective distance in Megaparsec (6) are from Tonry et al. (2001) with a  $-0.06$  correction as advocated by Mei et al. (2007), respectively. If the galaxy is in the ACS Virgo Survey, we use the distances from Mei et al. (2007). We assume that NGC 1407 and NGC 1400 lie at the same distance, computed as the average of the respective Tonry et al. (2001) distances. The  $K$  band absolute magnitude (7) is from 2MASS apparent magnitude at the distances given in column 6 and corrected for the foreground Galactic extinction given in column 8 (NED database). The photometric position angle (9) and axis ratio (10) are from 2MASS (Skrutskie et al. 2006). The last three galaxies have been analysed in separate papers (see text).

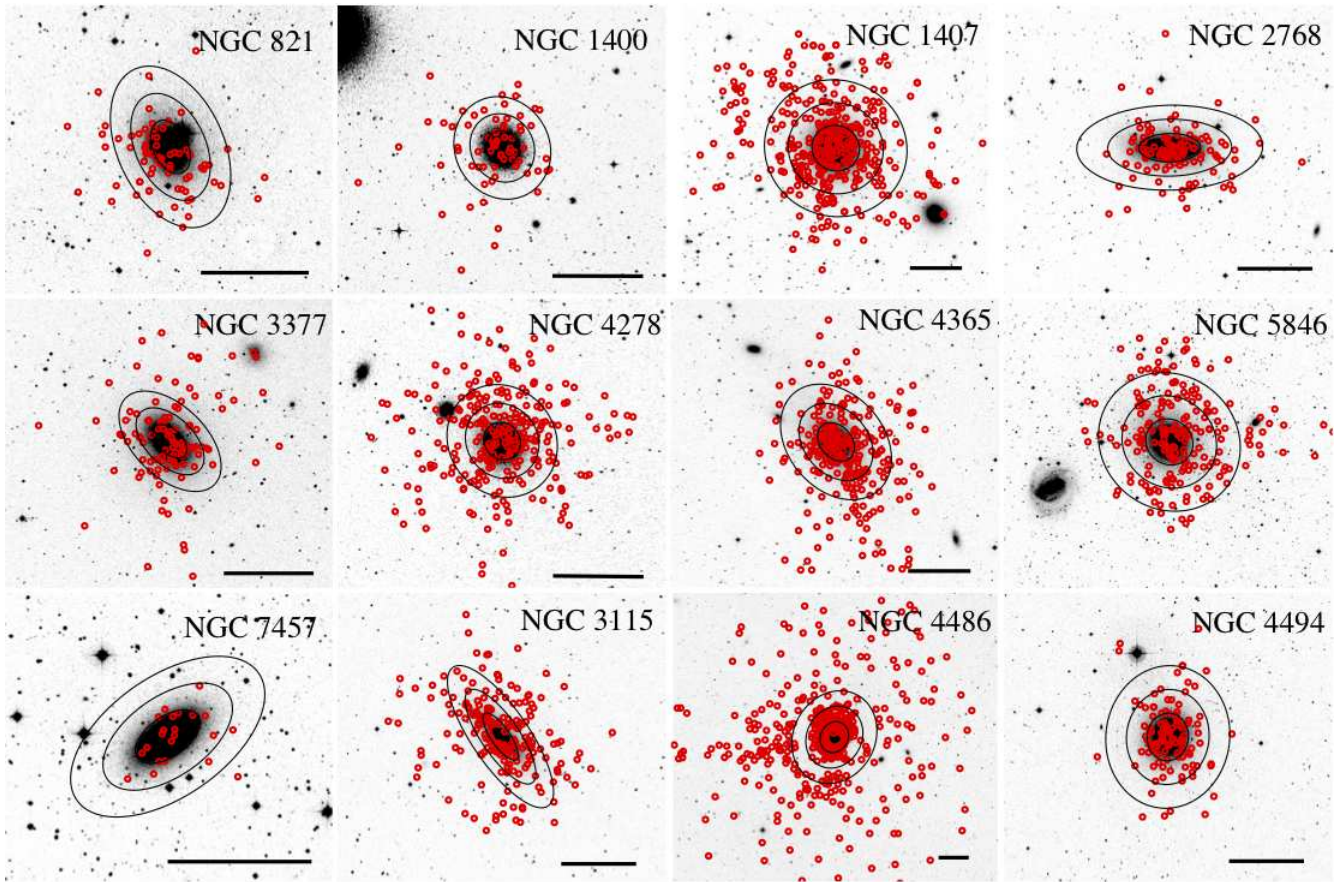


**Figure 1.** Digitalized Sky Survey (DSS) images of our galaxy sample. Red circles and black ellipses represent the spectroscopically confirmed GCs found in this work and the 2, 4, 6  $R_{\text{eff}}$  schematic isophotes corrected for the galaxy ellipticity respectively. The black line on the bottom-right spans 5 arcmin in length. North up and the East on the left. The elliptical galaxy south-west of NGC 1407 is NGC 1400 whose GC system is shown separately in this figure. The last three galaxies have been analysed in separate papers.

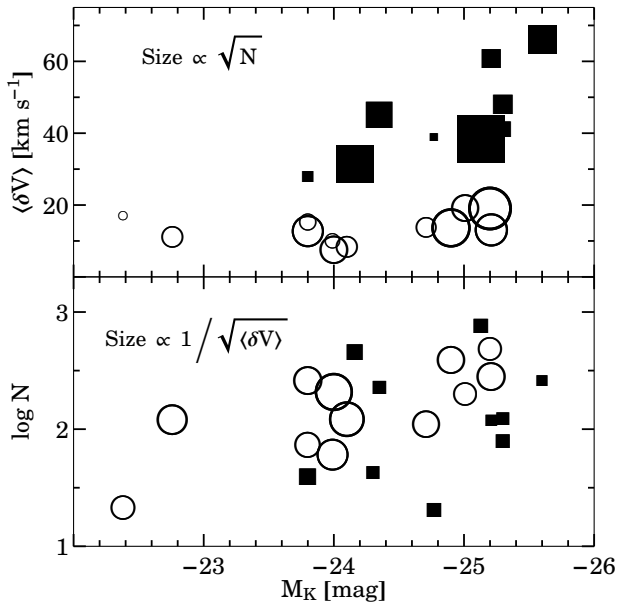


**Figure 2.** Accuracy of GC radial velocity measurements. Open circles and open boxes represent our GC data and literature data, respectively. Literature data will be discussed in Section 8. *Top panel.* The median velocity uncertainty  $\langle \delta V \rangle$  per GC system are shown as a function of absolute magnitude in the K band. Symbol sizes are  $\propto \sqrt{N}$ , where  $N$  is the number of spectroscopically confirmed GCs per galaxy. *Bottom panel.*  $\log N$  is shown as a function of the absolute magnitude in the K band, where symbol sizes are  $\propto 1/\sqrt{\langle \delta V \rangle}$ . Our data extend the range of galaxy luminosity probed with three times better velocity accuracy.

instruments including VLT/FLAMES, VLT/FORS2, Keck/LRIS or Gemini/GMOS).

### 3 PHOTOMETRIC OBSERVATIONS AND DATA ANALYSIS

#### 3.1 Subaru data

Multi-band photometric observations were carried out using the Subaru/Suprime-Cam instrument with a field of view of  $34 \times 27$  arcmin<sup>2</sup> and a pixel scale of 0.202 arcsec (Miyazaki et al. 2002). The galaxy sample was observed in the period between 2005 and 2010 with a standard Sloan Digital Sky Survey (SDSS) *gri* filter set. NGC 2768 and NGC 4278 were both downloaded from the SMOKA archive (Baba et al. 2002) and were observed with a *Rciz* and *BVI* filter set, respectively. For NGC 1407 and NGC 4365 we present existing Suprime-Cam photometry published in Spitler et al. (2012) (see also Romanowsky et al. 2009) and Blom et al. (2011), respectively. For these two galaxies both the imaging reduction and the catalogue extraction were performed with the methodology described in this paper. NGC 7457 is the only galaxy for which no Subaru imaging is available, and therefore we use WIYN/Minimosaic imaging in *BVR* filters presented in Hargis et al. (2011) and we refer to this paper for a description of the data reduction.

In Table 2 the imaging observations are summarized. The overall seeing conditions were mainly sub-arcsec. For NGC 821 (*g* band), NGC 5846 (*g* band) and NGC 4278 (*B* band) the data suffer from cloudy conditions and poor ( $\geq 1$  arcsec) seeing.

Subaru raw images were processed using the SDFRED data

pipeline (Ouchi et al. 2004) that yields standard flat field corrected images for each of the three filters. Photometric point source catalogues were extracted using standard IRAF/DAOPHOT aperture photometry routines. We summarise here the main steps of the data reduction and we refer to Section 3 of Blom et al. (2011) for a detailed description of the method.

We obtain a raw list of object positions by running IRAF/DAOFIND on galaxy subtracted images in order to optimise the finding algorithm. The extraction threshold was typically set between 2 and 4 times the background depending on the filter and on the seeing conditions. The galaxy light was modelled with IRAF/ELLIPSE set to allow the position angle and ellipticity to vary. Next, we perform aperture photometry using IRAF/PHOT on the preselected objects for a certain number of circular apertures from 1 up to 15 pixels (equivalent to  $\sim 0.2$  arcsec to 3 arcsec for the Suprime-Cam pixel scale). The extraction radius was chosen in order to maximise the signal of the source and minimise the sky contribution. The extracted magnitude was corrected for the computed aperture correction using IRAF/MKAPFILE. Photometric zeropoints were estimated by bootstrapping the Suprime-Cam photometry to the Sloan Digital Sky Survey (SDSS) DR7 photometric system (Abazajian et al. 2009) using the brightest objects in common between the two datasets (typically with  $17 < i < 21$ ). If not in SDSS, the zeropoints were calibrated using the flux from standard stars observed over the same night. Finally, we use the reddening given in Table 1 and the conversion table of Schlegel et al. (1998) to derive the Galactic extinction correction in our photometric bands. Hereafter, all magnitudes and colours are extinction corrected.

#### 3.2 HST data

We use *Hubble Space Telescope* (*HST*) archive images from the Advanced Camera for Surveys (ACS) and Wide Field Planetary Camera 2 (WFPC2) to improve the quality of the photometric selection in the central regions of our galaxies. For most of them, we exploit existing photometric GC catalogues and we refer to the following authors for a detailed description of the data reduction and analysis: Spitler et al. (2008) for NGC 821, Forbes et al. (2006) for NGC 1407 and NGC 1400, Forbes et al. (1996) for NGC 5846, Chomiuk et al. (2008) for NGC 7457 and Blom et al. (2011) for NGC 4365.

We obtained, from the Hubble Legacy Archive, new *HST*/ACS imaging for NGC 3377, NGC 2768 and NGC 4278, respectively. The ACS camera has a pixel scale of 0.05 arcsec and a field of view of  $3.36 \times 3.36$  arcmin<sup>2</sup>.

The NGC 3377 imaging consists of one pointing in F475W ( $\sim$  Sloan *g*) and F850LP ( $\sim$  Sloan *z*) filters and it was observed as part of the *HST* project ID 10554. NGC 2768 (ID 9353) was imaged in F435W, F555W, F814W filters, equivalent to a *BVI* configuration, respectively. Finally, the NGC 4278 (ID 10835) data consists of four pointings in F475W and F850LP filters that probe the galaxy up to  $\sim 6$  arcmin from the centre (Usher et al. 2012, in preparation).

The *HST* imaging was reduced and analysed using a custom built pipeline to find point-like sources and measure their magnitudes and half light radii. For details on the methods used by the pipeline including point spread function determination, we refer to Strader et al. (2006) and to Spitler et al. (2006). The extracted magnitudes and sizes for GCs in NGC 3377 and NGC 4278 were compared with those published by Chies-Santos et al. (2011) for objects in the NGC 3377 pointing and in the two NGC 4278 point-

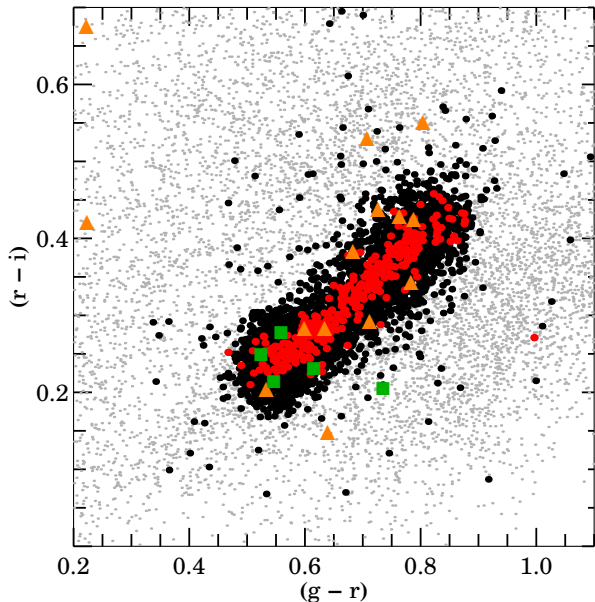


**Figure 3.** Colour-colour diagram of objects around NGC 1407. Grey and black points represent all the sources detected in the Suprime-Cam field-of-view and all the photometrically selected GCs with  $i < 25$  and  $i < 24$ , respectively. Spectroscopically confirmed sources are shown as red points (GCs), green boxes (Galactic stars) and orange triangles (galaxies) respectively.

ings. Both magnitudes and sizes show good agreement without any evidence of statistically significant offset from the published data.

### 3.3 Photometric GC selection

Once the point-source catalogues have been constructed, they are photometrically selected to avoid contamination, such as unresolved galaxies and Galactic stars. As far as our new Subaru data are concerned, this process involves the following steps: (i) selection in a colour-colour space; (ii) selection in a colour-magnitude space; (iii) a visual check. The GC selection in the ground-based imaging for NGC 7457 was carried out in Hargis et al. (2011) and we refer to this paper for a detailed description of their selection method. The steps listed above are subjected to variations in the procedures for the DEIMOS mask design.

GCs are known to populate a specific area of colour-colour diagrams (e.g., Rhode & Zepf 2001; Faifer et al. 2011; Chies-Santos et al. 2011). With a *gri* filter set, this is enclosed within  $0.4 \lesssim (g-i) \lesssim 1.5$ ,  $0 \lesssim (r-i) \lesssim 0.6$ ,  $0.3 \lesssim (g-r) \lesssim 0.9$  where these boundaries run diagonally to the colour axes, as shown in Figure 3 for the galaxy NGC 1407. To take into account the dependence of the colour boundaries on the quality of the data, we flag as GC candidates all the objects deviating by less than  $2\sigma$  from these boundaries (Spitler et al. 2008).

Next, we apply a cut on the  $i$  band magnitude ( $I$  band for NGC 4278). Given the ongoing debate regarding the uncertain separation between GCs and ultra compact dwarfs (UCDs, Mieske et al. 2006; Brodie et al. 2011), we decided to set the upper brightness magnitude at  $M_i \approx -11.6$  ( $M_I \approx -12$ ), one magnitude brighter than the integrated magnitude of  $\omega$  Cen, the brightest GC in the Milky Way. Nevertheless, in some cases we relax this criterion in order to include spectroscopically confirmed GCs that have magnitudes brighter than the set threshold. The separation be-

Galaxy ID	Obs date	Filters	Exp. time [sec]	Seeing [arcsec]
NGC 0821	2008 Nov.	<i>gri</i>	960, 350, 220	1.2, 1.0, 0.8
NGC 1400	2008 Nov.	<i>gri</i>	3240, 3600, 10800	0.6, 0.6, 0.6
NGC 1407	2008 Nov.	<i>gri</i>	3240, 3600, 10800	0.6, 0.6, 0.6
NGC 2768	2005 Mar.	$R_{Ciz}$	600, 100, 210	0.6, 0.6, 0.6
NGC 3377	2008 Nov.	<i>gri</i>	500, 450, 375	0.9, 0.7, 0.8
NGC 4278	2002 Feb.	<i>BVI</i>	600, 450, 360	1.4, 0.9, 0.9
NGC 4365	2008 Apr.	<i>gri</i>	650, 350, 300	0.8, 0.8, 0.8
NGC 5846	2009 Apr.	<i>gri</i>	2760, 1606, 1350	1.0, 0.6, 0.8
NGC 7457	2009 Oct.	<i>BVR</i>	6300, 6000, 7200	0.7, 0.8, 0.7

**Table 2.** Summary of the ground-based imaging observations. The galaxy name, observation date, filters employed, together with the respective exposure time and seeing are listed. All the observations were performed using Subaru/Suprime-Cam, except for NGC 7457 observed with WIYN/MiniMo (Hargis et al. 2011).

tween NGC 1407 and NGC 1400 objects will be discussed in Section 5.

Next, we calculate the radius at which the number of GC candidates per unit area flattens out (see §3.5 for the method), that is an estimate of the radius at which the contribution of the contaminants (Galactic stars and high redshift galaxies) becomes dominant. Therefore, we count out of the GC selection all the objects outside this background radius. We have tested that the effect of the contaminants on the GC colour distribution is minimal ( $< 0.1$ ) mag and that it does not affect considerably the GC colour bimodality (see also, Arnold et al. 2011).

Finally, we perform a visual check to make sure that no outliers, such as extended sources or image artefacts, contaminate the final GC catalogue. Most of the outliers turned out to be close to the galaxy (within 1 arcmin) where the galaxy light contamination and the crowded field makes the Subaru photometry unreliable. Within this radius, the contribution of the *HST* imaging becomes crucial.

As far as the *HST*/ACS imaging is concerned, it is worth noting that the diffraction limited quality of *HST* imaging has the advantage of making extragalactic GCs partially resolved for all of our galaxies. Therefore, the GC selection in our space-based imaging is also based on a size selection in addition to magnitude and colour-colour criteria (if available). In NGC 3377 and NGC 4278, for which only  $g$  and  $z$  imaging are available, we flag as GC candidates all the objects with colour  $0.7 < (g-z) < 1.6$  and sizes  $0.1 < r_h < 20$  pc. Such a choice is motivated by the clear drop off in the density of the objects outside the adopted colour cut, as observed in Blom et al. (2011). For NGC 2768, we adopt the same size-cut as above and select objects within  $0.4 < (B-V) < 1.2$  and  $0.8 < (V-I) < 1.4$  and an upper magnitude of  $M_I \approx -12$ . In Figure 4, the colour-magnitude diagrams of the GC candidates and of the spectroscopically confirmed GCs are shown.

### 3.4 GC colour bimodality

To probe bimodality, we use a Kaye’s Mixture Model algorithm (KMM, Ashman et al. 1994) that returns colour peaks, variance and number of objects in the detected subpopulations. KMM was run on all the  $(g-i)$  distributions of the Subaru GC candidates brighter than the turnover magnitude  $M_{\text{TOM}}$ . In this paper we adopt  $M_{\text{TOM},i} \equiv 8.00 \pm 0.03$ , derived using the  $i-I$  transformation from Faifer et al. (2011) to calibrate the  $I$  band TOM given by Kundu & Whitmore (2001) into our photometric system.

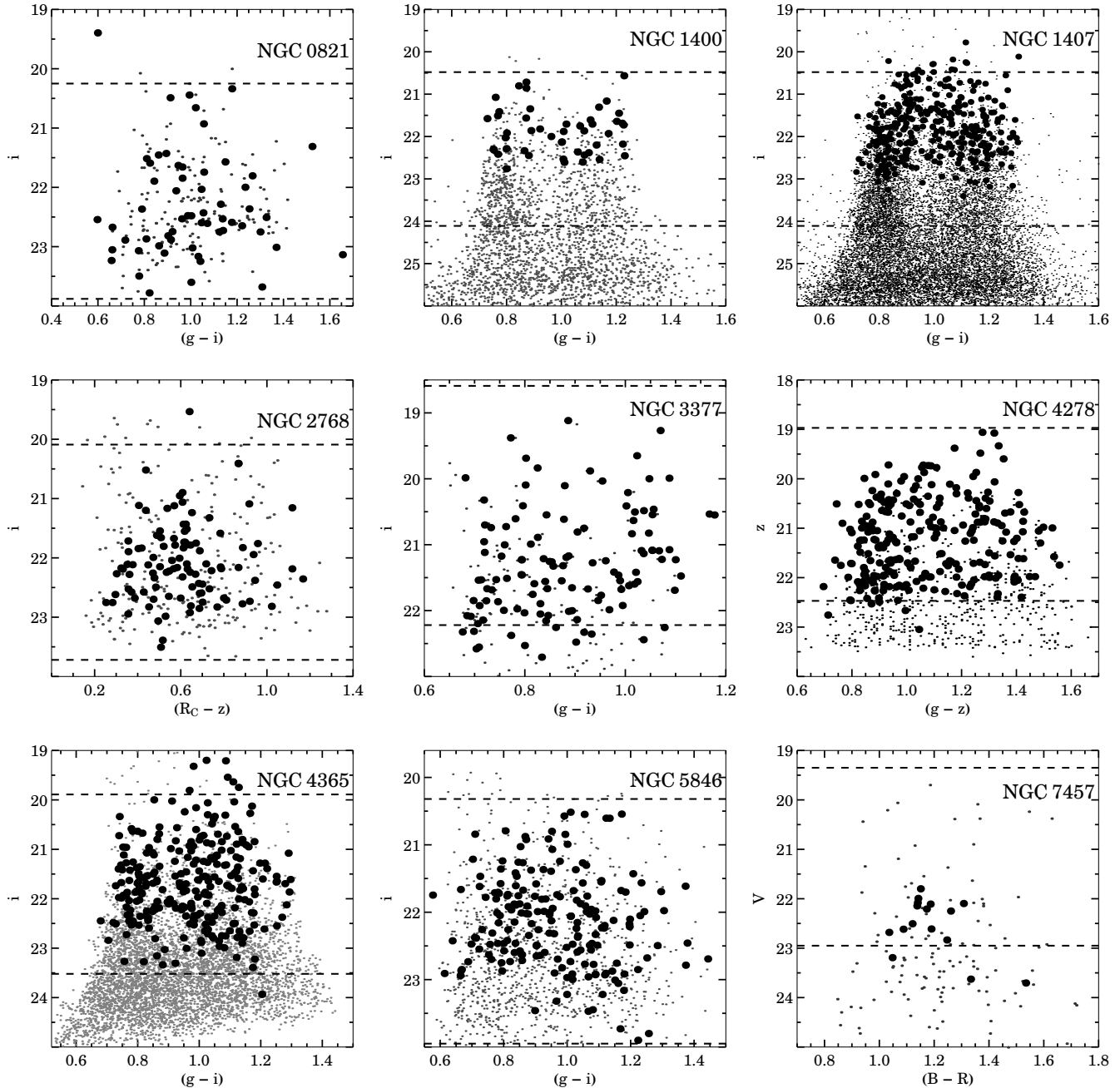


**Figure 4.** GC system colour-magnitude diagrams. Photometrically selected GCs and spectroscopically confirmed GCs are shown as small and large black points respectively. Upper and bottom dashed lines represent the  $\omega$  Cen magnitude ( $M_i \approx -11.6$ ) and the GC turnover magnitude ( $M_{\text{TOM},i} \equiv -8$  mag) at the distances given in Table 1.

For NGC 2768, NGC 7457 and NGC 4278, we study the  $(R_C - z)$ ,  $(B - V)$  and  $(g - z)$  colour distributions respectively. We perform a bisector fit (Feigelson & Babu 1992) to the bright GCs in common between the *HST* and Subaru images, in order to convert *HST* magnitudes of the spectroscopically confirmed GCs into the respective Subaru photometric system. For NGC 4278, given the wide spatial coverage and better quality of its *HST* data, we transform Subaru magnitudes of the confirmed GCs into the *HST* photometric system. Results of the KMM analysis are presented in Table 3. We find that eight out of nine galaxies show significant GC

colour bimodality. GCs are divided into blue and red according to the local minimum of the best fit Gaussians in Figure 5.

### 3.5 GC spatial distribution

We construct projected surface density profiles for the GC subpopulations of our galaxy sample. GC candidates brighter than the turnover magnitude were binned in circular annuli and corrected for areal incompleteness. The Subaru dataset was supplemented with *HST* photometry, in order to probe the GC surface density in the inner regions. An important caveat to bear in mind is that we

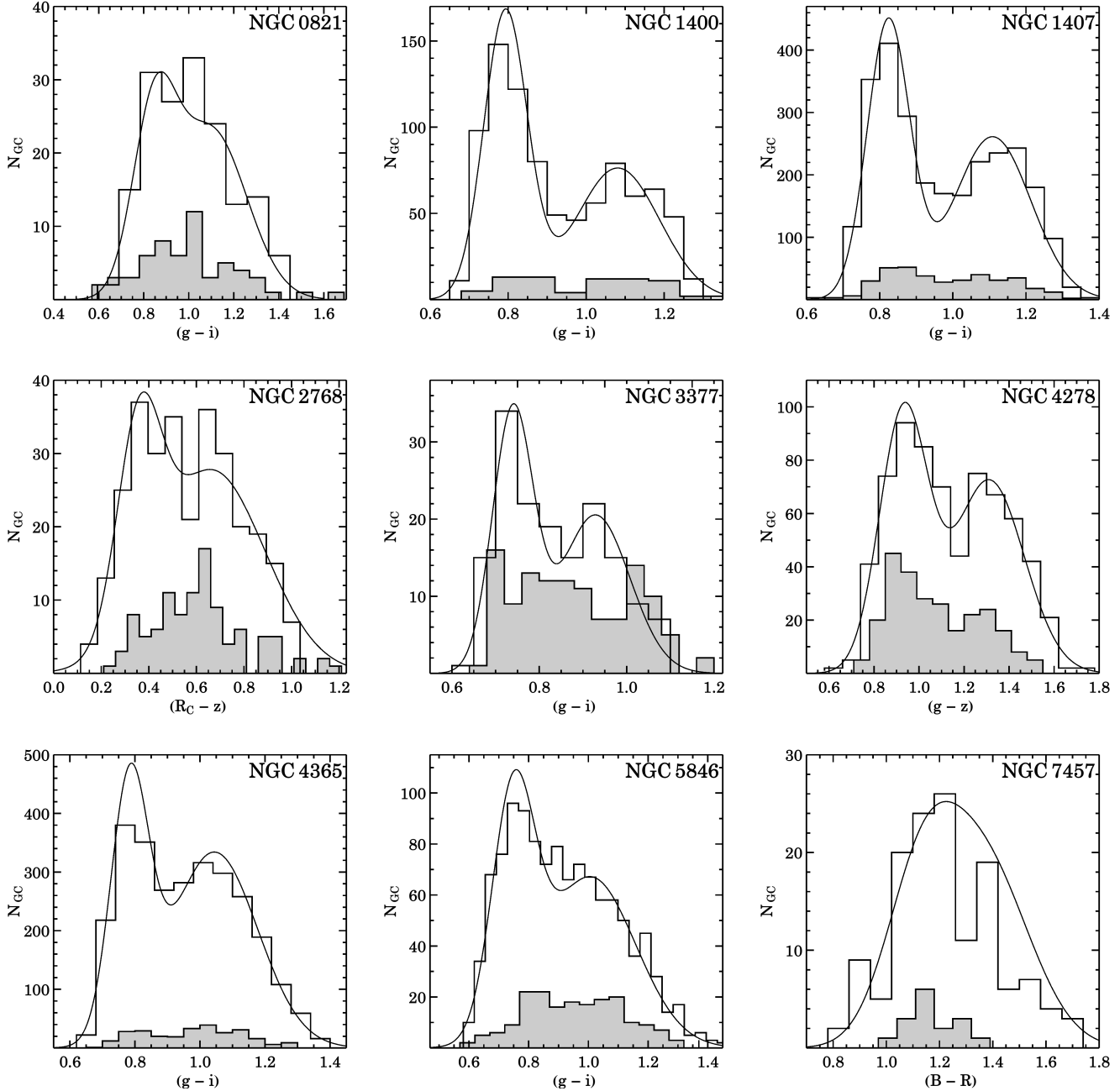


**Figure 5.** Colour histograms of our galaxy sample. GC candidates and spectroscopically confirmed GCs are shown as empty and grey filled histograms respectively. For NGC 1407, we only show GCs with  $i < 23$ . Solid lines show the sum of the KMM fits of the two subpopulations. No significant bimodality was detected in NGC 7457. The dearth of red GCs in NGC 3377 is due to the fact that we have excluded all the GC candidates within 1 arcmin from the centre. The magnitude of these objects turned out to be corrupted by the underlying diffuse stellar light.

do not correct the Subaru dataset for magnitude incompleteness. This effect becomes important especially for objects fainter than  $i \sim 23.5$  in the innermost regions ( $\sim 1$  arcmin) where the detection of sources is inhibited by the surface brightness contribution of the host galaxy (Faifer et al. 2011). Conversely, the completeness of the *HST* photometry in  $z$  ( $V$ ) band is typically above 90 (70) per cent at the turnover magnitude even in the innermost regions, respectively (Larsen et al. 2001; Jordán et al. 2007). Therefore, we select all the GCs brighter than the turnover magnitude (see Figure 4) and we use circular radial bins in common between *HST* and

Subaru to correct and adjust the Subaru GC surface density to that of the *HST* data. Although the matching between *HST* and Subaru data points is arbitrary, this approach preserves the relative slopes of the spatial distribution of the two subpopulations and allows us to verify whether or not blue and red GC subpopulations show different spatial distributions around the host galaxy as found from previous authors (e.g., Bassino et al. 2006).

Next, we fit the resulting (*HST* + Subaru) GC density profile  $N(r)$  with a Sérsic law (Sérsic 1963) similar to that commonly carried out for galaxy surface brightness profiles, but in practice

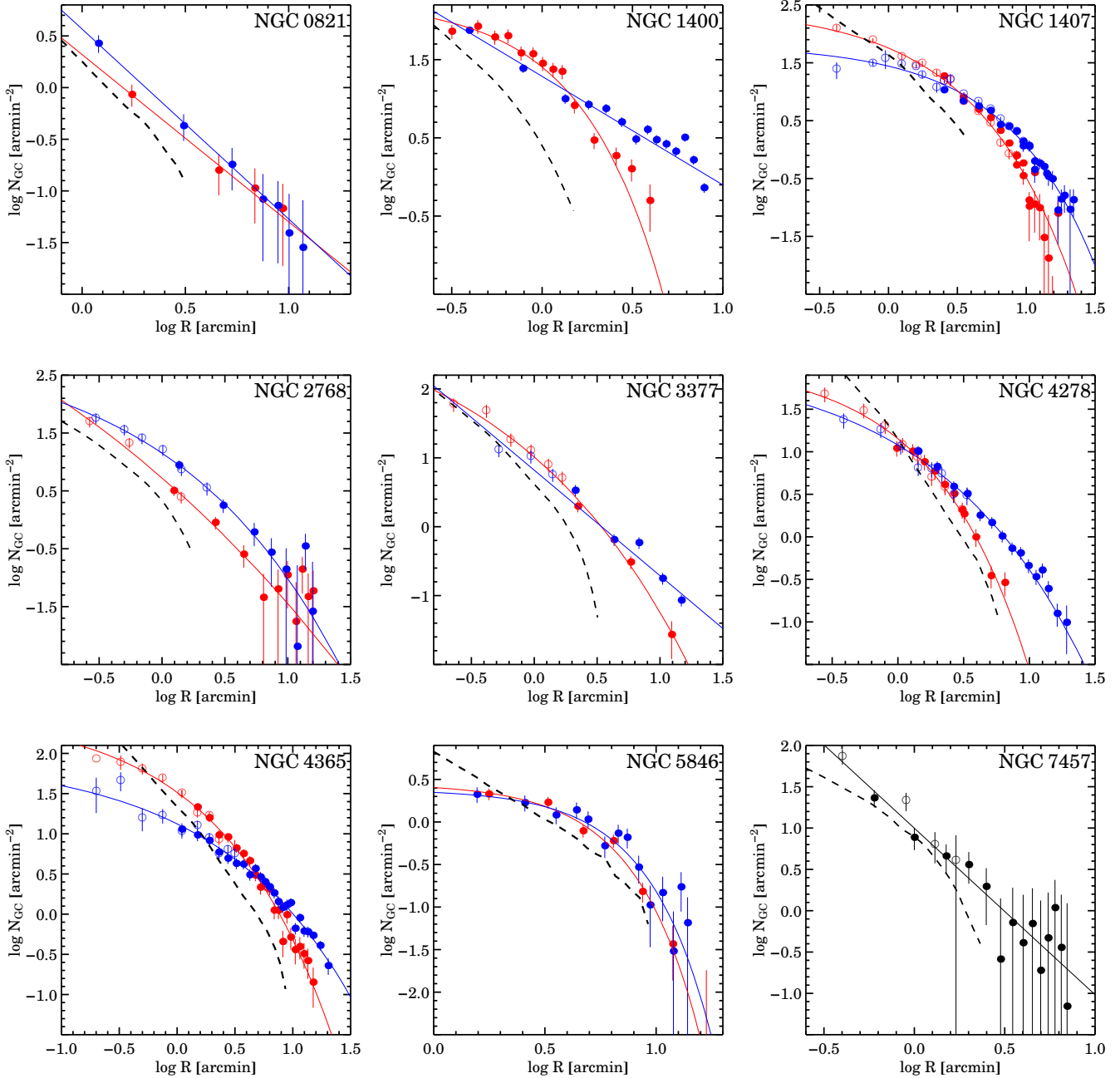


**Figure 6.** Surface density profiles of the GCs brighter than the turnover magnitude. Blue and red GC subpopulations are shown as blue and red filled points (if from Subaru imaging) and blue and red open circles (if from *HST* imaging) respectively. Sérsic fits or alternatively power-law fits to blue and red GC subpopulations are shown as blue and red lines respectively. For NGC 7457, the surface density and the fit to all GCs are shown as black points and black line respectively. Both the data points and the fits are background subtracted according to eq. 1. Also shown as dashed lines are the scaled and arbitrarily offset stellar surface brightness profiles obtained from Subaru imaging as described in §3.2. For completeness, we also show the surface density profiles from Blom et al. (2011) for NGC 4365 and from Hargis et al. (2011) for NGC 7457, respectively.

we fit a variation of the Sérsic profile from Graham et al. (2005) in order to quantify the background level:

$$N(r) = N_e \exp \left( -b_n \left[ \left( \frac{R}{R_{\text{eff}}} \right)^{1/n} - 1 \right] \right) + bg \quad (1)$$

where  $b_n = 1.9992n - 0.3271$ ,  $n$  is the Sérsic index,  $R_{\text{eff}}$  is the effective radius of the GC system,  $N_e$  is the surface density at that radius and  $bg$  is the background contamination level. In case

a Sérsic fit was not feasible due to small numbers we fit a power-law, i.e.  $N(r) \propto r^\alpha$  that has been also used for similar analyses (Spitler et al. 2008). In Figure 6 the background subtracted GC surface density profiles for our galaxies are shown. As found in other galaxies, the red GCs are more centrally concentrated than the blue GCs (e.g., Geisler et al. 1996; Bassino et al. 2006; Faifer et al. 2011; Strader et al. 2011).

We also compare the GC surface density to the galaxy surface



Galaxy ID	$\mu_{\text{blue}}$	$\mu_{\text{red}}$	$\sigma_{\text{red}}$	$\sigma_{\text{red}}$	p-value	colour
NGC 0821	0.84	1.10	0.09	0.15	0.034	$(g-i)$
NGC 1400	0.79	1.05	0.05	0.11	$10^{-10}$	$(g-i)$
NGC 1407	0.85	0.77	0.05	0.1	$10^{-10}$	$(g-i)$
NGC 2768	0.41	1.10	0.15	0.22	$10^{-5}$	$(R_C - z)$
NGC 3377	0.73	0.93	0.05	0.08	$10^{-6}$	$(g-i)$
NGC 4278	0.93	1.31	0.10	0.16	$10^{-10}$	$(g-z)$
NGC 4365	0.78	1.04	0.05	0.13	$10^{-10}$	$(g-i)$
NGC 5846	0.74	1.00	0.15	0.06	$10^{-5}$	$(g-i)$
NGC 7457	1.12	1.36	0.13	0.17	0.311	$(B-R)$

**Table 3.** KMM results. For each galaxy,  $\mu_{\text{blue}}$  and  $\mu_{\text{red}}$  represent the mean of the blue and red peak respectively, whereas  $\sigma_{\text{blue}}$  and  $\sigma_{\text{red}}$  are the Gaussian  $\sigma$  for each peak. The last column gives the p-value, that is the confidence level with which the hypothesis of an unimodal colour distribution can be rejected (larger confidence for smaller p-values). The last column gives the colour distribution used in the analysis. NGC 7457 is the only galaxy without significant bimodality detected.

brightness for each galaxy, obtained from the Subaru images using IRAF/ELLIPSE as described in §3.2. The surface brightness profiles were corrected for the local galaxy ellipticity and then shifted by an arbitrary constant for comparison purposes (different for each galaxy). Figure 6 shows that, qualitatively, the slope of the red GC subpopulation agrees with that of the surface brightness of the host galaxy.

#### 4 SPECTROSCOPIC OBSERVATIONS AND DATA ANALYSIS

Spectroscopic observations were performed with the DEep Imaging Multi-Object Spectrograph (DEIMOS, Faber et al. 2003) mounted on the 10 m Keck-II telescope. Galaxies were targeted in the period between 2006 and 2011, employing a different number of masks for each galaxy depending on the richness of the GC system. Objects selected for spectroscopic follower were chosen according to their likelihood of being GCs, i.e. giving priority to the objects selected with methods as Section 3.3. The spectroscopic observations are summarized in Table 4.

The large collecting area of the 10-meter Keck primary mirror combined with the  $\sim 16 \times 5$  arcmin<sup>2</sup> of DEIMOS is the ideal combination to investigate the outskirts of galaxies where GCs are expected to be one of the best tracers of the total galaxy potential. For all the galaxies, DEIMOS was set up with the 1200 l/m grating centred on 7800 Å together with 1 arcsec wide slits, allowing coverage of the region between  $\sim 6500 - 8700$  Å with a resolution of  $\Delta\lambda \sim 1.5$  Å. Raw spectra were reduced using the DEIMOS/spec2d reduction pipeline provided online, that produces calibrated and sky subtracted spectra for each slit (Newman et al. 2012; Cooper et al. 2012).

We estimate the radial velocity of the GCs by measuring the Doppler shift of Calcium Triplet (CaT) absorption lines that characterises the infrared part of their spectra at 8498 Å, 8542 Å, 8662 Å, respectively. We measure radial velocities with IRAF/FXCOR that performs a cross-correlation between the Fourier transformed science spectrum and 13 template Galactic star Fourier transformed spectra. The template spectra were observed with the same DEIMOS setup used for scientific spectra and they cover a wide range of spectral type, luminosity and metallicity (from F to M type). Fxcor was configured to have all the science and template spectra in the same wavelength range from 8300 to 8900 Å with

Galaxy ID	Masks	Exp. time [hr]	N <sub>GCs</sub>	N <sub>stars</sub>	N <sub>gal</sub>
NGC 0821	6	9.2	61	10	4
NGC 1400	4	9.0	72	6	27
NGC 1407	9	20	369	5	14
NGC 2768	5	12.7	109	57	9
NGC 3377	4	8.3	126	16	74
NGC 4278	4	8.8	256	44	33
NGC 4365	6	9.0	269	6	49
NGC 5846	6	9.1	195	32	4
NGC 7457	2	4.2	21	14	4
NGC 3115	5	14	190	29	0
NGC 4486	5	5.0	737	116	27
NGC 4494	5	4.6	117	34	108

**Table 4.** Summary of the spectroscopic observations for our twelve galaxies. The table lists the galaxy name and the total number of the DEIMOS masks used. To take into account the different seeing conditions over different nights, we show the effective exposure time weighted by the mean seeing conditions during the observation time as done in Coccato et al. (2009). Also shown are the total number of spectroscopically confirmed GCs (including marginal GCs), Galactic stars and background galaxies respectively. The datasets for NGC 3115 and NGC 4486 also include GCs from external datasets as described in Arnold et al. (2011) and Strader et al. (2011) respectively.

the same DEIMOS spectral resolution. The radial velocity for each object was estimated as the mean of the radial velocity resulting from the correlation with each template star. The respective errors were evaluated by adding in quadrature the default error given by fxcor as described in Tonry & Davis (1979) to the standard deviation among the stellar templates, which is an estimate of the systematics.

##### 4.1 Kinematic selection criteria

Once the final radial velocities of the GC candidates are obtained, we redshift-correct the spectra and perform a visual check to verify that the CaT lines are real and that they lie at the expected rest wavelength. Our selection criteria require the presence of at least two “visible” CaT lines (typically the brightest 8542 Å and 8662 Å lines) and of the H $\alpha$  absorption line at 6563 Å, if probed in the redshift corrected spectra. The visual analysis is performed by at least two members of the team and it produces a final spectroscopic consensus catalogue. Spectra that show a radial velocity consistent with a GC, but for which it was not possible to reach a consensus, were flagged as “marginal” and are not included in the kinematic analysis. These objects have usually low signal-to-noise spectra or suffer from bad sky-line subtraction making the line identification subjective.

Besides background galaxies that can be usually spotted by the emission lines in their spectra, the main outliers of our spectroscopic selection are Galactic stars because they show a stellar spectrum with radial velocity  $V_{\text{rad}} \approx 0 \pm 500$  km s<sup>-1</sup>. In most cases GCs and Galactic stars are well-separated in velocity, but for galaxies with  $V_{\text{sys}} < 1000$  km s<sup>-1</sup> Galactic stars might introduce a low velocity tail in the observed GC candidate velocity distribution. We decided to use a friendless algorithm introduced in Merrett et al. (2003) that flags objects deviating by more than  $n \times \sigma$  from the velocity distribution of their  $N$  nearest neighbours. We use  $n = 3$  and  $10 < N < 20$  (depending on the galaxy) to exclude both

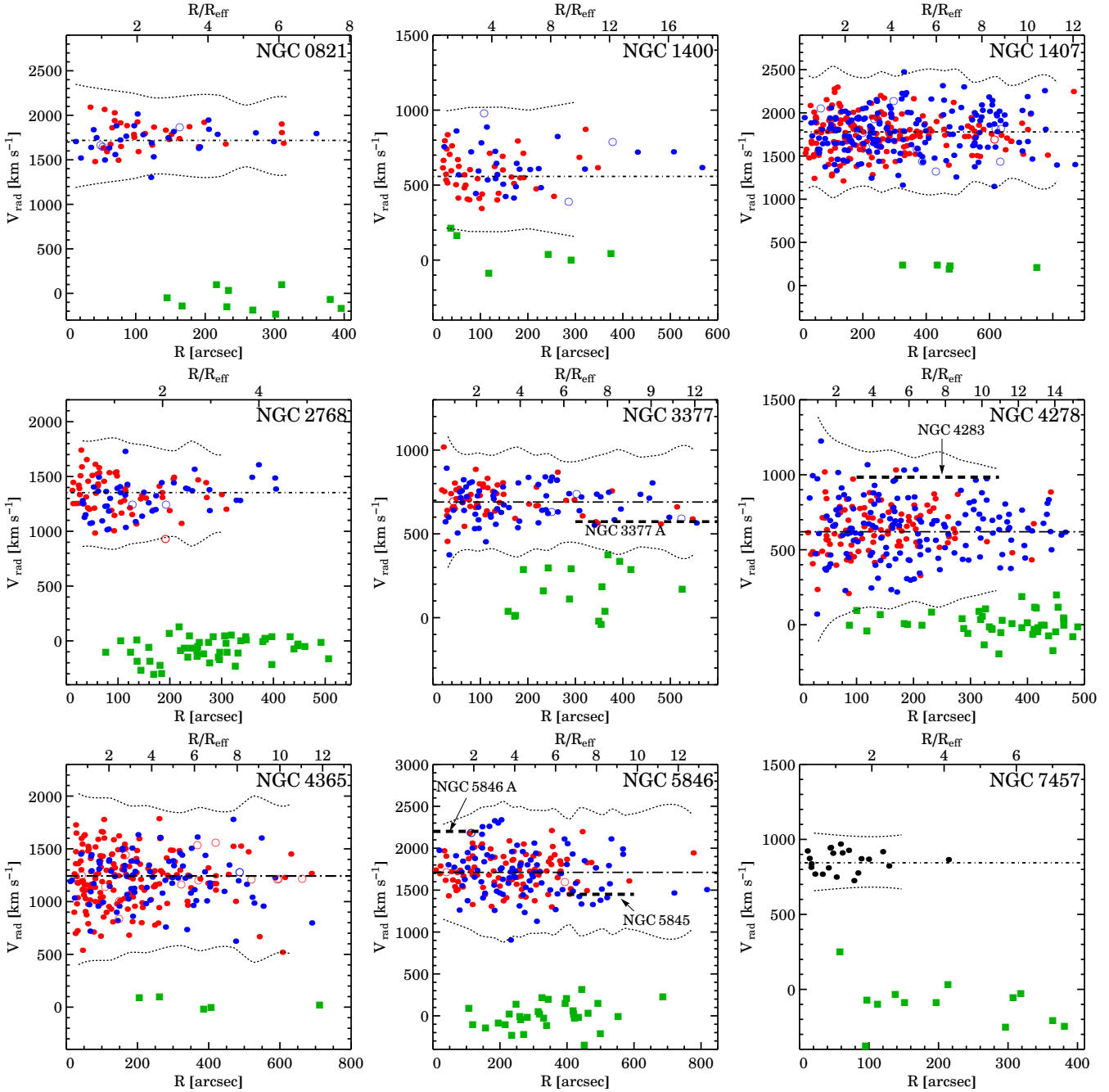


**Figure 7.** GC radial velocity distributions with galactocentric radius. Confirmed GCs, marginal GCs and Galactic stars are shown as filled points, open points and green boxes respectively. GCs are colour coded according to their subpopulation (blue or red) membership. Galactocentric radii have been translated into effective radii on the top axis. Dotted curves and dot-dashed lines are the clipping envelope as defined by the friend-less algorithm (see text) and the galaxy systemic velocities from Table 1, respectively. Also shown as thick dotted lines are the systemic velocities of the galaxies that might contaminate the GC system of the target galaxy. GCs have a mean velocity similar to the galaxy systemic velocity.

stars and possible outliers that lie outside the  $3\sigma$  envelope from the kinematic analysis.

In Figure 7 we show the distribution of all the spectroscopically confirmed GCs and Galactic stars in a radius-velocity phase space. In this plot and hereafter, galactocentric distances are expressed as a equivalent radius, that is defined as:

$$R = \sqrt{qX^2 + \frac{Y^2}{q}}, \quad (2)$$

where  $q$  is the axis ratio defined as the ratio of minor over the major axis of the galaxy (see Table 1),  $X$  and  $Y$  are Cartesian coordinates of an object in the galaxy rest frame, with the origin at the galaxy centre, and with  $X$  and  $Y$  aligned along the photometric major axis and minor axis respectively. The final spectro-photometric catalogues of our galaxy sample are available on-line and they include spectroscopically confirmed GCs, “marginal” GCs, Galactic stars and galaxies.

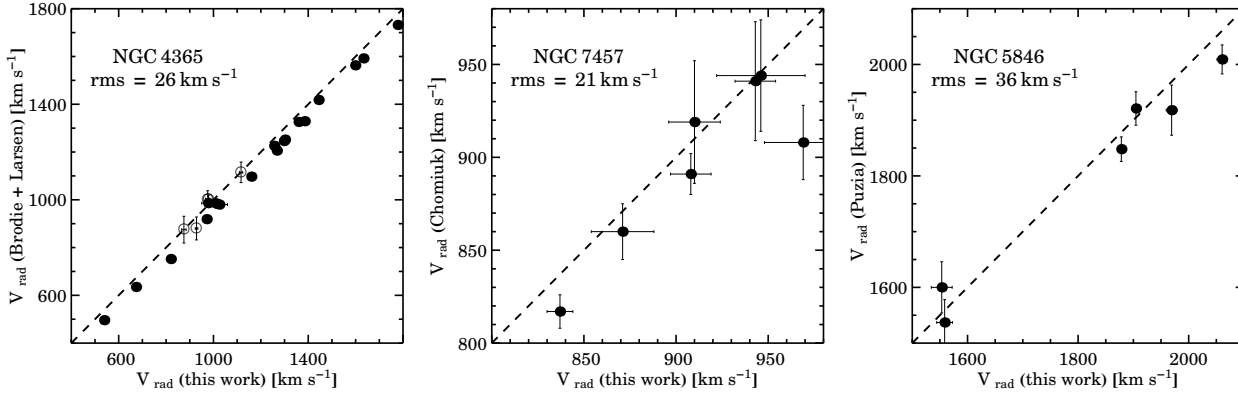


**Figure 8.** Comparison of our GC radial velocities with previous studies. For each galaxy the root-mean-square of the velocity difference between the two samples is also shown. Literature datasets come from Brodie et al. (2005) (black points) and Larsen et al. (2003) (open circles) for NGC 4365; Chomiuk et al. (2008) for NGC 7457; Puzia et al. (2004) for NGC 5846. The one-to-one line is shown as a dashed line.

## 4.2 Repeated GC measurements

We searched through the literature for GCs observed in our surveyed galaxies, finding existing datasets for three galaxies. In summary, we have re-observed: (i) 6 GCs of the 26 GCs confirmed by Puzia et al. (2004) in NGC 5846 using VLT/FORS2; (ii) 7 GCs of the 13 GCs found by Chomiuk et al. (2008) in NGC 7457 using Keck/LRIS; (iii) 24 GCs of the 33 GCs resulting from the combination of the Brodie et al. (2005) and Larsen et al. (2003) catalogues of NGC 4365, both observed with Keck/LRIS.

In Figure 8 we compare our DEIMOS dataset with literature studies. There is a rough agreement between external datasets and our DEIMOS radial velocities, although the root-mean-square of the velocity difference between the two datasets is larger than what was found with DEIMOS repeated measurements.

We supplement our GC catalogues with external GC radial velocities corrected for the mean offset between the literature and our DEIMOS measurements. This offset is  $-15 \text{ km s}^{-1}$  for both NGC 7457 and NGC 5846. In NGC 4365, the offset between DEIMOS radial velocities and Brodie et al. (2005) is effectively zero, and we only correct the dataset of Larsen et al. (2003) by  $-41 \text{ km s}^{-1}$ .

We test the reliability of our spectroscopic measurements by comparing the radial velocity of two or three GCs observed over different nights. Overall, we have collected 118 repeated GC radial velocities and these are shown in Figure 9. One-third of the total repeated sample is from a NGC 2768 mask that was observed twice with a one night offset. We find that repeated GC measurements are in good agreement in all the galaxies. The root-mean-square (rms) of the velocity difference between two observations is  $\delta V_{\text{rms}} = 15 \pm 1 \text{ km s}^{-1}$ .

## 4.3 Kinematic analysis

We study the kinematic properties of our GC systems using a maximum likelihood approach. We summarize here the main points of this analysis and refer to Foster et al. (2011) for the details. We divide the data in radial bins and then we fit the amplitude of the rotation ( $V_{\text{rot}}$ ), the velocity dispersion ( $\sigma$ ) and the kinematic position angle ( $PA_{\text{kin}}$ ) simultaneously. The bin size varies from galaxy to galaxy (wider for larger datasets) and it was set to have roughly the same number of objects per bin. For the  $j^{\text{th}}$  radial bin we minimise

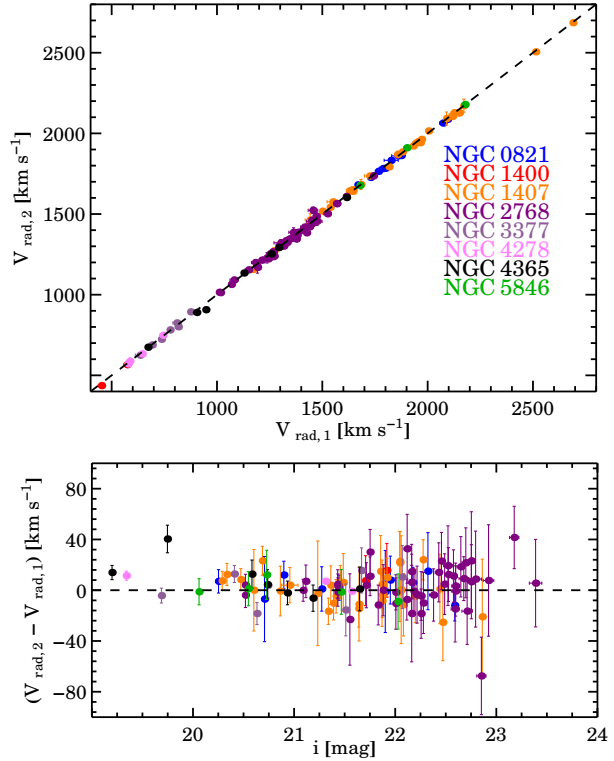


**Figure 9.** Repeated GC radial velocity measurements. In the *top panel* we show the radial velocity of a GC  $V_{\text{rad},1}$  against the radial velocity of the same GC observed in a different night  $V_{\text{rad},2}$ . Data points are colour coded according their host galaxy membership listed on the right. The dotted line is a one-to-one line. In the *bottom panel* we show the difference  $V_{\text{rad},2} - V_{\text{rad},1}$  as a function of the  $i$  band magnitude of the object. The dotted line shows the constant  $V_{\text{rad},2} - V_{\text{rad},1} = 0$  to guide the eye. Radial velocities from different nights are in good agreement with each other, with an overall root-mean-square (rms) of  $15 \pm 1 \text{ km s}^{-1}$ . No significant trend is seen as a function of GC magnitude.

the  $\chi^2$  function:

$$\chi_j^2 \propto \sum_{i=1}^{i=N_j} \left[ \frac{(V_{\text{rad},i} - V_{\text{mod},i,j})^2}{(\sigma_j^2 + (\Delta V_{\text{rad},i})^2)} + \ln(\sigma_j^2 + (\Delta V_{\text{rad},i})^2) \right], \quad (3)$$

where:

$$V_{\text{mod},i,j} = V_{\text{sys}} \pm \frac{V_{\text{rot},j}}{\sqrt{1 + \left(\frac{\tan(PA_i - PA_{\text{kin},j})}{q_{\text{kin},j}}\right)^2}}. \quad (4)$$

In eq. 4,  $PA_i$ ,  $V_{\text{obs},i}$  and  $\Delta V_{\text{obs},i}$  are the position angle, recession velocity and uncertainty on the recession velocity for the  $i^{\text{th}}$  GC, respectively. The axis ratio of GC systems is challenging to derive directly because of low number statistics, but it has been constrained in galaxies with large photometric datasets (Kissler-Patig et al. 1997, Strader et al. 2011, Blom et al. 2011). Therefore, the kinematic axis ratio  $q_{\text{kin}}$  of the GC system was assumed to be equal to the respective photometric axis ratio of the galaxy light (see Table 1). The galaxy systemic velocity  $V_{\text{sys}}$  was fixed to the values given in Table 1 because the GC mean velocity is in good agreement with the galaxy systemic velocity itself. Uncertainties on the fits to the GC kinematics are obtained using a bootstrapping method similar to that used by Côté et al. (2001). We obtain 1000 “mock” GC kinematic samples for each galaxy, by sampling with replacement from our measured distribution. Think kind of kinematic modelling tends to overestimate the rotation amplitude when the kinematic position angle is a free parameter. The correction for this bias is described in Appendix A.

By way of example, the best fit to eq. 4 for the GCs in NGC 3377 and its kinematic dataset are shown in Figure 10 and Table 5, respectively.

The kinematic method described above was used to investigate the kinematic properties of our surveyed galaxies in two different ways:

- First, the kinematic properties of each GC system were calculated as a function of the galactocentric radius. This approach allows us to compare the kinematics of a given GC system to different kinematic probes (e.g., long-slit spectroscopy and/or PNe kinematics). We generally use between 20 and 30 GCs per bin depending on the galaxy. These results are shown in Figure 11.
- Secondly, the confirmed GCs were sorted by their colour to study the GC kinematics as a function of colour. Here we use moving colour bins of equal width (with usually 20 GCs per bin) to investigate the effect of each GC on the final fit. This analysis is independent of the photometric dividing colour and it has the advantage of testing whether or not there is a transition in the kinematics between the two subpopulations. These results are shown in Figure 12.

To better appreciate the global kinematic properties of our GC systems, we also construct a 2D smoothed velocity field for our elongated early-type galaxies (i.e., galaxies with  $(b/a)_K < 0.6$ : NGC 821, NGC 2768, NGC 3377, NGC 7457). These galaxies are all part of the ATLAS<sup>3D</sup> sample (Krajnović et al. 2011) and are indeed good candidates to compare their moderate–fast stellar rotation in the innermost regions with the kinematics of their GC system. At every position  $(x, y)$  on the sky we compute the local radial velocity  $\hat{v}(x, y)$  via interpolation of the weighted average radial velocities of the  $N$  nearest neighbours, similar to the technique used in Coccato et al. (2009):

$$\hat{v}(x, y) = \frac{\sum_{i=1}^N V_{\text{rad},i}/d_i^2}{\sum_{i=1}^N 1/d_i^2} \quad (5)$$

with the weights being the reciprocal of the square distance  $d$  between two neighbour GCs. The 2D velocity field was smoothed using a Gaussian filter kernel of variable width for each galaxy on a regularly spaced grid. The kernel size was arbitrarily set between 2 and 5 kpc depending the sampling of the GC system and

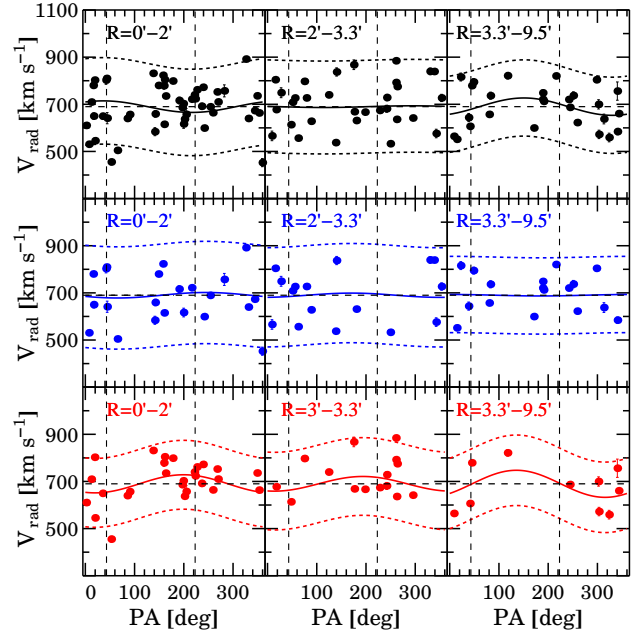


**Figure 10.** Rotation of NGC 3377 GC system with position angle in different radial bins. From the top to the bottom, panels show the rotation for all, blue and red GC subpopulations respectively. Whereas from the left to the right, panels show the rotation in the radial bin reported on the top left for each panel. The photometric major axis and the systemic velocity of the galaxy are both from Table 1 and represented with dashed vertical and dashed horizontal lines respectively. The best fit to eq. 4 and  $\pm 2\sigma$  envelope are shown as filled and dotted lines respectively.

on the size of the galaxy. For the sake of comparison, we analysed the SAURON data-cubes (Emsellem et al. 2007) of the same four early-type ellipticals in order to reproduce their 2D stellar velocity fields using our technique. These results are shown in Figure 13.

We also compute the root-mean-square velocity:

$$V_{\text{rms}}^2 = \frac{1}{N} \sum_{i=1}^N (V_{\text{rad},i} - V_{\text{sys}})^2 - (\Delta V_{\text{rad},i})^2. \quad (6)$$

This quantity coincides with the velocity dispersion in eq. 4 if the contribution of the rotation is negligible. The uncertainty on the  $V_{\text{rms}}$  is estimated with the formulae provided by Danese et al. (1980).

## 5 NOTES ON INDIVIDUAL GALAXIES

In this section we briefly discuss the kinematic results for our new nine GC systems that are presented in Figure 11, Figure 12 and Figure 13.

### 5.1 NGC 821

NGC 821 is an isolated E6 galaxy (de Vaucouleurs 1991) with photometric and kinematic signatures of an edge-on stellar disk (Emsellem et al. 2007; Proctor et al. 2009). The dark matter content of this galaxy has been debated in the literature. Romanowsky et al. (2003), and recently Teodorescu et al. (2010) found that the velocity dispersion of the PNe decreases with radius. In contrast, Weijmans et al. (2009), Forestell & Gebhardt (2010)

ID	RA	Dec	$V_{\text{rad}}$	$\delta V_{\text{rad}}$	$g$	$\delta g$	$r$	$\delta r$	$i$	$\delta i$
(1)	[Degree]	[Degree]	[ $\text{km s}^{-1}$ ]	[ $\text{km s}^{-1}$ ]	[mag]	[mag]	[mag]	[mag]	[mag]	[mag]
NGC3377_GC1	161.94713	14.00741	810	8	21.387	0.019	20.855	0.013	20.606	0.014
NGC3377_GC2	161.90719	13.96616	724	10	22.295	0.032	21.588	0.021	21.223	0.021
NGC3377_GC3	161.89561	13.97022	729	13	22.596	0.032	21.962	0.021	21.671	0.021
NGC3377_GC4	161.92600	14.01391	453	17	22.610	0.034	22.048	0.023	21.864	0.025
NGC3377_GC5	161.89744	13.97086	681	14	22.789	0.037	22.037	0.023	21.691	0.022
NGC3377_GC6	161.93466	13.96388	779	15	22.546	0.034	21.948	0.023	21.653	0.025
NGC3377_GC7	161.91688	13.96030	617	18	22.919	0.046	22.286	0.031	22.073	0.036
NGC3377_GC8	161.88981	13.95709	754	5	20.002	0.009	19.411	0.006	19.116	0.005
NGC3377_GC9	161.94103	14.03665	804	6	20.150	0.009	19.632	0.006	19.378	0.006
NGC3377_GC10	161.87097	13.91145	820	7	20.895	0.013	20.305	0.008	20.094	0.008
...	...	...	...	...	...	...	...	...	...	...
NGC3377_star1	162.03633	14.02335	185	11	22.174	0.026	21.750	0.017	21.581	0.017
NGC3377_star2	161.86723	13.90198	289	18	22.547	0.003	20.090	0.020	21.887	0.002
...	...	...	...	...	...	...	...	...	...	...
NGC3377_gal1	161.83237	13.92902	—	—	22.250	0.025	21.595	0.015	21.370	0.015
NGC3377_gal2	161.95037	14.08945	—	—	24.188	0.069	24.214	0.062	24.290	0.087
...	...	...	...	...	...	...	...	...	...	...

**Table 5.** Spectro-photometric catalogue of objects around NGC 3377. The horizontal line divides the sample into spectroscopically confirmed GCs, spectroscopically confirmed Galactic stars and background galaxies. The first column gives the object ID, composed of the galaxy name and the object identification. Columns 2 and 3 give position in right ascension and declination (J2000), respectively. Columns 4 and 5 are the observed heliocentric radial velocities and uncertainties respectively. The remaining columns are the Subaru photometry in  $gri$  and respective uncertainties. The full table for all the surveyed galaxies is available in the online version.

and Proctor et al. (2009) found a flat velocity dispersion for the stellar component within 100 arcsec. A photometric study of the GC system of NGC 821 was carried out by Spitler et al. (2008) using wide-field WIYN and *HST* observations. They were able to detect significant colour bimodality only after combining ground-based and space-based observations.

Our Subaru observations suffer from moderate  $g$  band seeing ( $\sim 1.2$  arcsec). However, we detect significant GC colour bimodality, although the blue and the red peaks are not clearly visible. We confirm that the surface density profile of the GC system extends up to 4 arcmin, as suggested from the WIYN imaging.

The combination of the poor  $g$  band seeing, and the presence of the 10th magnitude star 2 arcmin from the galaxy centre, resulted in a low return rate of spectroscopically confirmed GCs. In total, we obtained radial velocities for 61 GCs over 6 DEIMOS masks. We adopt a colour split at  $(g-i) = 1.0$ . This value was used to analyse the kinematics of blue and red GC subpopulations separately.

We detect significant rotation only for the blue GCs and for a small group of red GCs. The blue GCs are found to rotate at  $\sim 85 \text{ km s}^{-1}$  along  $\text{PA}_{\text{kin}} = 85^{+26}_{-27}$  deg, consistent with the photometric minor axis and in agreement with that found by Coccato et al. (2009) using PNe. Such a peculiarity is clearly visible in Figure 12. We will discuss this feature and its implications in more detail later. Interestingly, we note that the direction of the GC and PNe rotation coincides with an elongated jet/outflow structure detected in the X-ray (Pellegrini et al. 2007). With the adopted colour split, the kinematic position angle of the red GCs is generally unconstrained, except the outer red GCs that counter rotate with respect to the host galaxy stars. The velocity dispersion of both the red and the blue GCs declines with radius with a slope similar to that of the PNe and host galaxy stars.

## 5.2 NGC 1400

NGC 1400 has been classified both as a face-on S0 (Jarrett et al. 2003) and as an E0 (e.g., da Costa et al. 1998). It is the second brightest galaxy in the Eridanus group after NGC 1407. We have assumed that NGC 1407 and NGC 1400 lie at the same distance of 26.8 Mpc. NGC 1400 is characterised by a uniformly old stellar age up to  $\sim 1.3R_{\text{eff}}$  (Spolaor et al. 2008) and by an unusually low systemic velocity ( $V_{\text{sys}} = 558 \text{ km s}^{-1}$ ) for its distance. Forbes et al. (2006) studied the GC system of this galaxy using Keck/LRIS in imaging mode, detecting significant bimodality.

The photometric GC selection was performed within 8 arcmin from the galaxy centre to minimise the contamination from NGC 1407 GC system, resulting in a clear bimodal distribution, with the colour separation occurring at  $(g-i) = 0.98$ . The GC surface density was corrected for the local NGC 1407 contribution. This galaxy shows the steepest red surface density profile among our galaxies, similar to the slope of the galaxy surface brightness. In contrast, the profile of the blue GC subpopulation is more radially extended and also requires a power-law fit, because a Sèrsic function does not return a satisfactory solution.

We present here radial velocities for 34 blue and 37 red GCs respectively, for a total of 71 spectroscopically confirmed GCs. Despite their small angular separation ( $\sim 10$  arcmin), NGC 1407 and NGC 1400 also have a large peculiar velocity difference ( $\sim 1200 \text{ km s}^{-1}$ ), assuring a reliable separation of their spectroscopically confirmed GCs. The red GCs mimic the rotation of the stars in the inner regions, whereas the rotation of the blue GCs is consistent with zero with a marginal signature of counter-rotation in the inner radial bin. The velocity dispersion of the red GCs is in agreement with long-slit data in the region of overlap, with a slightly increasing trend towards the outer regions. Conversely, the velocity dispersion of the blue GCs decreased with the radius.

Galaxy ID	$V_{\text{sys,GC}}$ [km s <sup>-1</sup> ]	$V_{\text{rms,A}}$ [km s <sup>-1</sup> ]	$V_{\text{rms,B}}$ [km s <sup>-1</sup> ]	$V_{\text{rms,R}}$ [km s <sup>-1</sup> ]	$(V_{\text{rot}}/\sigma)_A$	$(V_{\text{rot}}/\sigma)_B$	$(V_{\text{rot}}/\sigma)_R$	$\text{PA}_{\text{kin,A}}$ [deg]	$\text{PA}_{\text{kin,B}}$ [deg]	$\text{PA}_{\text{kin,R}}$ [deg]
(1)	(2)	(3)	(4)	(5)	(6)	(7)	(8)	(9)	(10)	(11)
NGC 821	1750	158 <sup>+17</sup> <sub>-13</sub>	145 <sup>+28</sup> <sub>-18</sub>	154 <sup>+26</sup> <sub>-17</sub>	0.11 <sup>+0.18</sup> <sub>-0.18</sub>	0.60 <sup>+0.33</sup> <sub>-0.30</sub>	0.09 <sup>+0.27</sup> <sub>-0.22</sub>	80 <sup>+183</sup> <sub>-90</sub>	85 <sup>+26</sup> <sub>-27</sub>	252 <sup>+94</sup> <sub>-137</sub>
NGC 1400	612	137 <sup>+14</sup> <sub>-11</sub>	140 <sup>+22</sup> <sub>-15</sub>	135 <sup>+19</sup> <sub>-14</sub>	0.07 <sup>+0.17</sup> <sub>-0.13</sub>	0.10 <sup>+0.25</sup> <sub>-0.15</sub>	0.54 <sup>+0.27</sup> <sub>-0.26</sub>	39 <sup>+49</sup> <sub>-48</sub>	200 <sup>+55</sup> <sub>-60</sub>	30 <sup>+21</sup> <sub>-20</sub>
NGC 1407	1774	224 <sup>+9</sup> <sub>-8</sub>	232 <sup>+14</sup> <sub>-12</sub>	216 <sup>+11</sup> <sub>-11</sub>	0.17 <sup>+0.07</sup> <sub>-0.08</sub>	0.03 <sup>+0.10</sup> <sub>-0.10</sub>	0.32 <sup>+0.10</sup> <sub>-0.10</sub>	285 <sup>+30</sup> <sub>-29</sub>	224 <sup>+120</sup> <sub>-101</sub>	299 <sup>+18</sup> <sub>-19</sub>
NGC 2768	1338	165 <sup>+13</sup> <sub>-11</sub>	173 <sup>+23</sup> <sub>-17</sub>	160 <sup>+17</sup> <sub>-13</sub>	0.39 <sup>+0.13</sup> <sub>-0.11</sub>	0.34 <sup>+0.21</sup> <sub>-0.23</sub>	0.43 <sup>+0.15</sup> <sub>-0.14</sub>	97 <sup>+22</sup> <sub>-24</sub>	121 <sup>+32</sup> <sub>-34</sub>	79 <sup>+28</sup> <sub>-27</sub>
NGC 3377	685	100 <sup>+7</sup> <sub>-6</sub>	100 <sup>+12</sup> <sub>-9</sub>	85 <sup>+10</sup> <sub>-7</sub>	0.19 <sup>+0.13</sup> <sub>-0.14</sub>	0.09 <sup>+0.15</sup> <sub>-0.14</sub>	0.58 <sup>+0.20</sup> <sub>-0.20</sub>	197 <sup>+40</sup> <sub>-40</sub>	275 <sup>+77</sup> <sub>-108</sub>	181 <sup>+21</sup> <sub>-19</sub>
NGC 4278	637	177 <sup>+9</sup> <sub>-7</sub>	182 <sup>+12</sup> <sub>-10</sub>	152 <sup>+12</sup> <sub>-10</sub>	0.17 <sup>+0.08</sup> <sub>-0.08</sub>	0.16 <sup>+0.11</sup> <sub>-0.13</sub>	0.25 <sup>+0.15</sup> <sub>-0.14</sub>	200 <sup>+26</sup> <sub>-26</sub>	194 <sup>+32</sup> <sub>-38</sub>	207 <sup>+39</sup> <sub>-42</sub>
NGC 4365	1210	248 <sup>+12</sup> <sub>-10</sub>	230 <sup>+20</sup> <sub>-16</sub>	258 <sup>+16</sup> <sub>-13</sub>	0.11 <sup>+0.09</sup> <sub>-0.10</sub>	0.17 <sup>+0.18</sup> <sub>-0.14</sub>	0.26 <sup>+0.11</sup> <sub>-0.12</sub>	129 <sup>+37</sup> <sub>-42</sub>	307 <sup>+29</sup> <sub>-40</sub>	121 <sup>+26</sup> <sub>-26</sub>
NGC 5846	1706	238 <sup>+13</sup> <sub>-11</sub>	266 <sup>+22</sup> <sub>-18</sub>	207 <sup>+17</sup> <sub>-14</sub>	0.02 <sup>+0.15</sup> <sub>-0.12</sub>	0.19 <sup>+0.14</sup> <sub>-0.10</sub>	0.12 <sup>+0.14</sup> <sub>-0.15</sub>	157 <sup>+60</sup> <sub>-79</sub>	259 <sup>+60</sup> <sub>-71</sub>	107 <sup>+43</sup> <sub>-56</sub>
NGC 7457	847	68 <sup>+12</sup> <sub>-9</sub>	—	—	1.68 <sup>+0.37</sup> <sub>-0.40</sub>	—	—	324 <sup>+10</sup> <sub>-10</sub>	—	—
NGC 3115	710	164 <sup>+9</sup> <sub>-8</sub>	166 <sup>+13</sup> <sub>-11</sub>	161 <sup>+13</sup> <sub>-10</sub>	0.66 <sup>+0.09</sup> <sub>-0.09</sub>	0.74 <sup>+0.12</sup> <sub>-0.13</sub>	0.61 <sup>+0.14</sup> <sub>-0.13</sub>	35 <sup>+11</sup> <sub>-12</sub>	47 <sup>+13</sup> <sub>-13</sub>	20 <sup>+16</sup> <sub>-17</sub>
NGC 4486	1336	328 <sup>+14</sup> <sub>-12</sub>	296 <sup>+28</sup> <sub>-22</sub>	337 <sup>+16</sup> <sub>-14</sub>	0.07 <sup>+0.05</sup> <sub>-0.04</sub>	0.09 <sup>+0.07</sup> <sub>-0.08</sub>	0.29 <sup>+0.17</sup> <sub>-0.17</sub>	105 <sup>+40</sup> <sub>-38</sub>	92 <sup>+49</sup> <sub>-48</sub>	123 <sup>+39</sup> <sub>-43</sub>
NGC 4494	1338	99 <sup>+14</sup> <sub>-12</sub>	98 <sup>+9</sup> <sub>-7</sub>	99 <sup>+15</sup> <sub>-11</sub>	0.60 <sup>+0.12</sup> <sub>-0.11</sub>	0.65 <sup>+0.15</sup> <sub>-0.15</sub>	0.43 <sup>+0.21</sup> <sub>-0.23</sub>	174 <sup>+16</sup> <sub>-17</sub>	167 <sup>+16</sup> <sub>-11</sub>	195 <sup>+33</sup> <sub>-31</sub>

**Table 6.** GC kinematic results for our galaxy sample. Column (2) shows the systemic velocity of the host galaxy obtained from the weighted average of the GC radial velocities of the azimuthal-complete innermost region. The remaining columns are the overall root-mean-square velocity  $V_{\text{rms}}$ , the rotational dominance parameter  $(V_{\text{rot}}/\sigma)$  and kinematic position angle PA for all, blue and red GC subpopulations respectively.

### 5.3 NGC 1407

NGC 1407 is a massive E0 galaxy at the centre of the dwarf galaxy dominated Eridanus A group (Brough et al. 2006). It shows moderate rotation along the photometric major axis and has a weak central AGN (Zhang et al. 2007). The stellar population analysis of Spolaor et al. (2008) found the galaxy to possess a uniformly old age within  $\sim 0.6R_{\text{eff}}$ . A dynamical analysis of NGC 1407 was given by Romanowsky et al. (2009). They used Suprime-Cam imaging and DEIMOS spectra for 172 GCs and found a massive dark halo.

In this work, we use the photometric results presented in Romanowsky et al. (2009) in which the Suprime-Cam imaging was reduced and analysed with the same methodology described in this paper. The colour distribution shows clear bimodality with the colour separation occurring at  $(g - i) = 0.98$ . We supplement the spectroscopic sample of Romanowsky et al. (2009) with 6 additional DEIMOS masks, that make NGC 1407, with a total of 369 spectroscopically confirmed GCs, the most populous spectro-photometric dataset in our galaxy sample.

We detect rotation along the photometric major axis for both GC subpopulations. The blue GCs rotate in the innermost radial bin along the photometric minor axis and between 3 and 5  $R_{\text{eff}}$  along the photometric major axis. Similarly, the rotation of the red GCs occurs along the photometric major axis directions, but in this case the rotation signal is generally larger and better constrained than that of the blue GCs. Both GC subpopulations appear to rotate in the outermost regions of the galaxy along the major axis of the galaxy. The velocity dispersion of the red GC subpopulation in the inner regions is consistent with stellar data from Spolaor et al. (2008) and Proctor et al. (2009) showing a decreasing profile up to 10  $R_{\text{eff}}$ . Conversely, the velocity dispersion of the blue GCs increases with radius.

### 5.4 NGC 2768

NGC 2768 is classified as E6 in de Vaucouleurs (1991) and as S0<sub>1/2</sub> in Sandage & Bedke (1994). Spectroscopic studies of the very central regions (McDermid et al. 2006) have also suggested a young (2.5 Gyr) stellar population associated with the disk, as sup-

ported by the recent supernova SN2000ds (Filippenko & Chornock 2000). Kundu & Whitmore (2001) studied the *HST*/WFPC2 photometry for 113 GC candidates in this galaxy, finding a statistically significant probability of it having a bimodal colour distribution.

In this work, NGC 2768 was imaged with *R<sub>C</sub>iz* filters, in good seeing conditions but with the lowest exposure time among our sample of galaxies. Using KMM we found the colour distribution to be bimodal, with the blue and red peaks at  $(R_C - z) = 0.41 \pm 0.01$  and  $0.70 \pm 0.02$  respectively. Bimodality was also found in the *HST*/ACS West pointing used to design the DEIMOS masks in the central region. The colour peaks occur at  $(F435W - F814W) = 1.77 \pm 0.03$  and  $2.17 \pm 0.01$  respectively.

We find 109 spectroscopically confirmed GCs over 5 DEIMOS masks observed in sub-arcsec seeing conditions. Using a colour split at  $(R_C - z) = 0.57$  and excluding the marginal GCs, we investigate the kinematics of the resulting 60 blue and 42 red GCs respectively.

We find significant rotation only for the red GCs, which rotate roughly along the photometric major axis in agreement with the host galaxy stars. The 2-D velocity field of the red GCs is akin to that of ATLAS<sup>3D</sup> in the inner regions (Figure 13). The blue GCs have a marginally higher velocity dispersion profile than the red GCs.

### 5.5 NGC 3377

NGC 3377 is a classical E6 elliptical in the Leo I group and the closest galaxy in our sample. The resolved stellar properties of NGC 3377 have been studied by (Harris et al. 2007) that found no evidence for any young ( $< 3$  Gyr) stellar population. Coccato et al. (2009) studied 159 PNe in this galaxy, detecting significant rotation within 2 arcmin and a kinematic major axis twist of  $\sim 80$  deg from the major towards the minor axis. Kundu & Whitmore (2001), Chies-Santos et al. (2011) and Cho et al. (2012) studied the GC system of this galaxy using *HST* imaging, finding the colour distribution to be likely bimodal.

NGC 3377 was imaged with *gri* filters and *gz* filters for ground based and space based observations respectively. We found a high probability for the colour distribution to be bimodal, both in

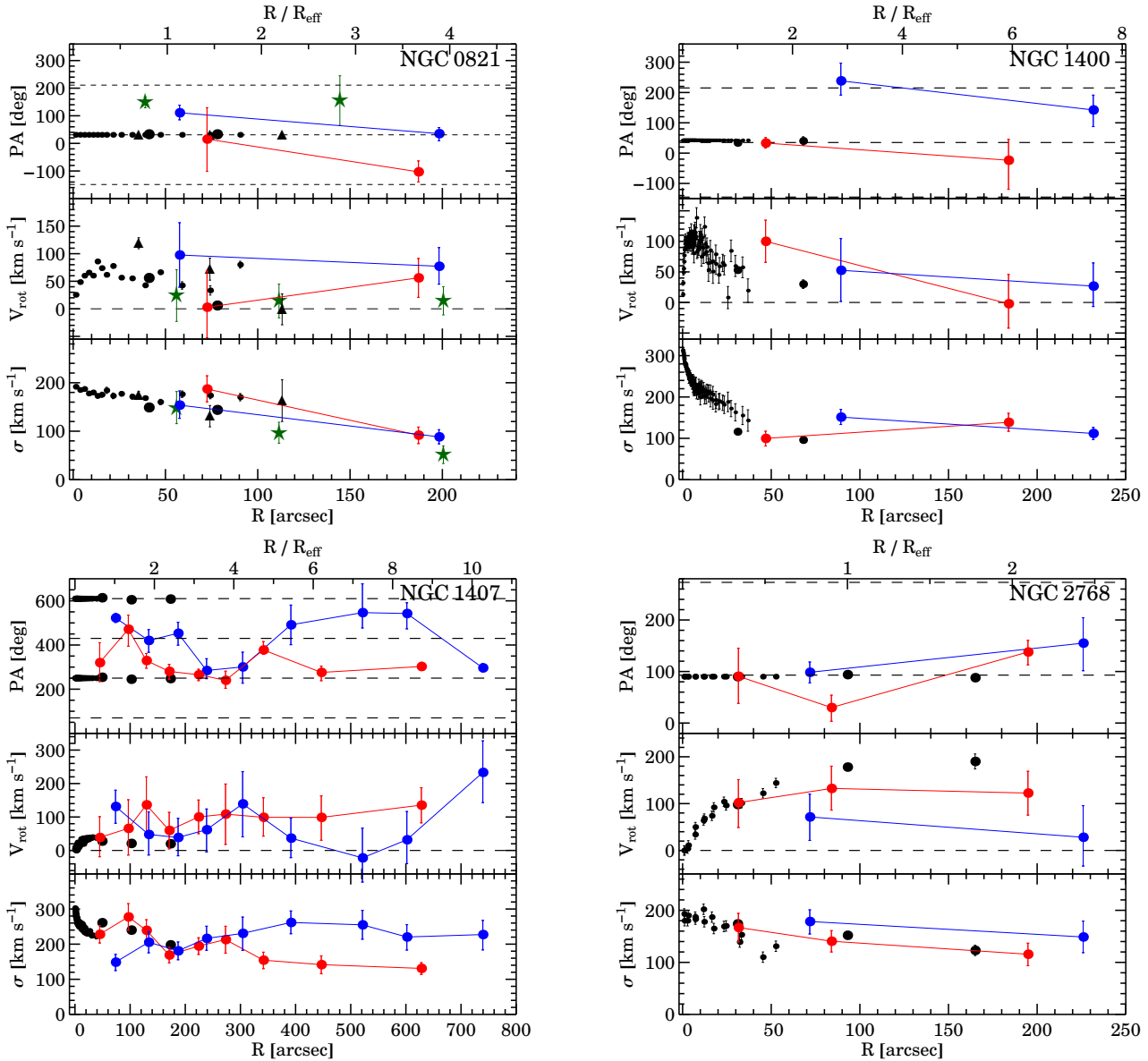


**Figure 11.** GC system kinematics compared to stellar data. For each galaxy (labeled on the top right of each panel) the plots represent the term of parameters ( $PA_{\text{kin}}, V_{\text{rot}}, \sigma$ ) that minimise eq. 3 as a function of the radius. Data points are joined for clarity, with the error bars representing the 68 per cent confidence intervals. The dashed horizontal lines in top and middle panels represent the photometric  $PA \pm 180$  deg from Table 1 and  $V_{\text{rot}} = 0$ , respectively. All the PNe data (green stars) are from Coccato et al. (2009). Integrated stellar light data are shown as small black points (if from long-slit) and large black points (if from Proctor et al. 2009). References for long-slit data are: Forestell & Gebhardt (2010) for NGC 821; Proctor et al. (2009) for NGC 1400 and NGC 1407; Fried & Illingworth (1994) for NGC 2768; Coccato et al. (2009) for NGC 3377; van der Marel & Franx (1993) for NGC 4278; Bender et al. (1994) for NGC 4365; Kronawitter et al. (2000) for NGC 5846; Simien & Prugniel (2000) for NGC 7457. Black triangles in NGC 821 are SAURON-IFU data from Weijmans et al. (2009). For NGC 7457, because of the low number statistics, we only show the total GC kinematic profile in black.

our Suprime-Cam and in the supplementary ACS archive imaging, as already found in Chies-Santos et al. (2011).

In this work, we present radial velocities for 126 GCs, observed in 4 DEIMOS masks. It is worth noting that we extend the kinematics of this galaxy to  $8 R_{\text{eff}} \sim 25$  kpc, two times further than the PNe studies. We rule out two GCs that are likely to belong to the spiral galaxy NGC 3377A ( $V_{\text{sys}} \sim 573$  km s $^{-1}$ ) that lies  $\sim 8$  arcmin North-West from NGC 3377. With a colour split at  $(g - i) = 0.88$  we study the kinematics of 57 blue and 60 red GCs, respectively.

We detect significant rotation for the red GC subpopulation

along the photometric major axis in agreement with PNe and long-slit data (Coccato et al. 2009). As found for the PNe, we discover that the kinematic position angle of the red GC subpopulation twists with radius from 250 deg to 150 deg (see also Figure 10). The 2-D velocity field of the red GCs is consistent with ATLAS $^{3D}$  in the inner regions (Figure 13). The position angle of the blue GC subpopulation is unconstrained, implying an overall null rotation with radius. The velocity dispersion of the red GC subpopulation is very flat and it matches the stellar and the PNe. The blue GCs have an overall higher velocity dispersion profile than the red GC subpopulation.

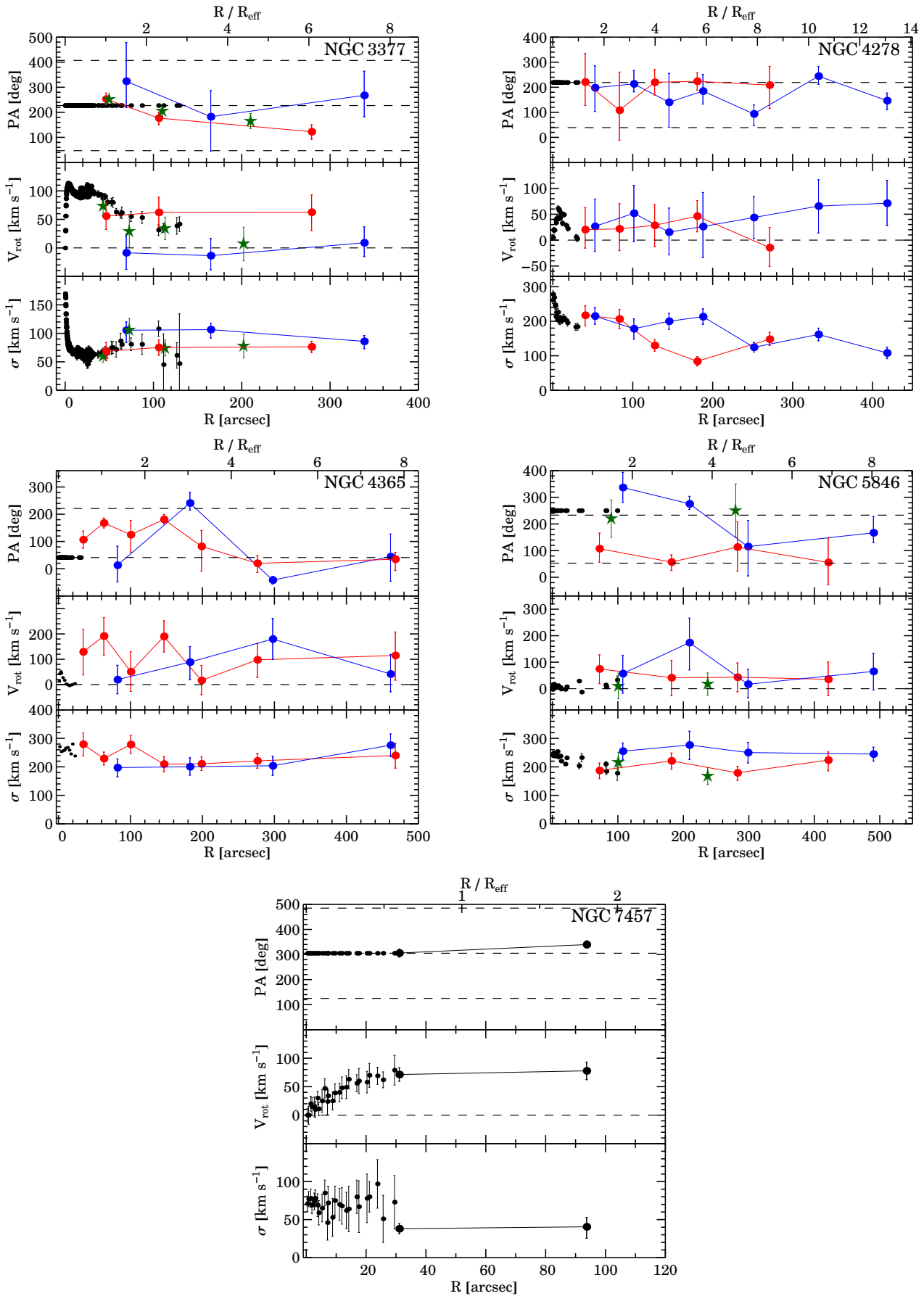
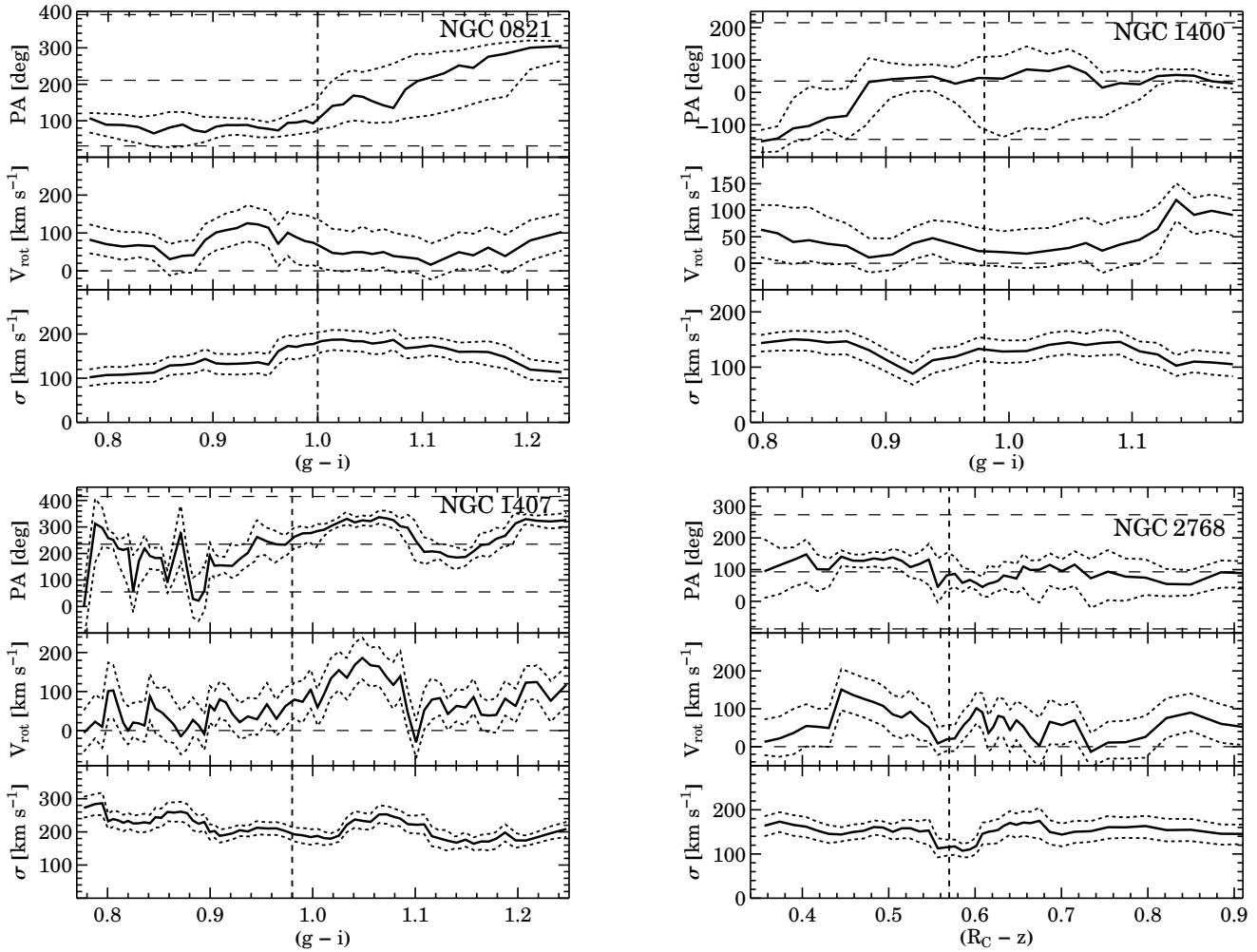


Figure 11 – continued





**Figure 12.** GC kinematics as a function of colour. Kinematic position angle, rotation velocity and velocity dispersion are shown in the top, central and bottom panel respectively. Dotted lines represent 68 per cent confidence intervals. Also shown are the photometric major axis (horizontal dotted lines) from Table 1 and the colour split between blue and red GC subpopulations (vertical dashed line) as derived from the KMM analysis.

## 5.6 NGC 4278

NGC 4278 is an elliptical (E1–2) member of the Coma I cloud. It has been extensively studied at different wavelengths: in radio, Nagar et al. (2005) detected two sub-parsec jets; in X-rays, a long (months) time scale variability (Ho et al. 2001) and a dominant nuclear source (Younes et al. 2010) were detected. It has long been known for its massive ( $\sim 10^8 M_{\odot}$ ) HI disc extending beyond  $10 R_{\text{eff}}$  (Gallagher et al. 1977) and used to infer the dark matter content at large radii (Bertola et al. 1993). The bimodality of the GC system of NGC 4278 has been under debate. Both Forbes et al. (1996) and Kundu & Whitmore (2001) investigated the GC system of NGC 4278 with *HST*/WFPC2, finding a marginal or “likely” probability for the  $(V - I)$  distribution to be bimodal. Recently, Chies-Santos et al. (2011) combined *HST*/ACS and WHT/LRIS imaging, finding evidence for bimodality in space-based but not ground-based datasets.

In this work we present new wide field *BVI* Suprime-Cam imaging (with the *B* band in poor seeing conditions), combined with four *g* and *z* *HST*/ACS pointings downloaded from the Hubble Legacy Archive (see Section 3.2). We find statistically significant bimodality both in our ground-based and space-based obser-

vations, with the colour separation occurring at  $(B - I) \sim 1.9$  and  $(g - z) = 1.1$ , respectively.

We spectroscopically confirm 256 GCs over four DEIMOS masks observed in good seeing conditions. Given the wide field coverage of the four *HST* pointings, we decided to use *HST* magnitudes to divide the kinematics of blue and red GC subpopulations, converting  $(V - I)$  colours into  $(g - z)$  if only Subaru photometry was available. As for other group members, we exclude from the kinematics analysis GCs that might be associated with other galaxies. We select and remove three GCs whose position and radial velocity are consistent with the galaxy NGC 4283 ( $V_{\text{sys}} = 984 \text{ km s}^{-1}$ ) that lies 3.6 ( $\sim 15 \text{ kpc}$ ) arcmin from NGC 4278.

We find no clear evidence for red GC rotation, but there is a hint that the blue GCs rotate in the outer regions along a direction intermediate between the major and the minor axis. The velocity dispersion of the red and blue GCs seem to be in good agreement with long-slit data in the inner regions although there is no direct overlap between the two datasets. The blue GCs have an overall higher velocity dispersion at intermediate radii.

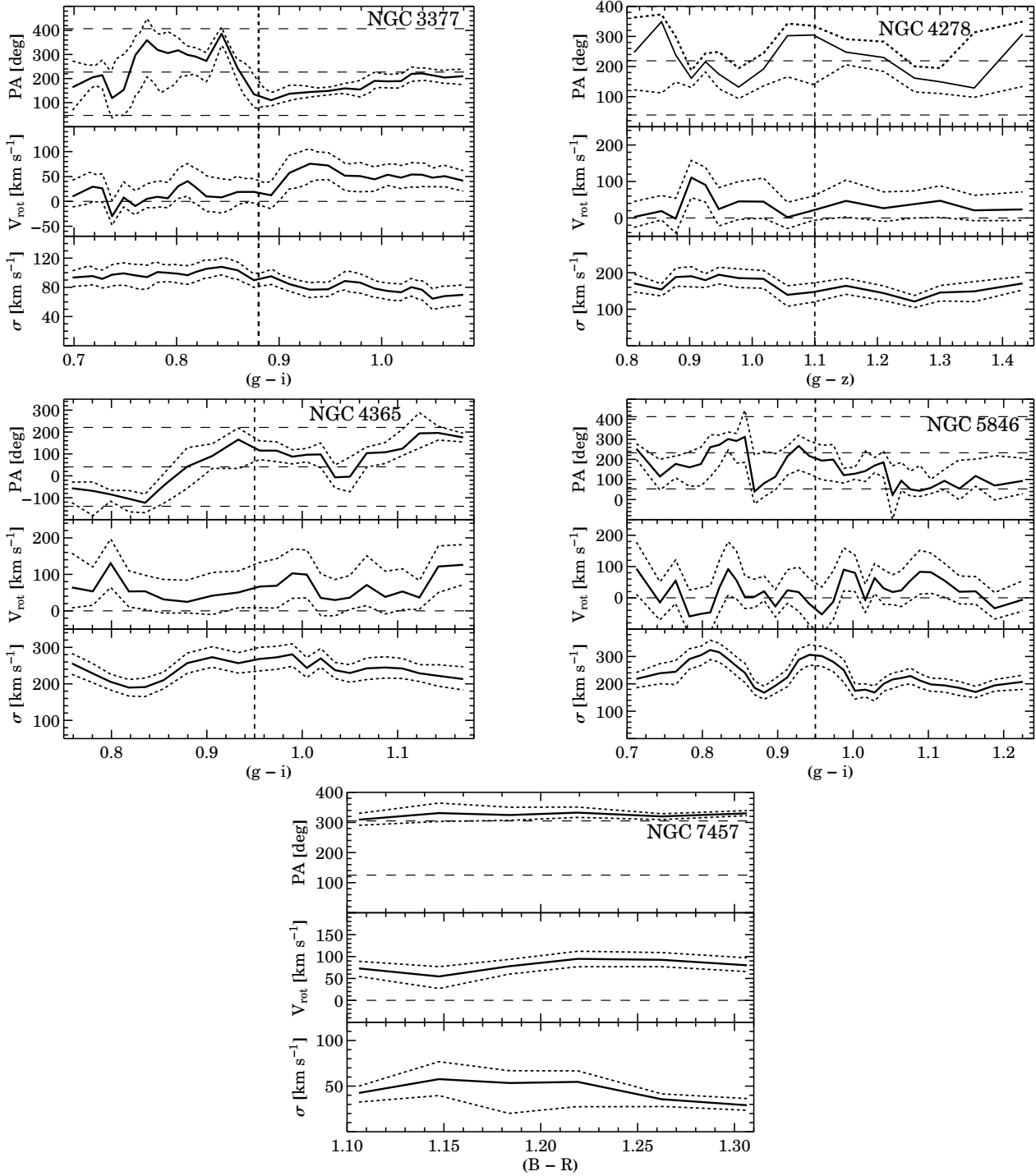
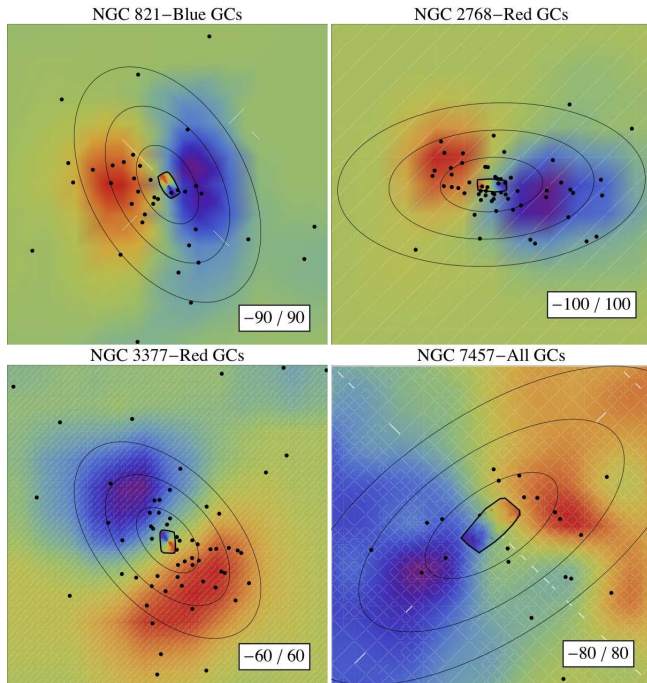


Figure 12 – continued

### 5.7 NGC 4365

NGC 4365 is a massive elliptical (E3) behind the Virgo cluster with signs of an ongoing merger (Mihos et al. 2012, in preparation). It has a kinematically distinct core (Krajnović et al. 2011) and an unusual stellar rotation along the photometric minor axis (Bender et al. 1994). Its GC system is mainly known for an odd GC colour distribution that seems to suggest the presence of three, instead of the classic two, subpopulations (Larsen et al. 2003, 2005; Brodie et al. 2005; Blom et al. 2011).

We make use of the photometric results presented in Blom et al. (2011) based on  $gz$  *HST/ACS* and  $gri$  Suprime-Cam imaging. In this work, we will treat the GC system of NGC 4365 as made up of two classic subpopulations and we refer to Blom et al. (2012, in preparation) for a detailed study of the kinematics of the three subpopulations. We use a colour split at  $(g-i) \sim 0.91$  that includes the “green” GCs as part of the red subpopulation. We represent here the surface density profile published in Blom et al. (2011) that shows that red GCs is more centrally concentrated than



**Figure 13.** Two-dimensional smoothed velocity fields of our diskly early-type galaxies. Black points and ellipses represent the locations of the spectroscopically confirmed GCs for a given population and the 2, 4, 6  $R_{\text{eff}}$  isophotes corrected for the galaxy ellipticity respectively. The white boxes are the maximum red-shifted and minimum blue-shifted velocities in the galaxy rest frame in unit of  $\text{km s}^{-1}$ . The SAURON stellar velocity maps are also shown in the innermost region of the galaxies. The agreement between the two datasets (except for NGC 821) is extremely good.

the blue GC subpopulation, with a trend similar to that of the galaxy stellar light (Figure 6).

We spectroscopically confirm 269 GCs over 6 DEIMOS masks. We study the kinematics of 87 blue and 164 red GCs respectively. We also add 9 GCs from the combined dataset of Larsen et al. (2003) and Brodie et al. (2005) as described in §4.2. We find that the red GCs rotate within  $R < 200$  arcsec along the photometric minor axis, mimicking the kinematics of the stars. The rotation of the blue GCs is only significant at intermediate radii. The velocity dispersion profile is identical for the blue and the red GCs.

### 5.8 NGC 5846

NGC 5846 is the brightest member of a galaxy group. The dynamics of NGC 5846 has been modelled within  $1R_{\text{eff}}$  (Cappellari et al. 2007; Kronawitter et al. 2000). Recently, Das et al. (2008) derived the mass of this galaxy up to  $11R_{\text{eff}}$  exploiting X-ray and PNe observations. An *HST*/WFPC2 analysis of the NGC 5846 GC system was given in Forbes et al. (1997) and then revisited by Chies-Santos et al. (2006). In addition to the classic bimodality, they also discovered that the GC system is better aligned with the galaxy’s minor axis than its major axis and that this galaxy has an unusually low specific frequency compared to similar dominant ellipticals in groups or clusters.

In this work we present new Subaru photometry in *gri* filters, with the *g* band in moderate seeing conditions ( $\sim 1$  arcsec). Although the red peak is not clearly visible (Figure 5), KMM re-

turned a high probability for the colour distribution to be bimodal with a colour split at  $(g - i) = 0.95$ .

We spectroscopically confirm 195 GCs over 6 DEIMOS masks. We also note that some radial velocities might be associated with other bright members of the group as NGC 5846A ( $V_{\text{sys}} = 2200 \text{ km s}^{-1}$ ) and NGC 5845 ( $V_{\text{sys}} = 1450 \text{ km s}^{-1}$ ). However the similar systemic velocities of these galaxies with NGC 5846 ( $V_{\text{sys}} = 1712 \text{ km s}^{-1}$ ) makes any attempt to distinguish their GC populations problematic. We also supplement our DEIMOS catalogue with 22 GCs from the dataset of Puzia et al. (2004) as described in §4.2. In summary, we study the kinematics of 104 blue and 108 red GCs.

We detect rotation only for the blue GCs, which rotate between 150 and 300 arcsec close to photometric major axis. This feature might be caused by the GCs of NGC 5846A, which contaminates our sample within 300 arcsec. The velocity dispersion of the red GCs is flat with radius and consistent with other studies, although the PNe seem to suggest a slightly decreasing slope. The blue GCs have a systematically higher velocity dispersion than the red GC subpopulation.

### 5.9 NGC 7457

NGC 7457 is an isolated S0 with a pseudo-bulge detected both photometrically (Tomita et al. 2000) and kinematically (Pinkney et al. 2003) that shows an unusually low central velocity dispersion for its luminosity. Emsellem et al. (2007) revealed that this galaxy has a small counter rotating core that might be the result of a merger. Chomiuk et al. (2008) gave an overview of the GC system of NGC 7457 using *HST* observations and Keck/LRIS spectra for 13 GCs. They find evidence for a third intermediate population of GCs sharing the same age (2–2.5 Gyr) as the young nuclear (radius of 1.5 arcsec) stellar population discovered by Sil’chenko et al. (2002).

NGC 7457 is the only galaxy in our sample not observed with Suprime-Cam. We have instead used the photometric results of Hargis et al. (2011) to design our DEIMOS masks, and we refer to their paper for a detailed description of the data reduction and analysis. They provide wide field WIYN/Minimosaic photometry of the GC system of this galaxy, finding that the colour distribution is not bimodal and showing the total population to be made up of  $210 \pm 30$  GCs with a radial extent of  $12 \pm 2$  kpc.

We find 21 spectroscopically confirmed GCs in two DEIMOS masks observed in average 0.9 arcsec seeing conditions. We also obtained spectra for 7 of the 13 GCs already observed by Chomiuk et al. (2008), finding their LRIS and our DEIMOS radial velocities to be consistent within the errors, but with a mean difference of  $\sim 12 \text{ km s}^{-1}$  (see §4.2). Therefore, we add the remaining 6 Chomiuk GCs corrected for the velocity offset to our GC sample. The final GC catalogue consists of 27 GC radial velocities.

Our confirmed GCs appear to be distributed within 2 arcmin  $\sim 7.7$  kpc from the galaxy centre, reflecting the expected poor extent of the underlying GC subpopulation. The mean velocity of the system ( $V_{\text{sys}} = 847 \pm 20 \text{ km s}^{-1}$ ) is in good agreement with both Chomiuk et al. (2008) and literature data. As this galaxy appears to be unimodal in colour, we fit the kinematics of all the GCs without any split in colour and we compare the results with the long-slit data of Simien & Prugniel (2000). We find that the GC system of NGC 7457 is rapidly rotating along the photometric major axis, with a flat rotation curve at  $\sim 80 \text{ km s}^{-1}$  up to  $2R_{\text{eff}}$ . In contrast, the velocity dispersion is low ( $< 50 \text{ km s}^{-1}$ ) at all radii. The agreement with the ATLAS<sup>2D</sup> velocity map is also very good

(Figure 13). We will discuss the implication of these results in more detail in §10.4.

## 6 GC FORMATION MODELS

Having determined the photometric and kinematic properties of our GC sample, in the following sections we will discuss these results as a whole. We look for common kinematic features that might retain key information about the formation history of the galaxies themselves and then we compare these results to theoretical models. In order to do so, it is first worth giving a brief summary of the main GC formation scenarios proposed in the literature, focusing on their kinematic predictions.

To date, the formation of GC bimodality has been investigated both in a cosmological context (Kravtsov & Gnedin 2005; Diemand et al. 2005; Moore et al. 2006) and at smaller scales, with models fine tuned to reproduce the properties of specific galaxies (see Vesperini et al. 2003 for NGC 4486 or Deason et al. 2011 for the Milky Way and M31). The challenge of producing simulations of GC bimodality formation is intertwined with our poor understanding of how GC systems formed in the first place (e.g., Beasley et al. 2002; Elmegreen et al. 2012). As a consequence, the three classic formation scenarios proposed in the literature and summarized below have few, if any, theoretical predictions directly comparable with the observations. In particular, there is a general dearth of GC kinematics predictions.

In the *major merger scenario* (Ashman & Zepf 1992) two or more gas-rich disk galaxies with pre-existing blue and red GC subpopulations merge to form an elliptical galaxy. New red GCs may form from the star formation induced by the merger (Bekki et al. 2002).

This scenario has been simulated by Bekki et al. (2005) (hereafter B+05). In this simulation the pre-existing blue and red GCs are assumed to have a Milky Way-like spatial distribution, but they are both pressure-supported. This is a reasonable assumption for the blue but not for the red GCs of the Milky Way that are known to be rotation-supported (Côté 1999; Deason et al. 2011). B+05 predicted that a merger with even mass-to-mass ratio produces strong rotation for both GC subpopulations in the outer regions of the remnant. This result is independent of the orbital configuration of the merger. The velocity dispersion profile is predicted to decrease with radius, but it would be flatter in case of multiple mergers. Also, the blue GCs are expected to show a larger central velocity dispersion than red GC subpopulation. Finally, the ratio of the maximum rotational velocity  $V_m$  to the central velocity dispersion  $\sigma_0$  of the GC systems ranges from 0.2 to 1.0 within  $6R_{\text{eff}}$  for both the blue and red GC subpopulations, but most GC systems, viewed from various angles, have  $(V_m/\sigma_0) < 0.5$ . Bekki & Peng (2006) carried out a simulation similar to that of B+05 (with the rotation of the disk in the spiral progenitors included), fine tuned to study the dynamics of the planetary nebulae (PNe) in elliptical galaxies. They found that the effect of the residual spin disk (additional to the initial orbital angular momentum) on the final PNe kinematics enhances the rotation at all radii, making the merger remnant rotation-supported.

In the *multiphase dissipational collapse scenario* (Forbes et al. 1997), GCs are the result of an early two phase collapse, and hence two main star formation episodes, that the galaxy undergoes. The blue GCs form during the first star formation episode in a metal-poor cloud, whereas red GC subpopulation form in a second phase after the gas in the galaxy is self-enriched. In this scenario, a fraction of blue GCs might also come from

accreted satellite galaxies, similar to the most recent two-phase galaxy formation model (Oser et al. 2010). No numerical simulations have been performed so far to test this model. Since the red GCs are coeval with the galaxy stellar component, Forbes et al. (1997) infer that they should share the same kinematic properties as the galaxy stars, and hence also the same spatial distribution. No significant rotation is expected for the blue GC subpopulation.

In the *dissipationless accretion scenario* (Côté et al. 1998), the red GCs form from the monolithic collapse of a giant protogalactic cloud, whereas the blue GCs are accreted from low mass galaxies due to mergers or tidal stripping. To date, simulations based on similar scenarios have been performed (e.g., Oser et al. 2010) but they do not include GC particles, and they have not made kinematic predictions. In addition to the observation of infalling co-moving groups, Côté et al. (1998) also infer that we should expect to observe blue GCs with radially biased orbits without overall rotation.

Bekki et al. (2008) (hereafter B+08) performed a high resolution N-body cosmological simulation combined with semi-analytic models. They found that almost half of the simulated  $10^5$  galaxies show clear bimodality in their GC metallicity distribution. The majority of GCs form in low-mass galaxies at redshift greater than 3 with the blue GCs being slightly older ( $< 1$  Gyr) than the red GC subpopulation. B+08 also made predictions for the overall kinematics of each GC system, whereas current spectroscopic observations only sample a smaller fraction of it. They find that the velocity dispersion of blue and red GC subpopulations increases with the total luminosity of the host galaxy and that the ratio of the velocity dispersion of the blue to red GC subpopulation is  $(\sigma_B/\sigma_R) \sim 1$  for a wide range of luminosity. Finally, they also predicted that the GC systems of most galaxies are mainly pressure supported with  $(V_{\text{rot}}/\sigma) < 0.3$ . This is in contrast with the wider range of  $V_{\text{rot}}/\sigma$  found by B+05.

## 7 GLOBAL RESULTS FROM OUR GC SAMPLE

In this section we summarize the results for the GC systems presented in this paper, including the three galaxies previously published by us (i.e., NGC 3115, NGC 4486, NGC 4494). Section 8 will incorporate other literature data, and tackle topics not covered here.

### 7.1 Spatial Distribution

Significant colour bimodality was detected in all the GC systems, except for NGC 7457. All GC system formation scenarios, as well as numerical simulations, predict that this bimodality should be reflected in different spatial distributions of the two subpopulations around the parent galaxy. A glance at Figure 6 reveals that this is also the case for our galaxy sample. Generally speaking, the red GCs are more centrally concentrated than the blue GCs, as already found in other studies (e.g., Schuberth et al. 2010; Faifer et al. 2011; Strader et al. 2011).

The advent of wide field imaging has shown that the radial distribution of the red GC subpopulation matches that of the host galaxy light, suggesting that they might have shared a similar formation history (Bassino et al. 2006). Here we have exploited the  $34 \times 22$  arcmin<sup>2</sup> field of view of our Suprime-Cam imaging to compare the GC surface density to the surface brightness of the respective host galaxy (shifted by an arbitrary constant). Qualitatively speaking, the galaxy starlight has a similar slope to that of the red

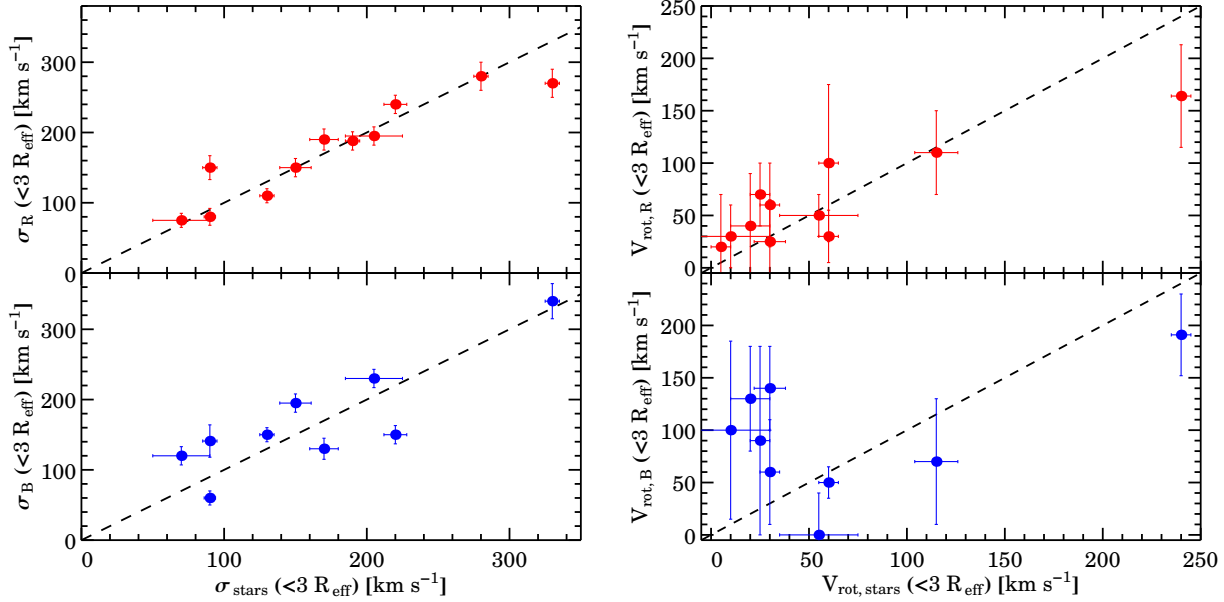


**Figure 14.** GC rotation velocities and velocity dispersions compared to the galaxy stars/PNe. Rotation velocities (*left panel*) and velocity dispersions (*right panel*) are extracted within  $3R_{\text{eff}}$ . The exact extraction radius is usually set to  $2R_{\text{eff}}$  but this threshold is arbitrarily adjusted by  $\pm 1R_{\text{eff}}$  in case the GCs do not overlap with the stellar data. The blue and the red GC subpopulations are shown in the *bottom* and *upper panel* respectively. Dashed lines represent a one-to-one relationship. Blue GC data for NGC 4365 and NGC 4278 are not shown due to limited radial range. NGC 7457 is not shown. The red GC subpopulation shows better agreement with stars than the blue GCs.

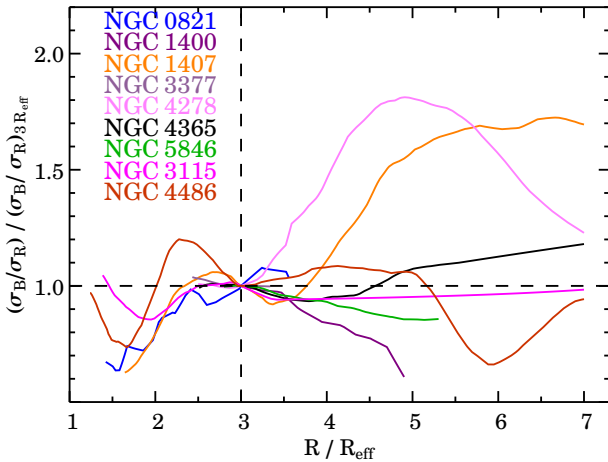


**Figure 15.** Velocity dispersion profiles. For each galaxy, we show the ratio of the velocity dispersion of blue to red GC subpopulations normalised to  $3R_{\text{eff}}$  (vertical dashed line) as a function of the effective radius. Different colours correspond to different galaxies. The horizontal and vertical lines show  $(\sigma_B/\sigma_R) = (\sigma_B/\sigma_R)_{3R_{\text{eff}}}$  and  $R = 3R_{\text{eff}}$ , respectively. NGC 7457 and NGC 4494 are not shown.

GC subpopulation. The discrepancies between the surface brightness and the GC spatial distribution in innermost regions (e.g., see NGC 4365 and NGC 1407 in Figure 6) is due to the core-like distribution of the GCs, that makes the GC density profile flatter. This feature is interpreted as the effect of the GC disruption, stronger in the central regions (Baumgardt 1998; Baumgardt & Makino 2003).

## 7.2 Rotation

We find a large variety of GC rotation profiles. Both the blue and red GCs show some degree of rotation, but there does not seem to be a clear correlation between the rotation patterns and the property of the host galaxy. A glance at Figure 11 reveals that the red GCs rotate more consistently with the photometric major axis than the blue GC subpopulation does. For our galaxy sample the photometric position angle coincides with the photometric major axis of the galaxy stars (except for NGC 4365), which means that the rotation velocity of the red GC subpopulation is similar to that of the galaxy stars. This is also true for the overall GC system of NGC 7457.

To quantify this phenomenon, in Figure 14 we compare the major axis rotation velocity of the blue and the red GC subpopulations within  $3R_{\text{eff}}$  to the rotation velocity of the stars and PNe (if available) at the same galactocentric distance. The exact extraction radius was set to  $2R_{\text{eff}}$ , but in some cases this was relaxed by  $\pm 1R_{\text{eff}}$  to maximise the overlap between the GCs and the stars. The rotation velocity of the host galaxy stars was extracted along the photometric major axis for all the galaxies, except for NGC 4365 in which the bulk of the stellar rotation is occurring along the photometric minor axis. The red GC rotation for our galaxies is similar to those of the host galaxy stars, at least for galaxies with a conspicuous amount of stellar rotation. On the other hand, the star-GC system coupling is also evident for only blue GC subpopulations, such as in NGC 4494, NGC 821 and NGC 3115.

The rotation of the blue GCs is more puzzling than the red GCs. Overall the rotation of the blue GCs is lower than the red GCs and often consistent with zero, yet we also detect minor axis rotation in NGC 821, also seen in PNe, in contrast with integrated starlight.

We detect GC rotation at large galactocentric radii for some galaxies. This feature is only significant in NGC 1407, NGC 4486 and only marginal in NGC 4278. The outer rotation occurs in the

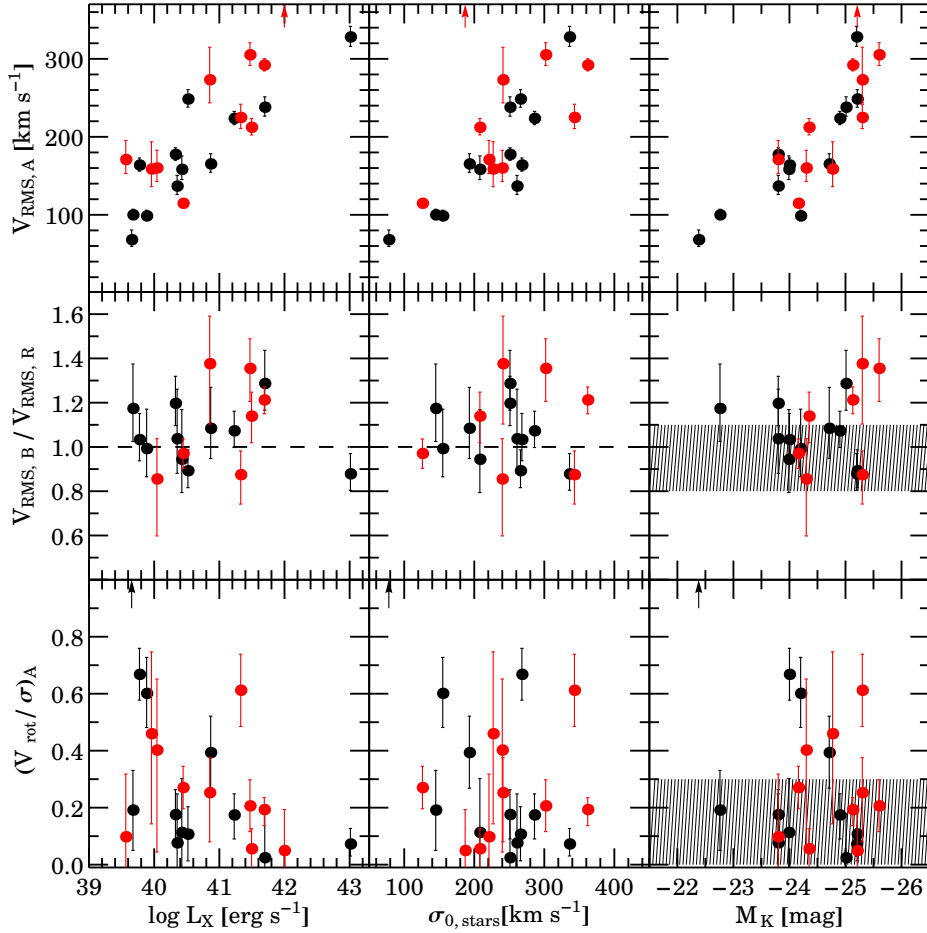


**Figure 16.** Summary of GC system kinematics as a function of the host galaxy properties. Literature data and our sample are shown as red and black points respectively. From the top to the bottom: root-mean-square velocity for the overall GC system ( $V_{\text{RMS,A}}$ ), ratio of the  $V_{\text{RMS}}$  of the blue to the red GC subpopulation ( $V_{\text{RMS,B}}/V_{\text{RMS,R}}$ ), ratio of the rotation velocity to the velocity dispersion for the overall GC system ( $(V_{\text{rot}}/\sigma)_A$ ). From the left to the right: X-ray luminosity ( $\log L_X$ ) from O’Sullivan et al. (2001) at the distance given in Table 1 and Table 7, central stellar velocity dispersion ( $\sigma_{0,\text{stars}}$ ) from Prugniel & Simien (1996) and total K-band magnitude ( $M_K$ ) from 2MASS. The black and red arrows indicate the position of NGC 7457 at  $(V_{\text{rot}}/\sigma)_A = 1.68$  and of NGC 3311 at  $V_{\text{RMS,A}} = 653 \text{ km s}^{-1}$ , respectively. The horizontal dashed line marks  $V_{\text{RMS,B}}/V_{\text{RMS,R}} = 1$  to guide the eye. The grey shaded shaded region represents the theoretical predictions from the cosmological simulation of Bekki et al. (2008).

same direction for both the blue and the red GC subpopulations and it usually coincides with the photometric major axis.

### 7.3 Velocity Dispersion

Our results show that the velocity dispersion profiles are quite flat for most of the galaxies, both as a function of radius (Figure 11) and as a function of the colour (Figure 12). The slope of the velocity dispersion profiles (including the contribution of the rotation) will be discussed below.

As for the rotation, we study how the velocity dispersion of the two GC subpopulations compares to the velocity dispersion of the host galaxy stars. We extract the velocity dispersion at the same galactocentric distances as done with the rotation. Figure 14 shows that the velocity dispersion of the red GC is very similar to that of the host galaxy stars in the region of overlap. Conversely, the blue GC subpopulations seem to avoid the one-to-one line. The standard deviation from the one-to-one line is  $22 \text{ km s}^{-1}$  and  $50 \text{ km s}^{-1}$  for the red and the blue GC subpopulations respectively.

To quantify the differences between the velocity dispersion

profiles of the two GC subpopulations, in Figure 15 we plot the ratio of the velocity dispersion of the blue GCs to the velocity dispersion of the red GCs ( $\sigma_B/\sigma_R$ ) normalised to  $3 R_{\text{eff}}$  as a function of the effective radius. In this case we show the velocity dispersion using rolling radial fits to appreciate the details of the profiles. Figure 15 shows that the ratio ratio  $(\sigma_B/\sigma_R)/(\sigma_B/\sigma_R)_{3 R_{\text{eff}}}$  is generally consistent with 1, but it increases towards the outer regions for some galaxies, as already observed for more massive galaxies (Lee et al. 2010).

The overall velocity dispersion profiles are in rough agreement with their merger remnants assembled via multiple mergers, with the velocity dispersion of the blue GCs being larger or equal to that of the red GCs. However, the model fails in reproducing the irregularity of some dispersion profiles (e.g., NGC 1407 and NGC 4278).

## 8 INCLUDING LITERATURE DATA

We examined the literature for galaxies with a reasonable number of GC radial velocity measurements. We require at least 20 spec-

Galaxy ID (1)	Hubble Type (2)	$M_K$ [mag] (3)	$D$ [Mpc] (4)	NGCs (5)	$V_{\text{rms,A}}$ [km s $^{-1}$ ] (6)	$V_{\text{rms,B}}$ [km s $^{-1}$ ] (7)	$V_{\text{rms,R}}$ [km s $^{-1}$ ] (8)	$(V_{\text{rot}}/\sigma)_A$ (9)	$(V_{\text{rot}}/\sigma)_B$ (10)	$(V_{\text{rot}}/\sigma)_R$ (11)	Ref. (12)
NGC 1380	SA0	-24.3	17.1	42	160 $^{+23}_{-17}$	142 $^{+38}_{-25}$	170 $^{+32}_{-22}$	0.39 $^{+0.25}_{-0.35}$	0.32 $^{+0.79}_{-0.54}$	0.05 $^{+0.30}_{-0.22}$	P+04
NGC 1399	E1	-25.1	19.4	738	292 $^{+8}_{-8}$	325 $^{+13}_{-12}$	266 $^{+10}_{-9}$	0.19 $^{+0.04}_{-0.05}$	0.28 $^{+0.06}_{-0.06}$	0.07 $^{+0.06}_{-0.08}$	S+10
NGC 3311	cD	-25.2	46.7	116	653 $^{+48}_{-40}$	—	—	0.03 $^{+0.14}_{-0.12}$	—	—	M+11
NGC 3379	E1	-23.7	10.2	39	171 $^{+24}_{-18}$	—	—	0.08 $^{+0.22}_{-0.15}$	—	—	P+06; B+06
NGC 3585	E6	-24.7	19.5	20	159 $^{+35}_{-23}$	—	—	0.43 $^{+0.28}_{-0.31}$	—	—	P+04
NGC 3923	E4	-25.3	22.3	79	273 $^{+42}_{-29}$	273 $^{+42}_{-29}$	200 $^{+26}_{-19}$	0.24 $^{+0.12}_{-0.16}$	0.31 $^{+0.26}_{-0.27}$	0.00 $^{+0.14}_{-0.22}$	N+12
NGC 4472	E2	-25.6	16.7	225	305 $^{+15}_{-14}$	334 $^{+22}_{-19}$	256 $^{+22}_{-19}$	0.19 $^{+0.09}_{-0.10}$	0.27 $^{+0.10}_{-0.10}$	0.08 $^{+0.14}_{-0.07}$	C+03
NGC 4636	E2	-24.3	14.2	259	212 $^{+11}_{-10}$	226 $^{+18}_{-15}$	200 $^{+15}_{-12}$	0.05 $^{+0.07}_{-0.11}$	0.09 $^{+0.14}_{-0.12}$	0.18 $^{+0.13}_{-0.10}$	L+08
NGC 4649	E2	-25.3	16.3	121	225 $^{+17}_{-14}$	209 $^{+20}_{-16}$	257 $^{+37}_{-26}$	0.61 $^{+0.12}_{-0.12}$	0.59 $^{+0.16}_{-0.15}$	0.70 $^{+0.24}_{-0.25}$	H+08
NGC 5128	S0	-24.1	4.1	449	115 $^{+5}_{-5}$	113 $^{+7}_{-6}$	117 $^{+7}_{-7}$	0.26 $^{+0.08}_{-0.05}$	0.25 $^{+0.10}_{-0.11}$	0.28 $^{+0.09}_{-0.11}$	W+10

**Table 7.** Kinematical properties of literature GC systems. The host galaxy name (1) and Hubble Type (2) are from NED database. K band absolute magnitude (3) is from 2MASS apparent magnitude at the distances given in column 4 and corrected for the foreground Galactic extinction from NED database. The distance in Megaparsec (4) was obtained by subtracting 0.06 mag (Mei et al. 2007) from the distance modulus from Tonry et al. (2001), except for NGC 3311 for which we adopt the distance of the Hydra I cluster of  $(m - M) = 33.37$  mag (Mieske et al. 2006). The number of spectroscopically confirmed GC system (5) is after the outliers filtering as described in the text. Columns (6), (7) and (8) are the root-mean-square velocity  $V_{\text{rms}}$  for all, blue and red GC subpopulations respectively. Columns (9), (10) and (11) are the  $(V/\sigma)$  value for all, blue and red GC subpopulations respectively. The data references are: P+04 (Puzia et al. 2004); S+10 (Schuberth et al. 2010); M+11 (Misgeld et al. 2011); P+06 (Pierce et al. 2006); B+06 (Bergond et al. 2006); N+12 (Norris et al. 2012); C+03 (Côté et al. 2003); H+08 (Hwang et al. 2008); L+08 (Lee et al. 2008); W+10 (Woodley et al. 2010).

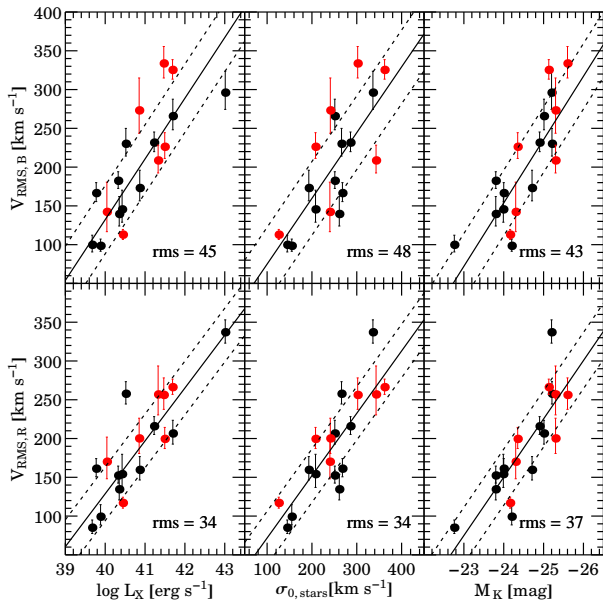


**Figure 17.** GC system  $V_{\text{rms}}$  as a function of the host galaxy properties. Literature data and our sample are shown as red and black points, respectively. The top and the bottom panels represent the velocity dispersion of the red and blue GC subpopulations as a function of the X-ray luminosity ( $\log L_X$ ), central stellar velocity dispersion ( $\sigma_{0,\text{stars}}$ ) and total K-band magnitude ( $M_K$ ), respectively. The solid and dashed lines represent the weighted linear fit to the data and its rms in km s $^{-1}$  quoted on the bottom right of each panel, respectively. The dependence of red GC subpopulation on the galaxy properties is tighter than for the blue GCs.

trioscopically confirmed GCs for a galaxy to be included in the literature sample. We use the same friendless algorithm as described in §4.1 to clip outliers in radius-velocity space. This selection returned ten GC systems, which are summarized in Table 7. Most of these galaxies are dominant group/cluster galaxies discussed in Lee et al. (2010), whereas the less massive galaxies are part of the survey of

Puzia et al. (2004). We also include NGC 3923 from Norris et al. (2012) which shows strong signatures a recent interaction. A first comparison between our GC dataset and external datasets was already given in Figure 2 in which we showed that we cover a wider range of mass with three times better velocity accuracy than previous studies.

We ran the kinematic likelihood code on the literature galaxies to get the *overall* best fit values to eq. 4, but we do not show the kinematic radial profiles for the literature sample. We investigate the kinematics of blue and red GC subpopulations for seven out of ten galaxies using the dividing colour quoted in the respective papers. For consistency with the kinematic analysis of our galaxies, we do not exclude UCD candidates from the literature data. We find that our likelihood-method tends to reduce both the velocity dispersion (by  $\sim 10$  km s $^{-1}$ ) and the rotation amplitude (up to  $\sim 30$  km s $^{-1}$ ) if the contribution of the rotation is low ( $V_{\text{rot}}/\sigma < 0.4$ ). We attribute this discrepancy to the fact that some previous GC kinematics studies have employed error-weighted least-square rotation fittings that are less appropriate for a system with an intrinsic dispersion. Another explanation might be that, to our knowledge, previous studies have never explicitly taken into account the bias introduced by an unconstrained position angle (see §4.3), which has an important effect at lower velocities. It is important to note that the maximum-likelihood approach does not alter the general results of previous works.

A final caveat to bear in mind concerns the different kinematic axes convention. Based on the fit of the GC radial velocities with the position angle (Figure 10), we define the kinematic position angle as the angle between the direction of maximum rotation amplitude and North, that is 90 degrees away from the angular momentum vector. Some previous studies have instead defined the kinematic position angle as the direction around which the rotation is occurring. In other words, our kinematic major axis would correspond to the kinematic minor axes quoted by Lee et al. (2010). Our convention is in line with that used in other galaxy kinematic studies (e.g. ATLAS $^{3D}$ ). For the galaxy properties of the literature sample we use the same sources quoted in Table 1.

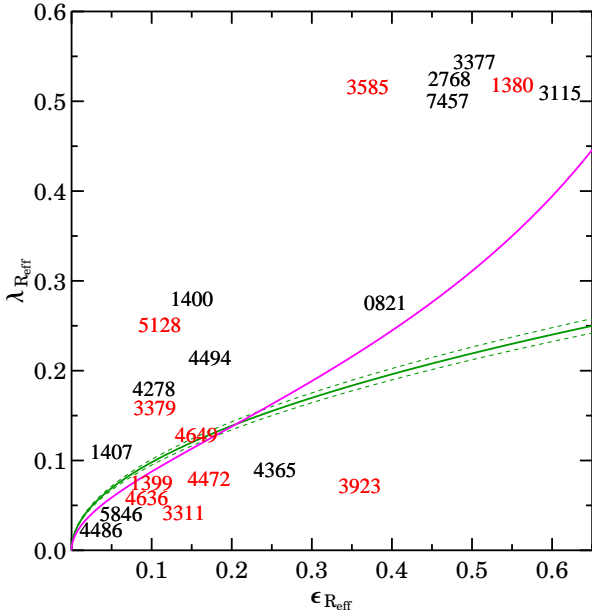


**Figure 18.** Rotational dominance parameter of the stellar component  $\lambda_{R_{\text{eff}}}$  versus the galaxy ellipticity  $\epsilon_{R_{\text{eff}}}$ . Both quantities are measured within  $1R_{\text{eff}}$ . Data points are represented by the NGC number of our galaxy sample (black) and literature data (red). Measurements are from Emsellem et al. (2011) if the galaxy is in ATLAS<sup>3D</sup>. If not they are estimated from literature data (see text). The magenta curve is the inferred edge-on average relation for nearby fast-rotators. The solid green curve is  $(0.31 \pm 0.01) \times \sqrt{\epsilon_{R_{\text{eff}}}}$ , with the dashed lines representing its uncertainties. Galaxies are divided into fast-rotators and slow-rotators if they are above or below the green curve respectively.

## 9 RESULTS

In this section we analyze the extended sample of 22 GC systems (literature plus our own galaxies), 18 of which have kinematics for both GC subpopulations. We carry out a number of tests to compare the kinematic properties of the two subpopulations with each other and with host galaxy properties.

### 9.1 Correlations with host galaxy properties

In Figure 16 we show the GC system kinematics as a function of the general properties of the host galaxies. We now have the chance to better constrain some relations examined by Lee et al. (2010) that were uncertain because of their limited sample size of six galaxies (see their figure 12).

The upper panels of Figure 16 show that, as found from previous studies, a correlation exists between  $V_{\text{rms}}$  of the GC systems and their respective host galaxy X-ray luminosity  $L_X$ , central velocity dispersion of the stars  $\sigma_0$  and absolute  $K$ -band magnitude  $M_K$ . We find that these correlations also hold for less massive galaxies. The correlations with galaxy properties are always tighter for our GC dataset as consequence of the improved reliability of our velocity measurements.

The correlation of  $V_{\text{rms}}$  with galaxy properties holds when we plot the  $V_{\text{rms}}$  of the blue and red GC subpopulations separately (see Figure 17). The main difference here is that the two subpopulations scatter differently with respect to the best fit lines. The rms of this difference for the blue GCs is systematically larger for the red GCs.

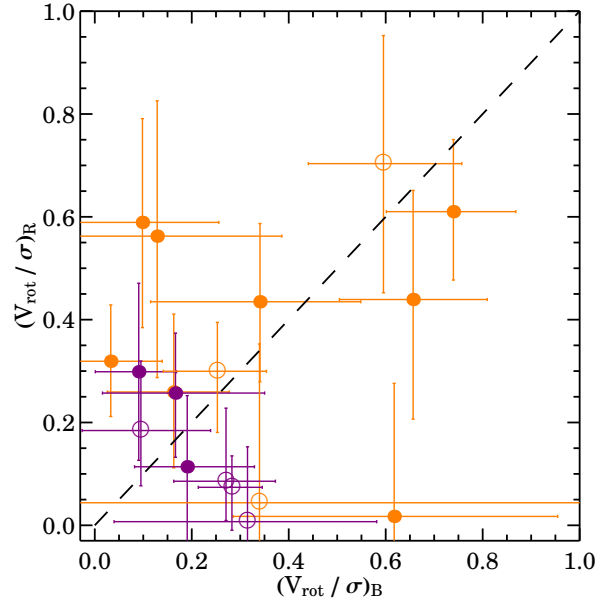


**Figure 19.** The rotational dominance parameter of GC systems. The plot compares the  $(V_{\text{rot}}/\sigma)$  parameter of the blue GCs  $(V_{\text{rot}}/\sigma)_B$  to that of the red GCs  $(V_{\text{rot}}/\sigma)_R$ . The dashed line marks a one-to-one line. GC systems are colour coded according to the kinematics of the host galaxy: purple if slow-rotators and orange if fast-rotators. Filled and open circles represent our GC systems and the data from the literature, respectively.

In Figure 16, the middle panel shows that most of the GC systems have  $V_{\text{rms},B}/V_{\text{rms},R} \geq 1$ . This is seen more clearly as a function of the X-ray luminosity which is larger in galaxies with an extended massive halo to which most of the blue GCs are thought to belong (Forbes et al. 2012). These results are in general agreement with the cosmological simulation of B+08 that predicted the  $V_{\text{rms},B}/V_{\text{rms},R}$  ratio to be slightly  $\geq 1$  for a wide range of host galaxy magnitudes. We also tested the significance of the apparent correlation between  $V_{\text{rms},B}/V_{\text{rms},R}$  and  $M_K$  finding a Spearman's rank correlation coefficient of  $r_s = 0.35$ , implying that a correlation is unlikely.

In the bottom panel of Figure 16 we quantify the GC system rotation by studying the overall  $(V_{\text{rot}}/\sigma)$ , which estimates the contribution of the GC rotation over its random motions. We find that galaxies are spread between  $0 < (V_{\text{rot}}/\sigma)_A < 0.8$  except for NGC 7457 with  $(V_{\text{rot}}/\sigma)_A = 1.68$ . It also appears that galaxies with lower  $L_X$  and lower  $\sigma_0$  are more rotation-supported than other galaxies. The bulk of GC systems with  $(V_{\text{rot}}/\sigma) \geq 0.3$  is consistent with cosmological simulation of B+08. However, as previously discussed, trends of rotation with radius and colour are also important to examine.

### 9.2 Rotation

To make things clearer we divide the host galaxies into two kinematic groups that will be used throughout this section. After considering various possibilities, we finally decided to divide the GC systems according to the rotation dominance parameter of their host galaxy. We use the  $\lambda_{R_{\text{eff}}}$  parameter within  $1R_{\text{eff}}$  as defined in Cappellari et al. (2007) with a threshold of  $0.31 \times \sqrt{\epsilon}$  to discriminate between slow and fast-rotators, where  $\epsilon_{R_{\text{eff}}} = 1 - (b/a)$  is the galaxy ellipticity. For our sample, we use  $\lambda_{R_{\text{eff}}}$



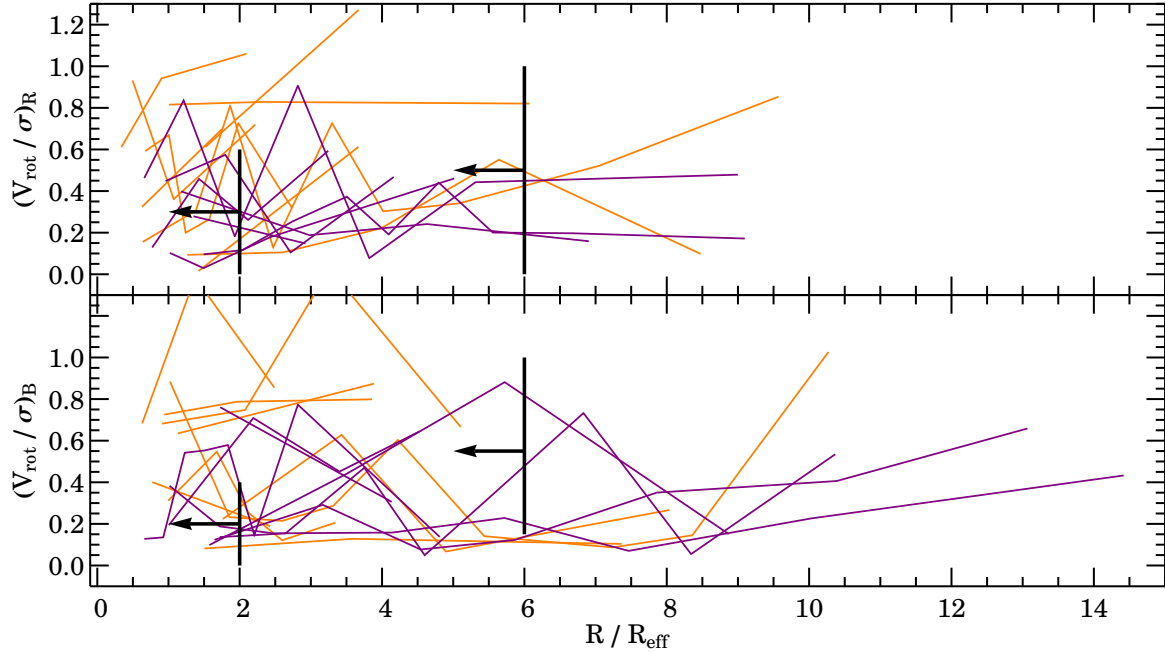


**Figure 20.**  $(V_{\text{rot}}/\sigma)_R$  radial profiles for our galaxy sample. Colours are as in Figure 19. The top and bottom panels show the rotational dominance parameter for the red and blue GC systems respectively. The black lines and arrows are predictions from Bekki et al. (2005) and represent the range of  $(V_{\text{max}}/\sigma_0)$  within 2 and  $6 R_{\text{eff}}$  respectively. There is no clear trend of  $(V_{\text{rot}}/\sigma)$  with radius as predicted from B+05.

from Emsellem et al. (2011) if the galaxy is in ATLAS<sup>3D</sup>, whereas we use the conversion formulae provided by the same authors to convert  $V_{\text{max}}/\sigma_0$  into  $\lambda_{R_{\text{eff}}}$ , where  $V_{\text{max}}$  and  $\sigma_0$  are the maximum rotation amplitude and the central velocity dispersion of the host galaxy respectively (Figure 18). This separation has the advantage of being independent of the galaxy inclination. It also allows us to test if the slow-fast rotator separation in the inner regions persists in the outer regions. The first group of galaxies is composed of slow-rotator galaxies and includes mostly round massive galaxies at the centre of groups or clusters. The second group includes fast-rotators but it covers a wide range of galaxy masses and morphologies, from E0 to S0. Fast-rotator galaxies with  $\lambda_{R_{\text{eff}}} > 0.25$  have stellar disk-like structures (photometric and/or kinematic) in the inner regions.

In Figure 19 we compare the *overall* rotational dominance parameter  $(V_{\text{rot}}/\sigma)$  of the blue and red GC subpopulations colour-coded according to their fast/slow rotator classification. We find that a dichotomy exists between the GC systems in slow and fast rotators. Most of the GC systems in the slow-rotator galaxies have  $0 < (V_{\text{rot}}/\sigma) < 0.3$ . Again, we want to emphasise that this does not necessarily imply that these systems lack rotation because if their rotation occurs only in a limited radial range, it may have been smeared out in the overall  $(V_{\text{rot}}/\sigma)$ . The GC systems in fast-rotator galaxies are more rotation-supported and in general at least one GC subpopulation has a conspicuous amount of rotation. There is a group of galaxies with  $(V_{\text{rot}}/\sigma) \sim 0.6$  which includes the fast-rotator galaxies with large  $\lambda_{R_{\text{eff}}}$ , but it also includes NGC 4649 with  $\lambda_{R_{\text{eff}}} \sim 0.12$ .

In Figure 20 we compare the radial  $(V_{\text{rot}}/\sigma)$  profiles for the blue and red GC systems with the numerical simulations of B+05. We note that B+05 quote the ratio of the maximum rotation velocity to the central velocity dispersion ( $V_{\text{max}}/\sigma_0$ ) within 2 and  $6 R_{\text{eff}}$ , whereas we plot the overall  $(V_{\text{rot}}/\sigma)$  in each radial bin.

Therefore, the predictions plotted in Figure 20 are typically upper limits. Another caveat is that B+05 simulate dry mergers, which leads to a systematic mismatch with the observed rotation in the galaxy centers. However, this effect is small for  $R \gtrsim 2R_{\text{eff}}$  (Hoffman et al. 2010), which is the radial range with better GC coverage and the most relevant for this study.

We find that for galaxies in the fast-rotator group, at least one GC subpopulation has  $(V_{\text{rot}}/\sigma) \neq 0$ . Slow-rotator galaxies have generally slower rotating GC systems. Although the comparison with B+05 suggests an overall agreement of our results with their predictions, the scatter in both  $(V_{\text{rot}}/\sigma)$  and in the simulations is too large to draw any strong conclusions. In more detail, the simulations predict  $(V_{\text{rot}}/\sigma)$  increasing monotonically with radius but we see no evidence for this feature in our data. Moreover, a direct comparison with B+05 simulations is not possible because they did not publish the  $(V_{\text{rot}}/\sigma)$  profiles to  $6R_{\text{eff}}$ . Figure 20 also shows that many GC systems are characterized by significant rotation spikes. These features might be partly caused by spatial incompleteness, outliers or projection effects. Alternatively, one speculative possibility is that these rotation spikes are the imprints of minor mergers. These events are expected (e.g., Vitvitska et al. 2002; Hetznecker & Burkert 2006), and observed (e.g., Romanowsky et al. 2011), to perturb the halo kinematics of massive galaxies. Detailed studies of GC system phase-space for each galaxy are needed to quantify this effect. Norris et al. (2012) also suggested that the missing outer rotation could be explained if the reservoir of angular momentum was located beyond the radii mapped by current GC system studies. This idea would be supported by the large rotation ( $V_{\text{rot}}/\sigma \sim 1.0$ ) we observe at  $\sim 10R_{\text{eff}}$  for both GC subpopulations of NGC 1407. However, at such galactocentric distances, results are uncertain because of spatial incompleteness and low number statistics. The same concerns

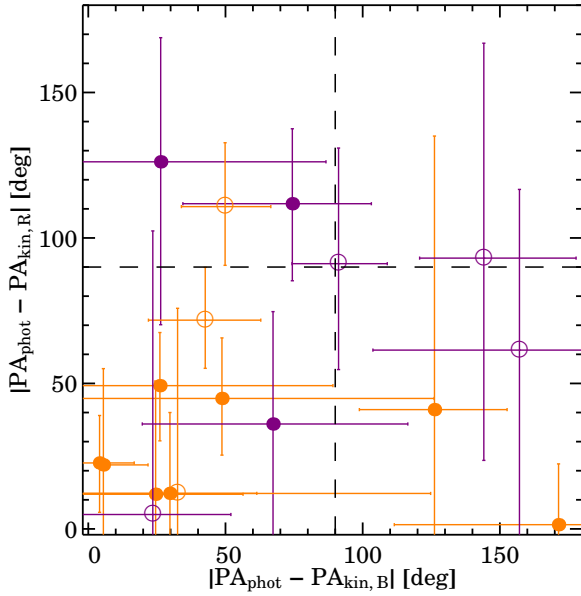


**Figure 21.** GC system position angle misalignments. The horizontal and the vertical axes show the misalignment between the photometric and the kinematic major axes for the blue and the red GC subpopulations respectively. Dashed lines mark a constant 90 degree angle. Rotation along the photometric major axis occurs at 0 deg, rotation along the minor axis at 90 deg and counter rotation at 180 deg. Galaxies with both a blue and red GC kinematic position angle unconstrained are not included for clarity. The rotation of the red GCs is more consistent with the photometric major axis.

were addressed by Strader et al. (2011) on the suspicious outer rotation ( $V_{\text{rot}}/\sigma \sim 0.6$ ) observed in NGC 4486.

### 9.3 Kinematic misalignment

It is also important to study how the rotation of the GC systems aligns with respect to the host galaxy isophotes. An eventual position angle misalignment might contain information about the triaxiality of the system (Krajnović et al. 2011).

In Figure 21 we compare the PA misalignment of the blue and red GC subpopulations. For clarity, we have removed from the plot galaxies for which neither the  $PA_{\text{kin}}$  of the blue nor of the red GC subpopulation was constrained. A caveat here is that we study *overall*  $PA_{\text{kin}}$  that will be biased by kinematic twists with radius. Broadly speaking, we note that most of the galaxies are located in the bottom-left quadrant of Figure 21 towards  $|\Delta PA| = 0$ , suggesting that the red GC subpopulation rotates more consistently with the photometric major axis than the blue GC subpopulation. We do not see a sharp separation between the GC systems in fast and slow-rotator galaxies. The GC rotation in fast-rotator galaxies seems to be equally consistent with the photometric major axis for both GC subpopulations.

The B+05 simulations also predicted kinematic misalignments with respect to the galaxy isophotes, albeit with an amplitude smaller than our findings. Depending on the orbital configuration, these authors can also reproduce the minor-axis rotation for the blue and red GC subpopulations, but they do not quantify this effect. Unfortunately, B+05 do not provide radial kinematic misalignments profiles, but they find that the rotation of both GC subpopulations in the outer regions of a merger remnant should be aligned along

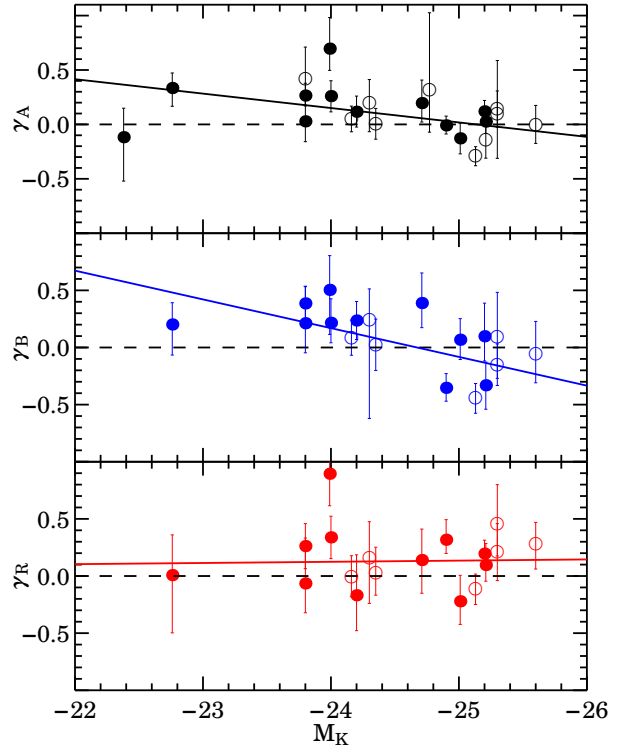


**Figure 22.** Log-slopes of the GC system  $V_{\text{rms}}^2$  profiles. Symbols are as in Figure 19. For each GC system the plot shows the best fit  $\gamma$  parameter to eq. 8 for all (top panel), blue (middle panel) and red GC subpopulation (bottom panel) as a function of the absolute magnitude  $M_K$  of the respective host galaxy. Lines are weighted linear fits to the data, whereas the dashed lines show an ideal flat  $V_{\text{rms}}$  profile ( $\gamma = 0$ ). The blue GC subpopulation tends to have a decreasing  $V_{\text{rms}}$  slope ( $\gamma < 0$ ) in more massive galaxies, while the red GC subpopulation has steady  $\gamma \geq 0$  over the whole magnitude range.

the photometric major axis, which is in rough agreement with our findings.

### 9.4 The slope of the $V_{\text{rms}}$ profile

The  $V_{\text{rms}}$ , sometimes freely named as velocity dispersion if the contribution of the rotation is low, is related the line-of-sight kinetic energy of a galaxy per unit of mass. Its profile has been classically used to model dark matter halos. Here, instead of showing the detailed  $V_{\text{rms}}$  profile for our GC system sample, we think it is more convenient to parametrize these profiles and to study their overall slopes. We use a maximum-likelihood approach to fit a power-law function to the non-binned  $V_{\text{rms}}$  profile, similarly to that done in eq. 4 for the GC system kinematics. In this case the  $\chi^2$  function to be minimized is (Bergond et al. 2006):

$$\chi^2 = \sum_{i=1}^{i=N} \left[ \frac{(V_{\text{rad},i} - V_{\text{sys}})^2}{V_{\text{rms}}^2 + (\Delta V_{\text{rad},i})^2} + \ln(V_{\text{rms}}^2 + (\Delta V_{\text{rad},i})^2) \right], \quad (7)$$

and the function to be modelled is:

$$V_{\text{rms}}^2(R) = V_{\text{rms},0}^2 \times (R/R_0)^{-\gamma}, \quad (8)$$

where  $R_0$  is a scale parameter, set here to the median galactocentric distance of each GC system.  $V_{\text{rms},0}$  and  $\gamma$  are two parameters free to vary, with the latter representing the slope of the power-law:

increasing if  $\gamma < 0$  and decreasing if  $\gamma > 0$ . Uncertainties on this method were obtained by bootstrapping the sample 2000 times in order to obtain the 68 per cent confidence levels.

Bearing in mind that the shape of the profile might change with radius (see the velocity dispersion profile of NGC 1407), in Figure 22 we show the best fit  $\gamma$  for each GC subpopulation (including the combination of the two) as a function of the host galaxy magnitude. The overall slope of the  $V_{\text{rms}}^2$  profile ( $\gamma$ ) of the GC systems is generally positive, but it becomes  $\leq 0$  for brighter galaxies, implying a constant or even increasing  $V_{\text{rms}}$  profile. If we now consider the blue and red GC subpopulations separately, it is clear that this effect is caused *only* by the blue GC subpopulations in galaxies with  $M_K < -25$  mag. The red GC subpopulations are always consistent with having  $\gamma \geq 0$  and a linear fit to the data suggest no significant trend with the magnitude. It is not clear why we do not observe  $\gamma \leq 0$  also for the red GC subpopulation. The two GC subpopulations might have different orbital configurations as a consequence of different formation histories and this would alter the shape of the  $V_{\text{rms}}$  profiles. Therefore, it is important also to study the orbits of the GC systems.

## 9.5 Kurtosis

The galaxy anisotropy has classically been measured through the parameter  $\beta$  that gives the relative ratio of the tangential to the radial velocity dispersion for a given dynamical tracer (Binney & Tremaine 2008). The calculus of  $\beta$  for our GC systems is not a topic of this paper and we will instead keep things simple by calculating the kurtosis  $\kappa$  that measures the deviation of a velocity distribution from a Gaussian. In the regime of a constant velocity dispersion the kurtosis provides a rough estimate of the GC orbits. These will be radial ( $\kappa > 0$ ), isotropic ( $\kappa = 0$ ) or tangential ( $\kappa < 0$ ), respectively. Broadly speaking we measure the fourth-order velocity moment:

$$\kappa = \frac{1}{N} \sum_{i=1}^N \frac{(V_{\text{rad},i} - V_{\text{sys}})^2}{V_{\text{rms}}^4} - 3 \pm \sqrt{\frac{24}{N}}, \quad (9)$$

but in practice we will use a more complicated bias-corrected formula from Joanes & Gill (1998).

We divide the radial kurtosis profiles in two radial bins in order to have roughly the same number of GCs in each bin. In this case the required number of GC radial velocities per bin is larger because the uncertainties are  $\propto N^{1/2}$ . We require at least 30 GCs per bin and this excludes smaller galaxies like NGC 1400 or NGC 821. As the calculation of  $\kappa$  does not take the GC radial velocity uncertainties into account, a bias might be present due to the different velocity resolution of the literature and of our GC samples. Results are presented in Figure 23.

We find that in the innermost bin most of the GC systems have  $\kappa_B \leq 0$  and  $\kappa_R \leq 0$ , suggesting isotropic or even tangential orbits. This is also true for kurtosis in the outer bin, but some galaxies (such as NGC 4365, NGC 4486 and NGC 4472) have the tendency of having more radially-biased orbits. In all cases the kurtosis of the blue and red GCs are consistent with isotropic orbits.

## 10 DISCUSSION

### 10.1 GC kinematic bimodality

The origin of GC colour bimodality is still an area of debate. On the theoretical side, there is a lack of consensus regarding the lead-

ing processes that drive the formation of GC systems (i.e. merging, collapse, accretion) and whether one (see Muratov & Gnedin 2010) or more of these processes (e.g., Lee et al. 2010) are needed to explain the observed colour bimodality. The contrasting numerical predictions are in part due to the diverse recipes with which simulations were built (Bekki et al. 2005, 2008; Moore et al. 2006; Kravtsov & Gnedin 2005; Diemand et al. 2005), but they might also reflect a real diversity of formation mechanisms that built up the GC systems in the first place.

On the observational side, the GC colour bimodality has been generally accepted because the two colour subpopulations differ in mean size and spatial distribution, and they depend differently on host galaxy properties (Forbes et al. 1997; Peng et al. 2006). Recently, the colour bimodality itself has been claimed to be an artifact of a strongly non-linear colour-metallicity relation (Yoon et al. 2006, 2011), which would make the metallicity distribution of a GC system unimodal, skewed towards metal-poor metallicities. The resulting metallicity distribution function would be more metal-rich than the one classically obtained with linear, or broken linear, colour-metallicity relations (Peng et al. 2006; Faifer et al. 2011; Sinnott et al. 2010; Alves-Brito et al. 2011).

We have found that GC systems around most of the surveyed galaxies have different kinematics between the blue and red sides of their GC colour distribution. This includes different kinematic position angle, rotation amplitudes and velocity dispersions. The kinematics generally change smoothly with the GC colour, but we also observe cases in which there is a sharp kinematic transition corresponding to the blue-red dividing colour (see NGC 821, NGC 1407 and NGC 3377 in Figure 12). *Our kinematic results are therefore strong evidence against colour bimodality simply being a consequence of a strong non-linear colour-metallicity relation.*

Most of the surveyed galaxies have small, yet significant, blue/red kinematic diversity (especially in their velocity dispersion profiles). The fact that we do not see any sharp kinematic transition with colour in all galaxies is not surprising because these systems lack intrinsic rotation of both GC subpopulations. Therefore, the rotation amplitude of GC systems can be insensitive for testing kinematic bimodality, especially for massive galaxies, for which one has instead to rely on other proxies such as the slope of the  $V_{\text{rms}}$  profile (Figure 22).

### 10.2 The star-GC system connection

Although the link between the red GCs and the host galaxy was somewhat expected from their similar spatial distributions, its kinematic confirmation was limited to a handful of galaxies (Schuberth et al. 2010; Norris et al. 2012; Romanowsky et al. 2009; Strader et al. 2011). The results that we found for our galaxy sample are diverse in this regard.

On one side we find excellent agreement between the kinematics of the stars (and/or PNe) and that of the red GCs, indicating that the coupling between stars and GC systems holds also for less massive galaxies. On the other hand, we have also found galaxies in which the blue GCs behave as the galaxy stars or, more interestingly, as the PNe. NGC 3377 and NGC 821 are two examples. These are very similar field disk galaxies with a falling stellar rotation curve. However, the blue GCs in NGC 3377 do not rotate and are decoupled from the PNe. Conversely, in NGC 821 blue GCs mimic the minor axis rotation of the PNe, but not of the stars. What is most surprising in the latter case is indeed the fact that the PNe are decoupled from the stars as well. Based on stellar population inferences, Proctor et al. (2005) concluded that NGC 821 has un-

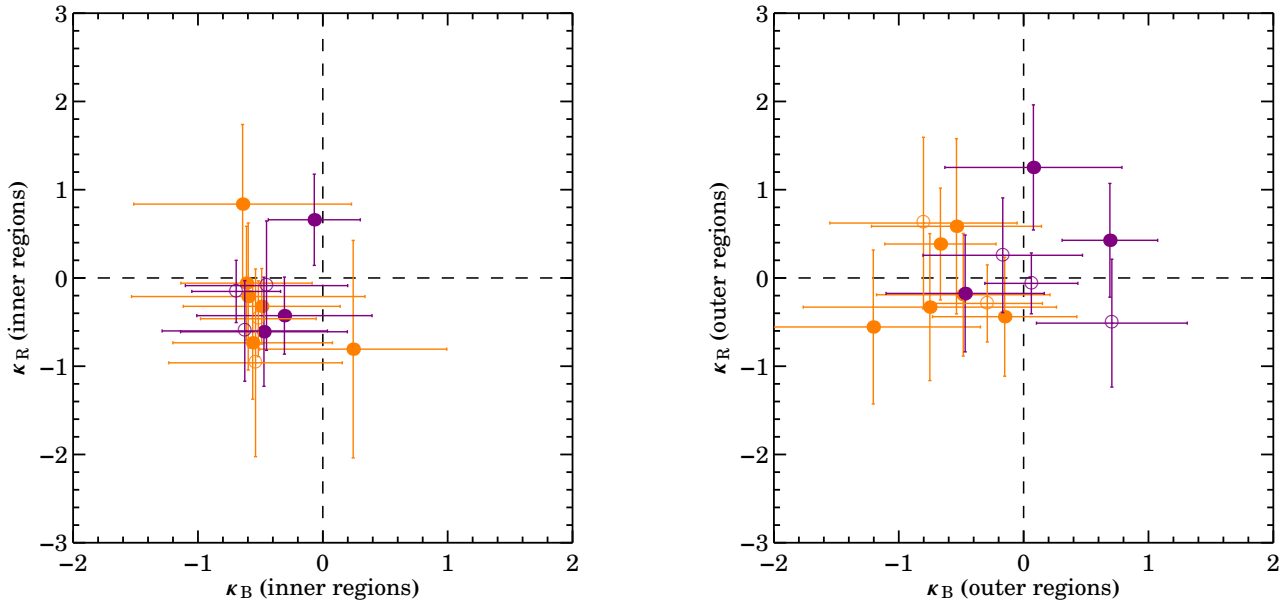


**Figure 23.** GC system velocity kurtosis. Symbols are as in Figure 19. The plot compares the kurtosis  $\kappa$  of the blue and red the GC systems in the inner (left panel) and outer radial bins (right panel). Dashed lines represent Gaussian distributions at  $\kappa = 0$ . GC system orbits are tangential and radial if  $\kappa < 0$  and  $\kappa > 0$  respectively.

dergone a minor merger or tidal interaction in the last 4 Gyr. Our results would support this scenario. However, it remains to be explained why the PNe are not akin to the underlying stars and how this feature can influence the dark matter estimate of this galaxy (Romanowsky et al. 2003).

How the star-GC system connection arose in the early times is still an open debate. Galaxy mergers may contribute to building the GC system of the remnant. Bekki et al. (2002) have shown that tidal shocks induced by galaxy merging can compress giant molecular clouds to form both new metal-rich GCs and stars. However, based on stellar population studies, Forbes et al. (2007) have shown that most of the red GCs are consistent with being uniformly old, and few, if any, formed in late epoch gaseous mergers.

A possible consensus scenario may arise from the idea that part of the red GCs might have formed during the early turbulent phases of galaxy formation at  $z \sim 2$  (Kravtsov & Gnedin 2005; Shapiro et al. 2010). At this redshift, galaxies are characterised by fast rotating thick discs (Elmegreen et al. 2009) fragmented into super-star forming clumps. Observations have shown that the origin of these clumps is related to disc instability processes (Wisnioski et al. 2011), but they may be also caused by cold flows (Dekel et al. 2009). It is thought that these gas-rich clumps migrate inwards to feed the nascent bulge (dragging along newly formed metal-rich GCs) and losing their rotational motion to dynamical friction, finally acquiring a typical  $V_{\text{rot}}/\sigma < 1$  for the bulge. During this migration,  $\sim 50\%$  of the clump mass will be stripped off and it will end up forming a rotationally supported disk (Bournaud et al. 2007).

This formation mechanism seems to qualitatively explain the spatial and kinematic similarity between stars and red GCs. However, as far as we know, no numerical simulations have to date been produced to directly compare observations with the kinematics of the red GCs forming during the ‘gas-rich clump-driven phase’. Also, the study of dwarf ellipticals in the Virgo cluster (Beasley et al. 2009) and in the Sculptor group (Olsen et al. 2004)

suggested that disks may have been significant sites of GC formation at early times.

The poor radial overlap between studies of galaxy stars and GC systems complicates the kinematic comparison between these two. Extended stellar kinematic studies, a la Proctor et al. (2009), will help to test the galaxy star-GC system connection. Also, it will be interesting to see what is the role of the PNe in this scenario and if the PNe-GCs connection in NGC 821 is the rule rather than the exception.

### 10.3 Orbital anisotropy

The GC orbital anisotropy, in this context represented by the kurtosis  $\kappa$ , can provide other clues about the formation of GC bimodality. Theoretical studies predict that dark matter haloes, including the baryonic tracers within them, have radially-biased orbits in their outer regions (McMillan et al. 2007; Prieto & Gnedin 2008; Dekel et al. 2005). However, the small number of studies in this field, which have usually employed deep integrated stellar light and PNe, seems to suggest that early-type galaxies harbour quasi-isotropic orbits (Gerhard et al. 1998; Douglas et al. 2007; de Lorenzi et al. 2009; Napolitano et al. 2009, 2011; Deason et al. 2011). How does this compare to the GC anisotropy?

Our analysis suggest that in the inner regions both GC subpopulations have isotropic or tangential orbits, whereas in the outer regions there is a hint that some red GC systems might have radial orbits. We recognise that in both cases the GC orbits are still consistent with being isotropic.

As already pointed out by Romanowsky et al. (2009), the lack of radially-biased orbits for the blue GC subpopulation might be connected to the evolutionary history of the GC system within the galaxy. Processes such as evaporation, dynamical friction and the consequent disruption of GCs may change the anisotropy. The disruption of GCs will be more efficient for those on radial orbits because they plunge deepest into the galaxy centre (Baumgardt 1998;

Baumgardt & Makino 2003). Accordingly, they will become less luminous and eventually vanish altogether, making GCs on tangential and isotropic orbits the most likely ones to survive and be observed today.

The GC orbital anisotropy will need further in-depth investigation but the overall pattern suggests that, if the blue GCs formed from the accretion or minor merger of satellite galaxies, some disruption effects have to be taken into account to explain the general absence of blue GC on radially-biased orbits. The scenario discussed above supports the idea that present day blue GCs were brought into the host galaxy via accretion and/or minor mergers.

The key point here is that the different GC orbits mean that the resulting  $V_{\text{rms}}$  profiles will be shaped by the orbits themselves (the mass-anisotropy degeneracy). Tangential anisotropy, for example, could mimic the presence of dark matter, whereas radial anisotropy could deplete it. Interestingly, we find that the blue GC subpopulations with tangentially-biased orbits tend to have increasing  $V_{\text{rms}}$  profiles (suggesting a more dominant dark-matter halo), whereas the red GC subpopulation is consistent with having a decreasing  $V_{\text{rms}}$  profile and more radial orbits. It will be interesting to test how a classic Jeans analysis that makes use of the different GC anisotropies found in this paper compares with recent studies that do not require assumptions on the dark matter halo (Walker & Peñarrubia 2011).

#### 10.4 NGC 7457: a case study for the formation of S0s

GC systems have been exploited to study the unsolved conundrum of the formation of lenticular galaxies (Barr et al. 2007; Arnold et al. 2011). In fact, it is still not clear whether S0s are quenched spirals: the remnant of a gentle gas shut off process that would preserve the kinematic signature of the progenitor spiral (Byrd & Valtonen 1990; Williams et al. 2010), or very disky ellipticals: the products of violent merging events (Bekki 1998; Cretton et al. 2001) that would diminish the original disk-rotation. The observational differences between these two scenarios are minimal and it also depends upon the galaxy environment (Kormendy & Bender 2012). S0s might still be rotationally supported if they form in uneven-mass galaxy mergers, with mass-ratio ratio between 1:4.5 and 1:10 (Bournaud et al. 2005).

In this context, a particularly interesting case study is offered by NGC 7457 that we have discussed in §5.9. This nearby lenticular galaxy contains in fact both signatures of a recent merger (Chomiuk et al. 2008) and a disky GC kinematics with a possible counter-rotating core in the innermost regions (Sil'chenko et al. 2002). In Figure 24 we compare the  $V_{\text{rot}}/\sigma$  profile of the stars (Simien & Prugniel 2000) and of our GC measurements (including the dataset of Chomiuk) with N-body simulations of merging with different mass-ratios of 1:3 (Cretton et al. 2001) and 1:10 (Bournaud et al. 2005), respectively. To do this, we select all the GCs within 1 arcmin from the photometric major axis and we construct two bins of 8 objects each.

Results in Figure 24 show that our data are in good agreement with the 1:10 remnant, even though the discrepancies occurring at small and large radii seem to suggest that the mass-ratio involved in the formation of this galaxy was probably smaller than this value. These results, along with the counter-rotating core in the centre and the intermediate-age GCs, seem to favour the minor merger scenario. We also note that the S0 galaxies simulated in B+05 are characterised by a strong rotation of the blue GC subpopulation if formed via merging, but we do not see any significant change of the GC kinematics with the GC colour in NGC 7457. This effect could

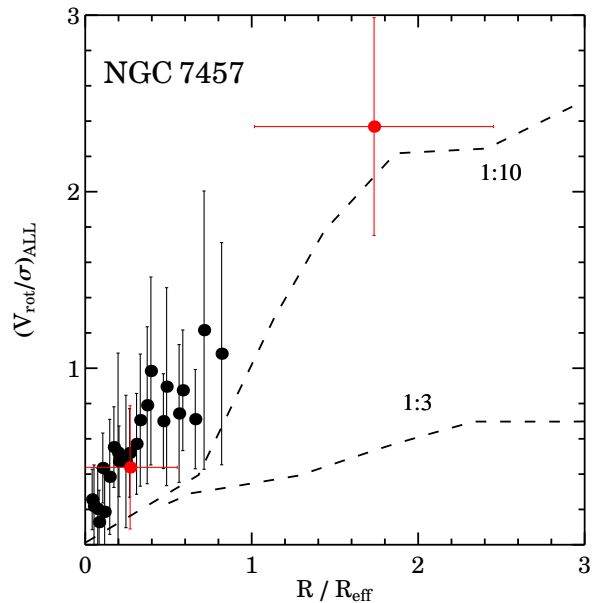


**Figure 24.** GC rotation rate in NGC 7457. GC data from this work (supplemented with Chomiuk et al. 2008) and long-slit data from Simien & Prugniel (2000) are shown as red and black points respectively. Also shown are the simulated merger remnant with a 1:10 (top dashed line) and 1:3 (bottom dashed line) mass ratio from Bournaud et al. (2005) and Cretton et al. (2001), respectively. Typical uncertainties on the merger remnant profiles are 15% at  $4 R_{\text{eff}}$ .

indeed be real, but it could also be driven by the low number statistics or by the large uncertainties ( $\pm 0.2$  mag) due to the conversion from *HST* to WIYN magnitudes.

## 11 SUMMARY AND CONCLUSIONS

We have examined the GC systems in twelve early-type galaxies (from lenticular to large ellipticals over a range of galaxy mass), nine of which published for the first time, with particular emphasis on the kinematics of their blue and red GC subpopulations.

For the new presented data, we have used wide-field ground-based imaging (mainly from Subaru/Suprime-cam) and *HST* observations, finding that eight out of nine galaxies have a significant bimodal GC colour distribution. The study of the spatial distribution of these two subpopulations has revealed that red GCs are generally more centrally concentrated and that they have a slope similar to the surface brightness of the underlying galaxy. This is in agreement with the idea that red and blue GC subpopulations trace the spheroidal component and the halo component of the host galaxies, respectively.

Multi-object spectroscopy was performed for a bright sample of GCs using Keck/DEIMOS that provided an average velocity resolution of  $\sim 15 \text{ km s}^{-1}$  (a factor of 3 better than most previous studies). We find a variety of kinematic profiles for both the blue and the red GC subpopulations. The salient results are:

- (i) The GC kinematics (rotation amplitude, velocity dispersion and rotation axis) varies with GC mean colour. In particular, we find GC systems which have a sharp kinematic transition at the blue-red dividing colour, implying that the GC colour bimodality is real and extends to kinematic bimodality.
- (ii) The rotation velocity and velocity dispersion of the red GC

subpopulation mimics the host galaxy stellar kinematics (including those of planetary nebulae). This property supports the scenario in which the red GCs form together with the bulk of stars of the host galaxy, for instance during the ‘turbulent disk phase’ at high redshift. The rotation of the blue GCs is typically consistent with zero, but their velocity dispersion is always higher or equal to that of the red GCs, especially in the outer regions.

(iii) The GC kinematics combined with other kinematic studies can reveal interesting features. We have found that the blue GCs in NGC 821 mimic the minor axis rotation of the PNe, but not that of the stars, suggesting that there might be a blue GC-PNe connection that trace a recent merging event. Also, our data seem to be consistent with the idea that the S0 galaxy NGC 7457 was formed via a minor merger with a 1:10 mass ratio.

We have supplemented our dataset with ten additional GC systems from the literature and compared their kinematics to host galaxy properties. We have compared our results with numerical simulations, finding no strong evidence that GC systems have formed via major-mergers. We find that the correlation between the  $V_{\text{rms}}$  of the GC systems and the mass of the host galaxy (from lenticular to massive ellipticals) holds for less massive galaxies and that it is tighter for the red GC subpopulation. The blue GCs in more massive galaxies have increasing  $V_{\text{rms}}$  profiles, whereas the red GCs have always shallower  $V_{\text{rms}}$  profiles. A study of the GC velocity kurtosis, suggests that blue GCs generally appear to be isotropic or tangentially-biased in the outer regions, unlike the red GCs which instead have more radially-biased orbits.

## 12 ACKNOWLEDGEMENTS

We thank the anonymous referee for the constructive feedback. AJB acknowledges the support of the Gordon & Betty Moore Foundation. CF acknowledges co-funding under the Marie Curie Actions of the European Commission (FP7-COFUND). KLR and JRH acknowledge support from NSF Career award AST-0847109 (PI: Rhode). This work was supported by the National Science Foundation through grants AST-0808099, AST-0909237 and AST-1211995. Some of the data presented herein were obtained at the W. M. Keck Observatory, operated as a scientific partnership among the California Institute of Technology, the University of California and the National Aeronautics and Space Administration, and made possible by the generous financial support of the W. M. Keck Foundation. The authors wish to recognise and acknowledge the very significant cultural role and reverence that the summit of Mauna Kea has always had within the indigenous Hawaiian community. The analysis pipeline used to reduce the DEIMOS data was developed at UC Berkeley with support from NSF grant AST-0071048. Based in part on data collected at Subaru Telescope and obtained from the SMOKA (which is operated by the Astronomy Data Centre, National Astronomical Observatory of Japan), via a Gemini Observatory time exchange. The authors acknowledge the data analysis facilities provided by IRAF, which is distributed by the National Optical Astronomy Observatories and operated by AURA, Inc., under cooperative agreement with the National Science Foundation. We have used the data products from the 2MASS, which is a joint project of the University of Massachusetts and the Infrared Processing and Analysis Centre/California Institute of Technology, funded by the National Aeronautics and Space Administration and the National Science Foundation. This research has made use of the NASA/IPAC Extragalactic Database (NED)

which is operated by the Jet Propulsion Laboratory, California Institute of Technology, under contract with the National Aeronautics and Space Administration. The figures for this article have been created using the excellent LevelScheme scientific figure preparation system (Caprio 2005).

## REFERENCES

- Abazajian K. N., Adelman-McCarthy J. K., Agüeros M. A., Allam S. S., Allende Prieto C., An D., Anderson K. S. J., Anderson S. F., Annis J., Bahcall N. A., et al. 2009, *ApJS*, 182, 543
- Alves-Brito A., Hau G. K. T., Forbes D. A., Spitler L. R., Strader J., Brodie J. P., Rhode K. L., 2011, *MNRAS*, 417, 1823
- Arnold J. A., Romanowsky A. J., Brodie J. P., Chomiuk L., Spitler L. R., Strader J., Benson A. J., Forbes D. A., 2011, *ApJ*, 736, L26
- Ashman K. M., Bird C. M., Zepf S. E., 1994, *AJ*, 108, 2348
- Ashman K. M., Zepf S. E., 1992, *ApJ*, 384, 50
- Ashman K. M., Zepf S. E., 1998, *The Observatory*, 118, 387
- Baba H., Yasuda N., Ichikawa S.-I., Yagi M., Iwamoto N., Takata T., Horaguchi T., Taga M., Watanabe M., Ozawa T., Hamabe M., 2002, in Bohlender D. A., Durand D., Handley T. H., eds, *Astronomical Data Analysis Software and Systems XI Vol. 281 of Astronomical Society of the Pacific Conference Series*, Development of the Subaru-Mitaka-Okayama-Kiso Archive System. p. 298
- Barr J. M., Bedregal A. G., Aragón-Salamanca A., Merrifield M. R., Bamford S. P., 2007, *A&A*, 470, 173
- Bassino L. P., Richtler T., Dirsch B., 2006, *MNRAS*, 367, 156
- Baumgardt H., 1998, *A&A*, 330, 480
- Baumgardt H., Makino J., 2003, *MNRAS*, 340, 227
- Beasley M. A., Baugh C. M., Forbes D. A., Sharples R. M., Frenk C. S., 2002, *MNRAS*, 333, 383
- Beasley M. A., Cenarro A. J., Strader J., Brodie J. P., 2009, *AJ*, 137, 5146
- Beasley M. A., Forbes D. A., Brodie J. P., Kissler-Patig M., 2004, *MNRAS*, 347, 1150
- Beasley M. A., Sharples R. M., Bridges T. J., Hanes D. A., Zepf S. E., Ashman K. M., Geisler D., 2000, *MNRAS*, 318, 1249
- Bekki K., 1998, *ApJ*, 502, L133
- Bekki K., Beasley M. A., Brodie J. P., Forbes D. A., 2005, *MNRAS*, 363, 1211
- Bekki K., Forbes D. A., Beasley M. A., Couch W. J., 2002, *MNRAS*, 335, 1176
- Bekki K., Peng E. W., 2006, *MNRAS*, 370, 1737
- Bekki K., Yahagi H., Nagashima M., Forbes D. A., 2008, *MNRAS*, 387, 1131
- Bender R., Saglia R. P., Gerhard O. E., 1994, *MNRAS*, 269, 785
- Bergond G., Zepf S. E., Romanowsky A. J., Sharples R. M., Rhode K. L., 2006, *A&A*, 448, 155
- Bertola F., Pizzella A., Persic M., Salucci P., 1993, *ApJ*, 416, L45
- Binney J., Tremaine S., 2008, *Galactic Dynamics: Second Edition*. Princeton University Press
- Blakeslee J. P., Cantiello M., Peng E. W., 2010, *ApJ*, 710, 51
- Blom C., Spitler L. R., Forbes D. A., 2011, *MNRAS*, p. 2118
- Bournaud F., Elmegreen B. G., Elmegreen D. M., 2007, *ApJ*, 670, 237
- Bournaud F., Jog C. J., Combes F., 2005, *A&A*, 437, 69
- Box M. J., 1971, *Journal of the Royal Statistical Society. Series B (Methodological)*, 33, pp. 171
- Brodie J. P., Larsen S. S., 2002, *AJ*, 124, 1410

- Brodie J. P., Romanowsky A. J., Strader J., Forbes D. A., 2011, *AJ*, 142, 199
- Brodie J. P., Strader J., 2006, *ARA&A*, 44, 193
- Brodie J. P., Strader J., Denicoló G., Beasley M. A., Cenarro A. J., Larsen S. S., Kuntschner H., Forbes D. A., 2005, *AJ*, 129, 2643
- Brough S., Forbes D. A., Kilborn V. A., Couch W., Colless M., 2006, *MNRAS*, 369, 1351
- Byrd G., Valtonen M., 1990, *ApJ*, 350, 89
- Cappellari M., Emsellem E., Bacon R., Bureau M., Davies R. L., de Zeeuw P. T., Falcón-Barroso J., Krajnović D., Kuntschner H., McDermid R. M., Peletier R. F., Sarzi M., van den Bosch R. C. E., van de Ven G., 2007, *MNRAS*, 379, 418
- Cappellari M., Emsellem E., Krajnović D., McDermid R. M., Scott N., Verdoes Kleijn G. A., Young L. M., Alatalo K., Bacon R., Blitz L., Bois M., Bournaud F., Bureau M., Davies R. L., 2011, *MNRAS*, 413, 813
- Caprio M., 2005, *Computer Physics Communications*, 171, 107
- Chies-Santos A. L., Larsen S. S., Kuntschner H., Anders P., Wehner E. M., Strader J., Brodie J. P., Santos J. F. C., 2011, *A&A*, 525, A20
- Chies-Santos A. L., Larsen S. S., Wehner E. M., Kuntschner H., Strader J., Brodie J. P., 2011, *A&A*, 525, A19
- Chies-Santos A. L., Pastoriza M. G., Santiago B. X., Forbes D. A., 2006, *A&A*, 455, 453
- Cho J., Sharples R. M., Blakeslee J. P., Zepf S. E., Kundu A., Kim H.-S., Yoon S.-J., 2012, *ArXiv e-prints*
- Chomiuk L., Strader J., Brodie J. P., 2008, *AJ*, 136, 234
- Coccatto L., Gerhard O., Arnaboldi M., 2010, *MNRAS*, 407, L26
- Coccatto L., Gerhard O., Arnaboldi M., Das P., Douglas N. G., Kuijken K., Merrifield M. R., Napolitano N. R., Noordermeer E., Romanowsky A. J., Capaccioli M., Cortesi A., de Lorenzi F., Freeman K. C., 2009, *MNRAS*, 394, 1249
- Cohen J. G., Blakeslee J. P., Ryzhov A., 1998, *ApJ*, 496, 808
- Cooper M. C., Newman J. A., Davis M., Finkbeiner D. P., Gerke B. F., 2012, in *Astrophysics Source Code Library*, record ascl:1203.003 spec2d: DEEP2 DEIMOS Spectral Pipeline. p. 3003
- Côté P., 1999, *AJ*, 118, 406
- Côté P., Marzke R. O., West M. J., 1998, *ApJ*, 501, 554
- Côté P., McLaughlin D. E., Cohen J. G., Blakeslee J. P., 2003, *ApJ*, 591, 850
- Côté P., McLaughlin D. E., Hanes D. A., Bridges T. J., Geisler D., Merritt D., Hesser J. E., Harris G. L. H., Lee M. G., 2001, *ApJ*, 559, 828
- Cretton N., Naab T., Rix H.-W., Burkert A., 2001, *ApJ*, 554, 291
- da Costa L. N., Willmer C. N. A., Pellegrini P. S., Chaves O. L., Rité C., Maia M. A. G., Geller M. J., Latham D. W., Kurtz M. J., Huchra J. P., Ramella M., Fairall A. P., Smith C., Lípári S., 1998, *AJ*, 116, 1
- Danese L., de Zotti G., di Tullio G., 1980, *A&A*, 82, 322
- Das P., Gerhard O., Coccatto L., Churazov E., Forman W., Finoguenov A., Böhringer H., Arnaboldi M., Capaccioli M., Cortesi A., de Lorenzi F., Douglas N. G., Freeman K. C., Kuijken K. a., 2008, *Astronomische Nachrichten*, 329, 940
- de Lorenzi F., Gerhard O., Coccatto L., Arnaboldi M., Capaccioli M., Douglas N. G., Freeman K. C., Kuijken K., Merrifield M. R., Napolitano N. R., Noordermeer E., Romanowsky A. J., Debattista V. P., 2009, *MNRAS*, 395, 76
- de Vaucouleurs G., 1991, *Science*, 254, 1667
- Deason A. J., Belokurov V., Evans N. W., 2011, *MNRAS*, 411, 1480
- Dekel A., Birnboim Y., Engel G., Freundlich J., Goerdt T., Mucoglu M., Neistein E., Pichon C., Teyssier R., Zinger E., 2009, *Nature*, 457, 451
- Dekel A., Stoehr F., Mamon G. A., Cox T. J., Novak G. S., Primack J. R., 2005, *Nature*, 437, 707
- Diemand J., Madau P., Moore B., 2005, *MNRAS*, 364, 367
- Dirsch B., Richtler T., Geisler D., Forte J. C., Bassino L. P., Gieren W. P., 2003, *AJ*, 125, 1908
- Douglas N. G., Napolitano N. R., Romanowsky A. J., Coccatto L., Kuijken K., Merrifield M. R., Arnaboldi M., Gerhard O., Freeman K. C., Merrett H. R., Noordermeer E., Capaccioli M., 2007, *ApJ*, 664, 257
- Elmegreen B. G., Elmegreen D. M., Fernandez M. X., Lemonias J. J., 2009, *ApJ*, 692, 12
- Elmegreen B. G., Malhotra S., Rhoads J., 2012, *ArXiv e-prints*
- Emsellem E., Cappellari M., Krajnović D., Alatalo K., Blitz L., Bois M., Bournaud F., Bureau M., Davies R. L., Davis T. A., de Zeeuw P. T., 2011, *MNRAS*, 414, 888
- Emsellem E., Cappellari M., Krajnović D., van de Ven G., Bacon R., Bureau M., Davies R. L., de Zeeuw P. T., Falcón-Barroso J., Kuntschner H., McDermid R., Peletier R. F., Sarzi M., 2007, *MNRAS*, 379, 401
- Faber S. M., Phillips A. C., Kibrick R. I., Alcott B., Allen S. L., Burrous J., Cantrall T., Clarke D., Coil A. L., Cowley D. J., Davis 2003, in Iye M., Moorwood A. F. M., eds, *Society of Photo-Optical Instrumentation Engineers (SPIE) Conference Series Vol. 4841 of Society of Photo-Optical Instrumentation Engineers (SPIE) Conference Series*, The DEIMOS spectrograph for the Keck II Telescope: integration and testing. pp 1657–1669
- Faifer F. R., Forte J. C., Norris M. A., Bridges T., Forbes D. A., Zepf S. E., Beasley M., Gebhardt K., Hanes D. A., Sharples R. M., 2011, *MNRAS*, 416, 155
- Feigelson E. D., Babu G. J., 1992, *ApJ*, 397, 55
- Filippenko A. V., Chornock R., 2000, *IAU Circ.*, 7511, 2
- Forbes D. A., Beasley M. A., Brodie J. P., Kissler-Patig M., 2001, *ApJ*, 563, L143
- Forbes D. A., Brodie J. P., Grillmair C. J., 1997, *AJ*, 113, 1652
- Forbes D. A., Brodie J. P., Huchra J., 1996, *AJ*, 112, 2448
- Forbes D. A., Brodie J. P., Huchra J., 1997, *AJ*, 113, 887
- Forbes D. A., Franx M., Illingworth G. D., Carollo C. M., 1996, *ApJ*, 467, 126
- Forbes D. A., Ponman T., O’Sullivan E., 2012, *ArXiv e-prints*
- Forbes D. A., Proctor R., Strader J., Brodie J. P., 2007, *ApJ*, 659, 188
- Forbes D. A., Sánchez-Blázquez P., Phan A. T. T., Brodie J. P., Strader J., Spitler L., 2006, *MNRAS*, 366, 1230
- Forbes D. A., Spitler L. R., Strader J., Romanowsky A. J., Brodie J. P., Foster C., 2011, *MNRAS*, 413, 2943
- Forestell A. D., Gebhardt K., 2010, *ApJ*, 716, 370
- Foster C., Proctor R. N., Forbes D. A., Spolaor M., Hopkins P. F., Brodie J. P., 2009, *MNRAS*, 400, 2135
- Foster C., Spitler L. R., Romanowsky A. J., Forbes D. A., Pota V., Bekki K., Strader J., Proctor R. N., Arnold J. A., Brodie J. P., 2011, *MNRAS*, 415, 3393
- Fried J. W., Illingworth G. D., 1994, *AJ*, 107, 992
- Gallagher J. S., Knapp G. R., Faber S. M., Balick B., 1977, *ApJ*, 215, 463
- Gebhardt K., Kissler-Patig M., 1999, *AJ*, 118, 1526
- Geisler D., Lee M. G., Kim E., 1996, *AJ*, 111, 1529
- Gerhard O., Jeske G., Saglia R. P., Bender R., 1998, *MNRAS*, 295, 197
- Graham A. W., Driver S. P., Petrosian V., Conselice C. J., Ber-shady M. A., Crawford S. M., Goto T., 2005, *AJ*, 130, 1535

- Hargis J. R., Rhode K. L., Strader J., Brodie J. P., 2011, *ApJ*, 738, 113
- Harris W. E., Harris G. L. H., Layden A. C., Wehner E. M. H., 2007, *ApJ*, 666, 903
- Hetznecker H., Burkert A., 2006, *MNRAS*, 370, 1905
- Ho L. C., Feigelson E. D., Townsley L. K., Sambruna R. M., Garmire G. P., Brandt W. N., Filippenko A. V., Griffiths R. E., Ptak A. F., Sargent W. L. W., 2001, *ApJ*, 549, L51
- Hoffman L., Cox T. J., Dutta S., Hernquist L., 2010, *ApJ*, 723, 818
- Hopkins P. F., Bundy K., Croton D., Hernquist L., Keres D., Khochfar S., Stewart K., Wetzel A., Younger J. D., 2010, *ApJ*, 715, 202
- Hopkins P. F., Cox T. J., Dutta S. N., Hernquist L., Kormendy J., Lauer T. R., 2009, *ApJS*, 181, 135
- Hwang H. S., Lee M. G., Park H. S., Kim S. C., Park J.-H., Sohn Y.-J., Lee S.-G., Rey S.-C., Lee Y.-W., Kim H.-I., 2008, *ApJ*, 674, 869
- Jarrett T. H., Chester T., Cutri R., Schneider S. E., Huchra J. P., 2003, *AJ*, 125, 525
- Joanes D., Gill C. A., 1998, *The Statistician*, 47, 183
- Jordán A., Côté P., Blakeslee J. P., Ferrarese L., McLaughlin D. E., Mei S., Peng E. W., Tonry J. L., Merritt D., Milosavljević M., Sarazin C. L., Sivakoff G. R., West M. J., 2005, *ApJ*, 634, 1002
- Jordán A., McLaughlin D. E., Côté P., Ferrarese L., Peng E. W., Mei S., Villegas D., Merritt D., Tonry J. L., West M. J., 2007, *ApJS*, 171, 101
- Kissler-Patig M., Brodie J. P., Schroder L. L., Forbes D. A., Grillmair C. J., Huchra J. P., 1998, *AJ*, 115, 105
- Kissler-Patig M., Richtler T., Storm J., della Valle M., 1997, *A&A*, 327, 503
- Kormendy J., Bender R., 2012, *ApJS*, 198, 2
- Krajnović D., Emsellem E., Cappellari M., Alatalo K., Blitz L., Bois M., Bournaud F., Bureau M., Davies R. L., Davis T. A., de Zeeuw P. T., 2011, *MNRAS*, 414, 2923
- Kravtsov A. V., Gnedin O. Y., 2005, *ApJ*, 623, 650
- Kronawitter A., Saglia R. P., Gerhard O., Bender R., 2000, *A&AS*, 144, 53
- Kundu A., Whitmore B. C., 2001, *AJ*, 122, 1251
- Larsen S. S., Brodie J. P., Beasley M. A., Forbes D. A., Kissler-Patig M., Kuntschner H., Puzia T. H., 2003, *ApJ*, 585, 767
- Larsen S. S., Brodie J. P., Huchra J. P., Forbes D. A., Grillmair C. J., 2001, *AJ*, 121, 2974
- Larsen S. S., Brodie J. P., Strader J., 2005, *A&A*, 443, 413
- Lee M. G., Park H. S., Hwang H. S., Arimoto N., Tamura N., Onodera M., 2010, *ApJ*, 709, 1083
- Lee M. G., Park H. S., Kim E., Hwang H. S., Kim S. C., Geisler D., 2008, *ApJ*, 682, 135
- Masters K. L., Jordán A., Côté P., Ferrarese L., Blakeslee J. P., Infante L., Peng E. W., Mei S., West M. J., 2010, *ApJ*, 715, 1419
- McDermid R. M., Emsellem E., Shapiro K. L., Bacon R., Bureau M., Cappellari M., Davies R. L., de Zeeuw T., Falcón-Barroso J., Krajnović D., Kuntschner H., Peletier R. F., Sarzi M., 2006, *MNRAS*, 373, 906
- McMillan P. J., Athanassoula E., Dehnen W., 2007, *MNRAS*, 376, 1261
- Mei S., Blakeslee J. P., Côté P., Tonry J. L., West M. J., Ferrarese L., Jordán A., Peng E. W., Anthony A., Merritt D., 2007, *ApJ*, 655, 144
- Merrett H. R., Kuijken K., Merrifield M. R., Romanowsky A. J., Douglas N. G., Napolitano N. R., Arnaboldi M., Capaccioli M., Freeman K. C., Gerhard O., Evans N. W., Wilkinson M. I., Haliday C., Bridges T. J., Carter D., 2003, *MNRAS*, 346, L62
- Mieske S., Jordán A., Côté P., Kissler-Patig M., Peng E. W., Ferrarese L., Blakeslee J. P., Mei S., Merritt D., Tonry J. L., West M. J., 2006, *ApJ*, 653, 193
- Misgeld I., Mieske S., Hilker M., Richtler T., Georgiev I. Y., Schuberth Y., 2011, *A&A*, 531, A4
- Miyazaki S., Komiyama Y., Sekiguchi M., Okamura S., Doi M., Furusawa H., Hamabe M., Imi K., Kimura M., Nakata F., Okada N., Ouchi M., Shimasaku K., Yagi M., Yasuda N., 2002, *PASJ*, 54, 833
- Moore B., Diemand J., Madau P., Zemp M., Stadel J., 2006, *MNRAS*, 368, 563
- Muratov A. L., Gnedin O. Y., 2010, *ApJ*, 718, 1266
- Nagar N. M., Falcke H., Wilson A. S., 2005, *A&A*, 435, 521
- Napolitano N. R., Romanowsky A. J., Capaccioli M., Douglas N. G., Arnaboldi M., Coccato L., Gerhard O., Kuijken K., Merrifield M. R., Bamford S. P., Cortesi A., Das P., Freeman K. C., 2011, *MNRAS*, 411, 2035
- Napolitano N. R., Romanowsky A. J., Coccato L., Capaccioli M., Douglas N. G., Noordermeer E., Gerhard O., Arnaboldi M., de Lorenzi F., Kuijken K., Merrifield M. R., O'Sullivan E., Cortesi A., Das P., Freeman K. C., 2009, *MNRAS*, 393, 329
- Newman J. A., Cooper M. C., Davis M., Faber S. M., Coil A. L., Guhathakurta P., Koo D. C., Phillips A. C., Conroy C., Dutton A. A., Finkbeiner D. P., Gerke B. F., Rosario D. J., Weiner 2012, *ArXiv e-prints*
- Norris M. A., Gebhardt K., Sharples R. M., Faifer F. R., Bridges T., Forbes D. A., Forte J. C., Zepf S. E., Beasley M. A., Hanes D. A., Proctor R., Kannappan S. J., 2012, *MNRAS*, p. 2399
- Norris M. A., Sharples R. M., Bridges T., Gebhardt K., Forbes D. A., Proctor R., Faifer F. R., Forte J. C., Beasley M. A., Zepf S. E., Hanes D. A., 2008, *MNRAS*, 385, 40
- Olsen K. A. G., Miller B. W., Suntzeff N. B., Schommer R. A., Bright J., 2004, *AJ*, 127, 2674
- Oser L., Ostriker J. P., Naab T., Johansson P. H., Burkert A., 2010, *ApJ*, 725, 2312
- Ostrov P., Geisler D., Forte J. C., 1993, *AJ*, 105, 1762
- O'Sullivan E., Forbes D. A., Ponman T. J., 2001, *MNRAS*, 328, 461
- Ouchi M., Shimasaku K., Okamura S., Furusawa H., Kashikawa N., Ota K., Doi M., Hamabe M., Kimura M., Komiyama Y., Miyazaki M., Miyazaki S., Nakata F., Sekiguchi M., Yagi M., Yasuda N., 2004, *ApJ*, 611, 660
- Pellegrini S., Siemiginowska A., Fabbiano G., Elvis M., Greenhill L., Soria R., Baldi A., Kim D. W., 2007, *ApJ*, 667, 749
- Peng E. W., Jordán A., Côté P., Blakeslee J. P., Ferrarese L., Mei S., West M. J., Merritt D., Milosavljević M., Tonry J. L., 2006, *ApJ*, 639, 95
- Pierce M., Beasley M. A., Forbes D. A., Bridges T., Gebhardt K., Faifer F. R., Forte J. C., Zepf S. E., Sharples R., Hanes D. A., Proctor R., 2006, *MNRAS*, 366, 1253
- Pinkney J., Gebhardt K., Bender R., Bower G., Dressler A., Faber S. M., Filippenko A. V., Green R., Ho L. C., Kormendy J., Lauer T. R., Magorrian J., Richstone D., Tremaine S., 2003, *ApJ*, 596, 903
- Prieto J. L., Gnedin O. Y., 2008, *ApJ*, 689, 919
- Proctor R. N., Forbes D. A., Forestell A., Gebhardt K., 2005, *MNRAS*, 362, 857
- Proctor R. N., Forbes D. A., Romanowsky A. J., Brodie J. P., Strader J., Spolaor M., Mendel J. T., Spitler L., 2009, *MNRAS*, 398, 91
- Prugniel P., Simien F., 1996, *A&A*, 309, 749



- Puzia T. H., Kissler-Patig M., Thomas D., Maraston C., Saglia R. P., Bender R., Richtler T., Goudfrooij P., Hempel M., 2004, *A&A*, 415, 123
- Rhode K. L., Zepf S. E., 2001, *AJ*, 121, 210
- Rhode K. L., Zepf S. E., 2004, *AJ*, 127, 302
- Romanowsky A. J., Douglas N. G., Arnaboldi M., Kuijken K., Merrifield M. R., Napolitano N. R., Capaccioli M., Freeman K. C., 2003, *Science*, 301, 1696
- Romanowsky A. J., Strader J., Brodie J. P., Mihos J. C., Spitler L. R., Forbes D. A., Foster C., Arnold J. A., 2011, *ArXiv e-prints*
- Romanowsky A. J., Strader J., Spitler L. R., Johnson R., Brodie J. P., Forbes D. A., Ponman T., 2009, *AJ*, 137, 4956
- Sandage A., Bedke J., 1994, *The Carnegie Atlas of Galaxies. Volumes I, II*.
- Schlegel D. J., Finkbeiner D. P., Davis M., 1998, *ApJ*, 500, 525
- Schroder L. L., Brodie J. P., Kissler-Patig M., Huchra J. P., Phillips A. C., 2002, *AJ*, 123, 2473
- Schuberth Y., Richtler T., Hilker M., Dirsch B., Bassino L. P., Romanowsky A. J., Infante L., 2010, *A&A*, 513, A52
- Sérsic J. L., 1963, *Boletín de la Asociación Argentina de Astronomía La Plata Argentina*, 6, 41
- Shapiro K. L., Genzel R., Förster Schreiber N. M., 2010, *MNRAS*, 403, L36
- Sil'chenko O. K., Afanasiev V. L., Chavushyan V. H., Valdes J. R., 2002, *ApJ*, 577, 668
- Simien F., Prugniel P., 2000, *A&AS*, 145, 263
- Sinnott B., Hou A., Anderson R., Harris W. E., Woodley K. A., 2010, *AJ*, 140, 2101
- Skrutskie M. F., Cutri R. M., Stiening R., Weinberg M. D., Schneider S., Carpenter J. M., Beichman C., Capps R., Chester T., Elias 2006, *AJ*, 131, 1163
- Spitler L. R., Forbes D. A., Strader J., Brodie J. P., Gallagher J. S., 2008, *MNRAS*, 385, 361
- Spitler L. R., Larsen S. S., Strader J., Brodie J. P., Forbes D. A., Beasley M. A., 2006, *AJ*, 132, 1593
- Spitler L. R., Romanowsky A. J., Diemand J., Strader J., Forbes D. A., Moore B., Brodie J. P., 2012, *MNRAS*, p. 2978
- Spolaor M., Forbes D. A., Hau G. K. T., Proctor R. N., Brough S., 2008, *MNRAS*, 385, 667
- Spolaor M., Forbes D. A., Proctor R. N., Hau G. K. T., Brough S., 2008, *MNRAS*, 385, 675
- Strader J., Brodie J. P., Cenarro A. J., Beasley M. A., Forbes D. A., 2005, *AJ*, 130, 1315
- Strader J., Brodie J. P., Spitler L., Beasley M. A., 2006, *AJ*, 132, 2333
- Strader J., Romanowsky A. J., Brodie J. P., Spitler L. R., Beasley M. A., Arnold J. A., Tamura N., Sharples R. M., Arimoto N., 2011, *ApJS*, 197, 33
- Tamura N., Sharples R. M., Arimoto N., Onodera M., Ohta K., Yamada Y., 2006, *MNRAS*, 373, 601
- Teodorescu A. M., Méndez R. H., Bernardi F., Riffeser A., Kudritzki R. P., 2010, *ApJ*, 721, 369
- Tomita A., Aoki K., Watanabe M., Takata T., Ichikawa S.-i., 2000, *AJ*, 120, 123
- Tonry J., Davis M., 1979, *AJ*, 84, 1511
- Tonry J. L., Dressler A., Blakeslee J. P., Ajhar E. A., Fletcher A. B., Luppino G. A., Metzger M. R., Moore C. B., 2001, *ApJ*, 546, 681
- van der Marel R. P., Franx M., 1993, *ApJ*, 407, 525
- Vesperini E., Zepf S. E., Kundu A., Ashman K. M., 2003, *ApJ*, 593, 760
- Vitvitska M., Klypin A. A., Kravtsov A. V., Wechsler R. H., Prugniel P., Bullock J. S., 2002, *ApJ*, 581, 799
- Walker M. G., Peñarrubia J., 2011, *ApJ*, 742, 20
- Weijmans A.-M., Cappellari M., Bacon R., de Zeeuw P. T., Em-sellem E., Falcón-Barroso J., Kuntschner H., McDermid R. M., van den Bosch R. C. E., van de Ven G., 2009, *MNRAS*, 398, 561
- Weil M. L., Pudritz R. E., 2001, *ApJ*, 556, 164
- Whitmore B. C., Sparks W. B., Lucas R. A., Macchetto F. D., Biretta J. A., 1995, *ApJ*, 454, L73
- Williams M. J., Bureau M., Cappellari M., 2010, *MNRAS*, 409, 1330
- Wisnioski E., Glazebrook K., Blake C., Wyder T., Martin C., Poole G. B., Sharp R., Couch W., Kacprzak G. G., Brough S., Colless M., Contreras C., 2011, *MNRAS*, 417, 2601
- Woodley K. A., Gómez M., Harris W. E., Geisler D., Harris G. L. H., 2010, *AJ*, 139, 1871
- Yoon S.-J., Lee S.-Y., Blakeslee J. P., Peng E. W., Sohn S. T., Cho J., Kim H.-S., Chung C., 2011, *ApJ*, 743, 150
- Yoon S.-J., Sohn S. T., Lee S.-Y., Kim H.-S., Cho J., Chung C., Blakeslee J. P., 2011, *ApJ*, 743, 149
- Yoon S.-J., Yi S. K., Lee Y.-W., 2006, *Science*, 311, 1129
- Younes G., Porquet D., Sabra B., Grosso N., Reeves J. N., Allen M. G., 2010, *A&A*, 517, A33
- Zepf S. E., Ashman K. M., 1993, *MNRAS*, 264, 611
- Zhang Z., Xu H., Wang Y., An T., Xu Y., Wu X.-P., 2007, *ApJ*, 656, 805

#### APPENDIX A: VELOCITY BIAS CORRECTION

A feature of the kinematic modelling used in this work (equation 4) is that the rotation amplitude is biased to higher values when the kinematic position angle is unconstrained. This effect becomes important in systems with  $V_{\text{rot}} \ll \sigma$ , because the rotation (and its direction) is fully embedded in the dispersion. There are two ways to approach this issue: numerically, via a Monte Carlo simulation, or analytically, using the Box's bias measure in non-linear model theory (Box 1971). The first method is the most straightforward, whereas the latter is computationally more complicated. Here we adopt a similar approach to Strader et al. (2011) and correct for the bias via a Monte Carlo simulation.

In practice, for each data bin containing  $N$  GCs (see Figure 11), we compute the best fit rotation by minimizing equation 3. We then generate 1000 artificial datasets, of the same size  $N$ , drawn from the best-fit model. We repeat the fit for each generated dataset using the original best-fit model as starting point. We define the velocity bias as the median difference between the computed and the simulated (known) rotation amplitude. This approach is adopted to correct for the bias also in Figure 12, Table 6 and Table 7.

We find that the magnitude of the bias correction depends both on the bin size and on the  $(V_{\text{rot}}/\sigma)$ . In the case of  $(V_{\text{rot}}/\sigma) \gtrsim 1$ , the bias is negligible regardless the bin size. For bins with  $(V_{\text{rot}}/\sigma) \sim 0.4$  (0.6) and  $N \leq 20$ , the bias can be up to  $\sim 50$  (40)  $\text{km s}^{-1}$ . Within the same  $(V_{\text{rot}}/\sigma)$  values, the bias can decrease down to  $\sim 30$  (20)  $\text{km s}^{-1}$  for  $N \approx 50$ . This agrees with the rule of the thumb of Strader et al. (2011) to identify the severity of the bias, i.e. the bias is small if  $(V_{\text{rot}}/\sigma) \geq 0.55 \times \sqrt{20/N}$ . If this condition is satisfied, we find that the bias is of the order of (or less than) our nominal median uncertainty of 15  $\text{km s}^{-1}$ .